Outflow and clogging of rigid and soft particles in silos with small apertures

Dissertation

to obtain the academic degree

doctor rerum naturalium
(Dr. rer. nat.)

approved by the Faculty of Natural Sciences
of Otto von Guericke University Magdeburg

by

M.Sc. Phys. Ahmed Mohamed Ali Ashour Ahmed

born on 14th April 1985 in Cairo

Reviewer 1: Prof. Dr. rer. nat. habil. Ralf Stannarius

Reviewer 2: Prof. Dr. rer. nat. habil. Ingo Rehberg

submitted on 22nd November 2017

defended on 19th February 2018

Contents

1 Introduction and literature work

1.1 Motivation to study granular materials

Granular materials are a highly interesting research area, not only because they have unusual physical properties [1–3] but also because they are present everywhere in our daily life, on a macroscopic scale. Most grains which we come across every day in our kitchens are granular matter. If you want to prepare a cup of coffee, you have to deal with at least one form of granulates. This type of material also plays an important role in some natural phenomena (e.g. earthquakes and mudslides), and there are numerous applications for using granulates in industry, like coal and grain handling, chemical processing, agriculture, mining, pharmaceuticals and many other industrial branches.

Granular materials are present in three different phases; solid, liquid and gas as in Fig. 1.1 [4]. While they have simple forms in nature, their physical properties are still not completely understood. This is because many parameters play a role during their interactions with each other and the surrounding, for example, surface texture, the shape of the particles, the degree of softness, the packing fraction and many other grain features on the microscopic level, which determine the macroscopic ensemble properties to a great extent.

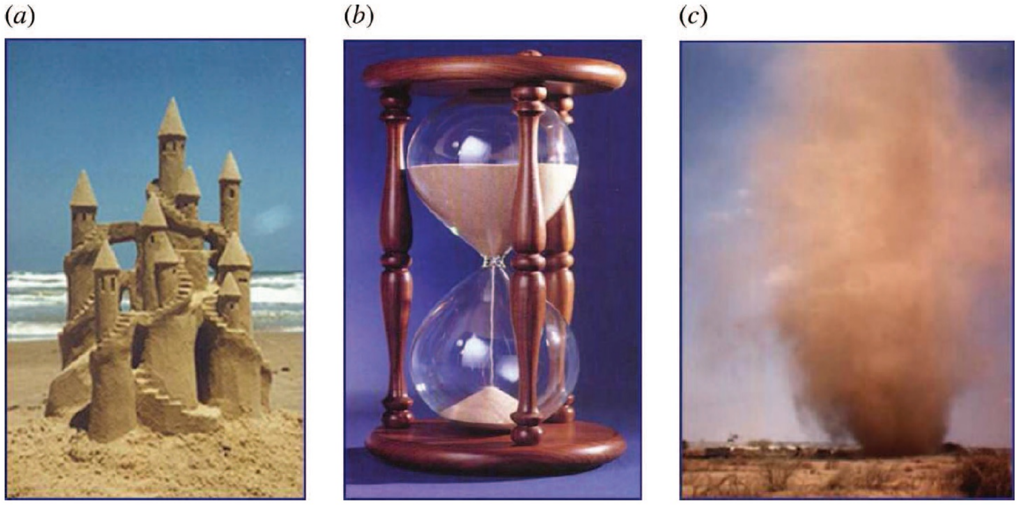

Figure 1.1: Different states for sand as a granular material: (a) solid sand castle on beach, (b) outflow of sand from an hourglass like a liquid, and (c) dust devil like a gas in desert. Figure taken from Ref. [4].

1.2 Introduction to silo discharge

The study of the outflow of granular materials from a silo has an extensive history, and still remains an important research area [5]. In our daily life and also in many industrial fields, one can come across the discharge of granulates of different shapes and geometries from a container with a small orifice.

During the past decades, much work has been done to understand the static and dynamic properties during the discharge of hard particles from 2D or quasi-2D silos [6–47] and 3D silos [48–87], and a few experiments have dealt with soft particles in 2D silos [88–91]. Although there is a good deal of literature on this topic, some aspects remain a mystery, and there are several new phenomena which do not yet have a clear explanation.

There are some basic common forces which govern the silo discharge, that is, the friction force between the grains, the friction between the grains and the container's walls, and its associated electrostatic force (which is in general very small and can be controlled by choosing appropriate particles and containers [92]). In most of the previous experiments in the literature, the discharge of grains was studied under gravity as an external force. When the orifice size is not much larger than the size of the particles, we can find fluctuations during the discharging, or clogging. At a certain moment, self sustaining particles can block the outlet and arrest the outflow [18]. The intermittency in the flow and its arrest are similar to what we can see in colloidal systems [93], the motion of microparticles [94–96] or microbes [97] in suspensions through microchannels, or a flock of sheep [98] or crowd of people [99,100] evacuating a place through a narrow exit and daily in a traffic jam [101]. In spite of the significant difference between the previous systems they show a strong similarity in the clogging process [102].

For hard disks in 2D silos, it was observed that clogging occurs until the orifice size is nearly equal to or greater than 5 grain diameters [10] and this number changes with different types of grains [58]. In a simple 2D silo, we define the first layer of grains above the orifice which blocks it and arrests the flow as an *arch* [10], and in the case of a 3D silo, we define the first shell of the grains which blocks the outlet as a *dome* [86]. The constructed 2D arch or 3D dome is stable enough and can hold all the materials above it [103]. The stability of such arches and its forces were investigated in Ref. [30, 34, 42, 104] in 2D and quasi-2D silos.

There are some parameters which play an important role in changing the shape and the size of the arch or dome, for example, the size of the particles, the shape parameters, the softness and the orifice size [58, 87]. These parameters also affect the clogging probability by influencing the avalanche size (the number of grains which falling down between two successive clogs).

Most silo experimental work carried out so far was focused on monodisperse disks in 2D silos [10] or spherical grains in 3D silos [58], because they do not need a special imaging technique (*e.g.* computer tomography) to see what is happening inside the silo, and the behavior of such material is easier to comprehend than that of anisotropic grains. So only few experiments have been performed using anisotropic particles [58, 87].

1.3 Clogging probability, avalanche size and critical orifice size

The clogging or jamming probability as it is called sometimes in the literature, mainly depends on the particles and orifices sizes [14, 16, 58, 81]. To *et al.* [10] were pioneers who described this probability. They introduced a 2D experimental hopper filled with monodisperse stainless steel disks. In this fixed size hopper the jamming probability was dependent on the relative orifice size d (the ratio between the orifice width and the disk diameter). The jamming probability was close to 1 when the orifice size was slightly larger than the disk diameters and decreased with the orifice size until it reached zero when $d \approx 5$. The roughness also played a role in changing the probability values. Therefore they tested rough disks with 25 v-shaped and found that the jamming probability then increased at a given d (see Fig. 1.2). Moreover, the number of disks which formed the arch and closed the outlet were affected by the roughness. The arch took a convex shape almost everywhere and the arch length was greater than the orifice size with smooth disks. In their recent work [11] they found the jamming probability $J(d)$ dependent on the amount of the particles inside the silo. For 200 disks $J(d) = 0.5$ at $d \approx 4$, and for 700 disks $J(d) = 0.5$ at $d \approx 4.8$.

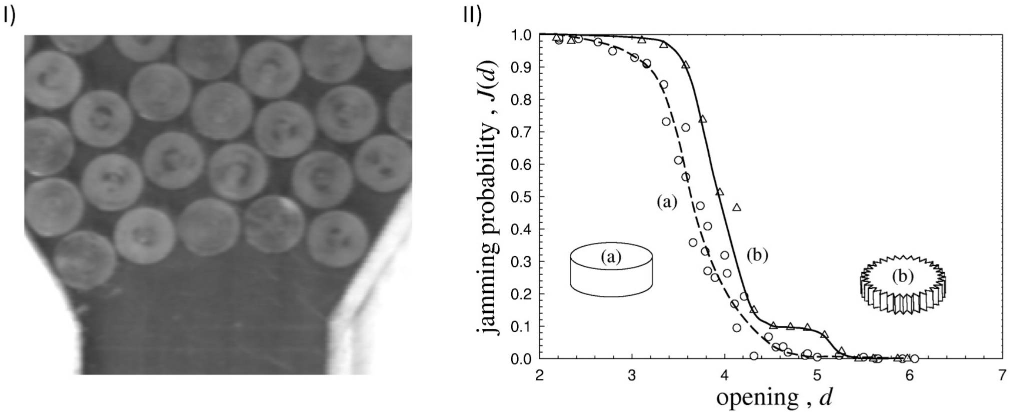

Figure 1.2: (I) Typical jamming shape for the experimental work. (II) The jamming probability $J(d)$ versus the relative orifice size d for, a) smooth disks and b) rough disks when the silo angle = 60^o. Figures taken from Ref. [10].

A comparable result had been shown by Janda *et al.* [16]. They filled their 2D silo with spherical beads and ran the experiment using different numbers of grains. They defined the jamming probability in their case as the probability at which the discharge gets arrested before X grains fall (the probability of each bead passing through the outlet and arresting the outflow is close to one for much smaller orifices and zero for large orifices). They found also that the jamming probability was not only dependent on the orifice size, but also on the number of grains inside the silo. The probability increases with X at the same given orifice size. A similar behavior was also demonstrated in the case of 3D cylindrical silo loaded with spherical beads [57].

Another important factor in studying the silo discharge through a small aperture is the avalanche size (the number of grains falling down between two successive clogs), which has an inverse relation with the clogging probability (when the system clogs more the avalanche size becomes small). The distribution of the avalanche size has been tested on different orifice sizes and shown an exponential decay [57], which means that the clogging probability is the same for all the grains [37,39]. Zuriguel *et al.* [58] studied the avalanche size distribution in a 3D silo using spherical grains and one type of elongated rice grains. They introduced an empirical power law (Eqn. 1.1) which enabled them to fit their experimental data in Fig. 1.3 with a sufficient accuracy. This law described the change in the mean avalanche size $\langle S \rangle$ in relation to the orifice size.

$$\langle S \rangle = A\left(R_c - \frac{R}{r_{eq}}\right)^{-\beta} \tag{1.1}$$

where R, is the orifice radius; r_{eq}, is the radius of the spherical grains or the radius of the sphere with the same volume in the case of the elongated grains; A and β, are fitting parameters, the value of β was ≈ 7 and does not depend on the type of tested grains. The most important parameter in this equation is the critical orifice size R_c in units of the bead diameter, which indicated the critical orifice size after which no jamming occurs for the grains, and where they can be discharged from the silo without interruption. The values of R_c changed with grain shapes. It was illustrated in his work as being ≈ 5 for spherical grains and ≈ 6 for rice grains.

In contrast to the previous model, Thomas and Durian [75, 81] conducted experimental work with three different silos and three different spherical grains. They succeeded on fitting the mean avalanche size $\langle S \rangle$ data at different tilted hopper angles by the following exponential equation

$$\langle S \rangle = c \,\mathrm{x} \exp\left\{ a \left(\frac{R}{r_{eq}}\right)^{3} \right\}, \tag{1.2}$$

where c and a, are the fitting parameters; R, is the orifice radius; and r_{eq}, is the radius of the spheres. By this equation, we can say that the clogging probability is the same for each grain during the avalanche. The most important difference between Thomas' and Zuriguel's models is the critical orifice size which discriminates the clogging regime and the free discharge regime. In the Thomas model we can expect that the flow can clog at any orifice size, although the clogging probability is very low and tends to zero for the very large orifice sizes.

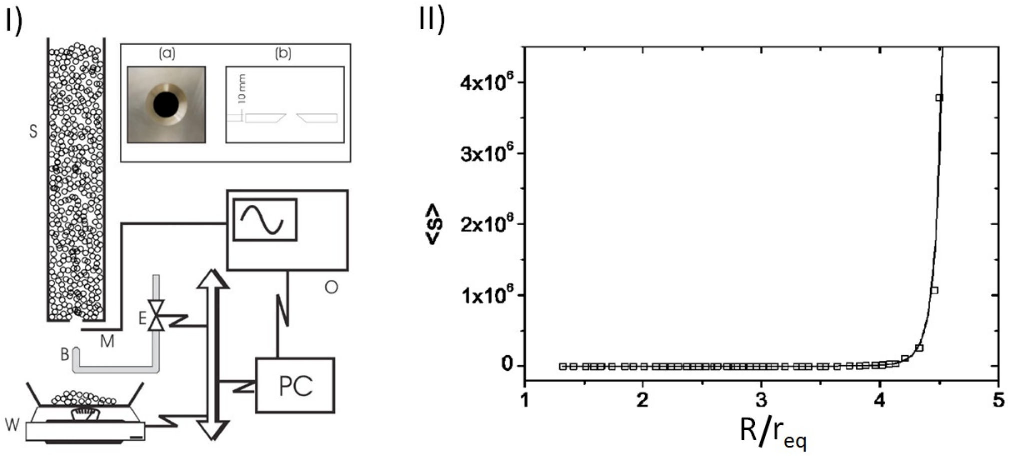

Figure 1.3: (I) Sketch of the experimental setup. (II) Mean avalanche size versus the rescaled orifice size (R/r_{eq}). The solid line represents the fit with Eqn. 1.1. Figures taken from Ref. [58].

1.4 Mass discharge and Beverloo's equation

The mass discharge of granular materials from a silo is in contrast to the behavior of fluids, and does in general not depend on the filling height [105]. After a certain filling height (around 1.5 of the diameter of the silo), a saturation in the pressure is found at the bottom of the silo according to the Janssen effect [106]. This leads to a constant flow rate during the discharge. But even if the pressure at the container bottom lowers at lower fill heights, the discharge rate is only a little influenced. The diameter of the container as well should be more than 30 beads in diameter to avoid any wall effect [50].

The most accepted equation until now for describing the mass discharge of different types of grains through different silo shapes, was established by Beverloo *et al.* [49] in 1961 in the following form

$$W = \mathit{\Gamma} \rho_b \sqrt{g} (D - kd)^{n+1/2}. \tag{1.3}$$

Where W is the mass flow rate of the grains from a silo, mainly dependent on the orifice diameter ($D = 2R$) and the grain diameters ($d = 2r_{eq}$). The other symbols in this equation are constants or fitting parameters. $\mathit{\Gamma}$ and k, dimensionless constants, come from the fitting and mainly depend on the silo and grain shapes; ρ_b, is the particles' effective density; g, is free fall gravitational acceleration and $n = 2$ in the case of 3D silos. Beverloo executed this work when the orifice diameter was big enough to avoid any type of intermittency in the flow during the discharge and the diameter of the grains was greater than 0.5 mm. For the spherical grains, the fitting parameter $\mathit{\Gamma}$ was between 0.55 and 0.65 which indicated the packing fraction, and the parameter $k \approx 1.4$.

In the subsequent decades, Beverloo's equation has succeeded in describing the flow rate through different silos of different shapes, angles and diameters [32], especially at large orifice sizes, where the amount of the discharged materials increases with the orifice size [52]. Moreover, in recent years, some modifications have been made to Beverloo's law by Mankoc *et al.* [105], to enable them to fit their data in two regimes. The first regime when the orifice size is very small (just a few beads in diameter) which allowed recording avalanches, the second one when the orifice is large enough and there was no clogging during the discharge. They demonstrated the validity of their equation

$$W_b = C^{'}\ (1 - \frac{1}{2}\ e^{-b\ (R-1)})(R-1)^{\alpha}, \tag{1.4}$$

by applying it to their experimental and numerical results in 3D and 2D silos (see Fig. 1.4). Where W_b is the number of the discharged beads; $C^{'}$ (which contains the parameters $\mathit{\Gamma}$, ρ_b and g in Eqn. 1.3) and b, are fitting parameters; R, is the ratio between the orifice radius and the grain radius; α is constant, $\alpha = 5/2$ in the case of 3D silos and $3/2$ in case of 2D silos.

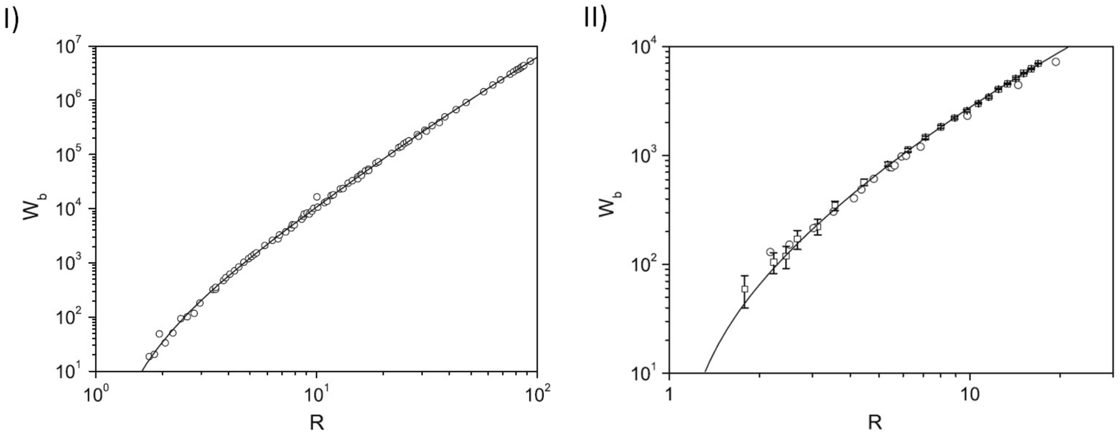

Figure 1.4: (I) 3D silo experimental data for glass beads fitted by Eqn. 1.4 with $C^{'} = 64.6$, b = 0.051 and $\alpha = 5/2$. (II) 2D silo experimental data (circles) and numerical simulations (squares) fitted by Eqn. 1.4 with $C^{'} = 108$, b = 0.23 and $\alpha = 3/2$. Figures taken from Ref. [105].

Recently Sheldon [66] and Thomas [75] have completed extensive experimental studies on silos by using three different spherical glass beads. They proved that Beverloo's law can fit the mass flow rate data with the same fitting parameters, both at small orifice sizes which have avalanches, as well as for large orifices which have a continuous discharge without interruption (see Fig. 1.5).

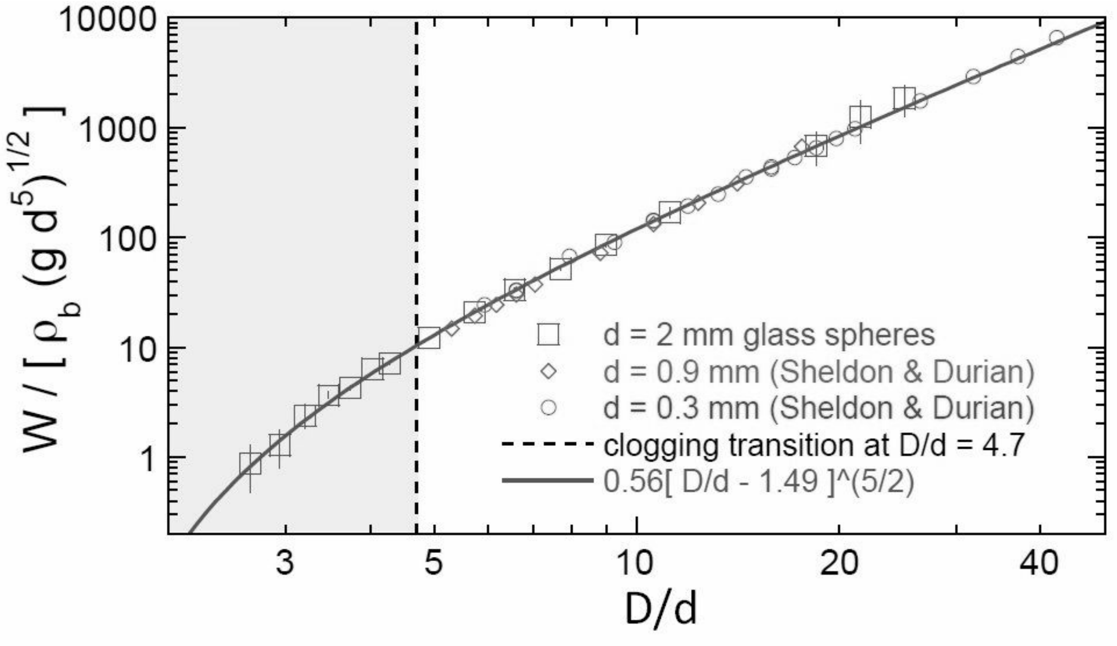

Figure 1.5: Dimensionless mass flow rate $W/(\rho_b\sqrt{gd^5})$ versus the dimensionless orifice diameter. The solid black curve is fitted by Eqn. 1.3 with $\Gamma = 0.56$ and $k = 1.5$. The vertical dotted line separates the clogging regime and the free flow regime. Figure taken from Ref. [75].

1.5 Janssen's effect with hard grains

When we loaded our silo with hard granular materials, the measured pressure at the bottom of the silo increased with the height until a certain filling height and after that went to saturation in accordance with Janssen's effect as in Fig. 1.6 [106,107]. The rest of the weight of the materials inside the silo after that critical filling height is transferred to the side walls by force chains. The transfer process mainly depends on friction between the grains, which plays an important role in carrying that weight. So the silos walls have to be strong enough to be able to carry the weight of the grains above.

Softness and low friction of grains may play a role in changing the Janssen effect to a behavior similar to what happens when we fill the silo with liquids (hydrostatic pressure characteristics). In the case of liquids the measured pressure at the bottom of the silo represents the weight of all of the liquid above it (the pressure increasing linearly with the filling height and no saturation).

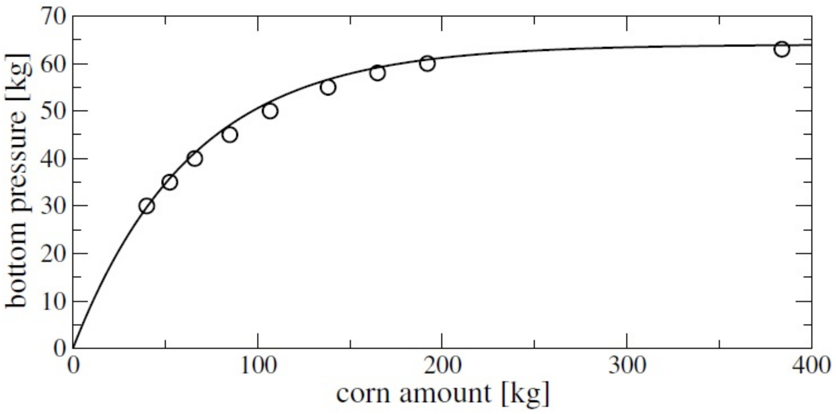

Figure 1.6: The measured pressure at the silo bottom versus the filling amount. Figure taken from Ref. [107].

1.6 Behavior of soft materials inside silos

Recently, a few experiments have been performed to check the behavior of soft particles inside a silo. Bertho *et al.* [88] studied the flow of dense quasi monodisperse air bubbles through an inverse 2D silo with a small aperture (see Fig. 1.7).

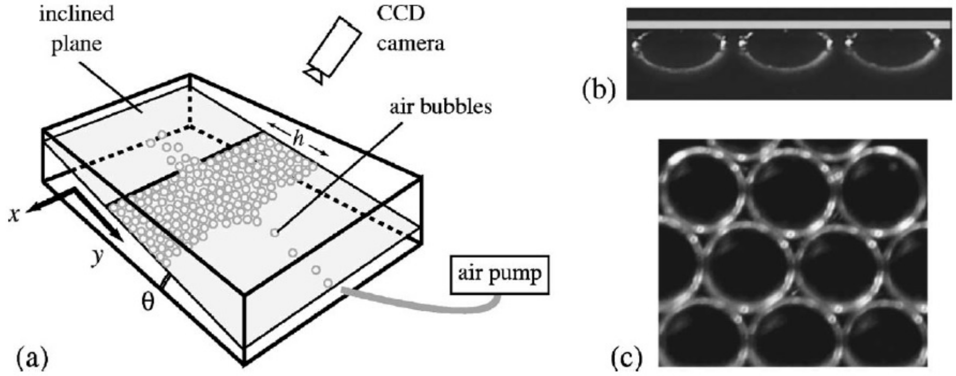

Figure 1.7: (a) Sketch of the inverse 2D experimental silo setup. The setup is immersed into water and filled with air bubbles. (b) Side view of the air bubbles. (c) Top view of the air bubbles. Figure taken from Ref. [88].

The silo was immersed in water and tilted at a small angle θ (between 0 and 1) to decrease the gravity influence. Dish-washing solution was added to prevent the bubbles from joining together. They found the outflow rate Q can be described by the equation (similar to Beverloo's law [49])

$$Q \propto g^{1/2}(W/d - k)^{1/2}, \tag{1.5}$$

where g is the gravitational acceleration; W is the orifice width; d is the bubble diameter; k is an empirical constant < 1, linked with the deformability of the bubbles and the friction between them. As a result of the high deformation in the air bubbles especially in the first layers nearest the orifice, the bubbles were able to move through the orifice even when $W < d$ and no clogging was noticed during this study.

Another group later studied the flow of polydisperse oil droplets in a water emulsion by using an inversed quasi-2D hopper [90, 91]. They approximated the droplets to frictionless disks by adding a surfactant to the water. Due to the nearly zero friction between the droplets, the droplets clogged at a small orifice size compared to the hard disks [10] (this clogging is resolved after some time as a result of the high deformability of the oil droplets). The clogging probability becomes zero when the orifice size is slightly larger than two droplets in diameter and the probability equals 0.5 when the orifice size ≈ 1.4 droplets in diameter. Because they could not distinguish between the influence of the softness and the friction, they introduced a numerical simulation to enable them to change the gravity (which related to the deformability or the softness). When the gravity decreased (low load) the arch became stronger and clogging was observed at larger orifice sizes than before. This was in contrast to the previous result for the hard grains [102].

1.7 The properties of 2D arches and 3D domes

During the discharge of granular materials from a silo with a small outlet we sometimes find a fluctuation in the outflow velocity followed by clogging as a result of an arch in the 2D silo (some grains block the outlet) which arrests the outflow. One of the most important properties of the arch is its stability, whether it is strong enough and able to carry the weight of the grains above it [30, 103]. Some numerical and simulation work has been done in the last years to describe the arches and their stability by performing a force analysis of the arches and studying the influence of friction on their construction [34, 61, 103, 108, 109]. A few experimental studies have been done to understand the complexities of the supposedly simple arches in 2D silos.

The arch structure (a stable set of disks closing the outlet and preventing the particles from reaching the outflow) was investigated experimentally by To *et al.* [10] using disks in a 2D hopper. In this study, they found that the arch is almost convex everywhere and all the particles which belong to the arch should be in contact. Moreover the width of the arch should be greater than the orifice width, and the number of disks in the arch have been found to increase with the orifice size [11].

Garcimartín *et al.* [18] introduced an experimental work to describe and analyze the arch formed by means of spherical beads in a 2D silo. Since their silo had a flat base, they suggested discarding some beads from the first layer above the orifice which blocked it and defining them by the base of that arch, not belonging to it, because they are mechanically stable by themselves (see Fig. 1.8). The arch aspect ratio has been defined as the ratio between the half of the arch span and the arch height. Some beads in the detected arches have been found hanging from above, which means the angle formed between such beads and its two neighbors was greater than 180^o, and these were called "defects". In that case, some parts in the arches take a concave shape instead of convex shape everywhere. More recently, another experimental work proved that the angles between the particles play an important role in making the arch stable against vibration. When the angles increased, the breaking of the arch became easier [110], and the probability of finding defects with an angle $> 180^o$ increased with the orifice size [42].

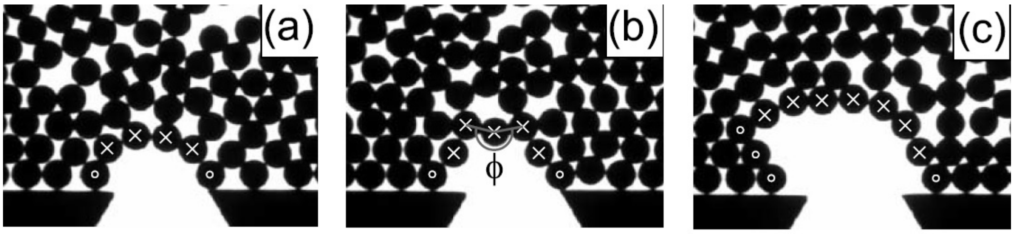

Figure 1.8: (a), (b) and (c) are three different 2D arch images. The beads which are marked with a white cross belong to the arch, and those with white circles indicate the base of the formed arch. In (b) we can see an example of a bead which has an angle greater than 180^o. Figure taken from Ref. [18].

In the 3D silo, the analysis of the dome (the first shell of particles above the orifice which arrests the discharge) needs special imaging techniques. Ashour *et al.* [87] studied the 3D dome formed by spherical particles and anisotropic particles with different aspect ratios. They used X-ray tomography and an optical inspection method for detecting all the particles in the dome and their orientations. The two methods showed similar results. For elongated grains, their long axis tends to align toward the orifice center, and the shell formed by the elongated grains is thicker compared to those of spheres with the same volume. In the case of the elongated grains more grains are needed to block the outlet and the number of grains in the blocked shell increases with the aspect ratio.

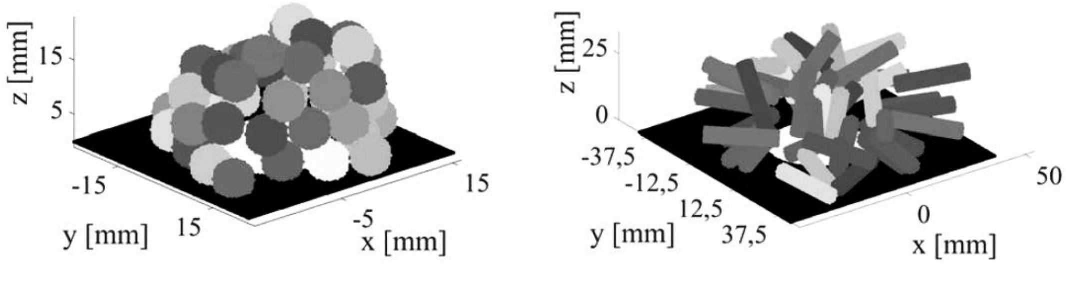

Figure 1.9: The first detected shell of the particles above the orifice by using X-ray tomography. left, peas (nearly spherical); right, cylindrical wooden pegs with aspect ratio 5. Figure taken from Ref. [87].

1.8 Parameters affecting the clogging and flow in silos

Many parameters affect the clogging probability and the flow of particles from silos.

Zuriguel *et al.* [19] proved that the presence of an obstacle inside the silo can reduce the chance of the particles clogging the outlet, if it is placed in an appropriate position (See Fig. 1.10). In this experiment, they used spherical beads of 1 mm in diameter and an orifice width of 4.2 mm. They attributed the reason for the reduction in the clogging to the decrease in pressure in the vicinity above the orifice. This work was extended in Ref. [27] where the authors changed the orifice sizes to investigate the influence of the obstacle position on the avalanche size and the flow rate. They showed that there is not necessarily a relation between the mean avalanche size and the average flow rate. The mean avalanche size increases with the obstacle height h (the vertical distance from the middle of the orifice to the lowest point of the obstacle) and reaches the maximum value at the appropriate position for the obstacle ($h \approx 4$). The average flow rate followed another trend where it decreased of the normal value (without obstacle) at small h and for large h increased with a small shift up to 10%.

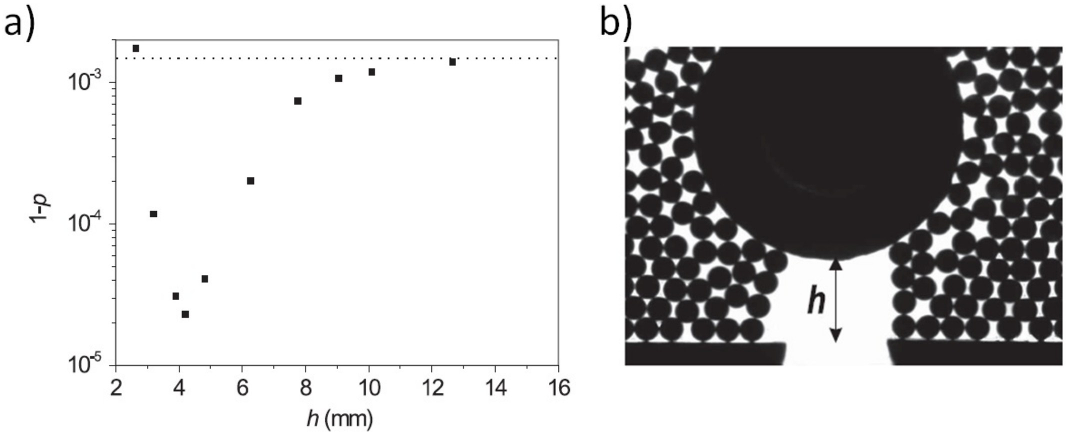

Figure 1.10: (a) The Probability of a particle clogging the orifice versus the obstacle height, the dashed line indicates the probability in the absence of the obstacle. (b) Photograph of the 2D experimental silo setup with a circular obstacle. Figure taken from Ref. [19].

A recent work [47] studied the influence of the obstacle shape experimentally and numerically by introducing circular, horizontal bar, upward triangular and downward triangular obstacles. The authors found experimentally that the triangular obstacle has the ability to reduce and prevent clogging when it is placed at a certain height h above the orifice, and numerically the horizontal bar could do the same. The reason was the low packing fraction in the area above the orifice, which is sufficient to prevent clogging.

Another parameter affecting the behavior of granular materials in silos is gravity. The effect of high and low gravity from the earth gravity on the silo discharge was studied by using different silo shapes loaded with different types of spherical beads [111]. These experiments confirmed the dependence of the flow rate on the square root of the gravity, which was introduced by Beverloo. Moreover, there was not a significant change in the critical orifice size (the size of the orifice after which no jamming) with gravity. A numerical simulation was done later on spherical particles in a rectangular 2D silo [112]. In this study, by increasing the gravity, the mean avalanche size showed a weak dependence on the gravity, while there was a significant decrease in the time taken by the avalanches which produced a high flow rate. The dependence of the flow rate on the orifice size under the influence of gravity was discussed, it increases with the orifice size at different values of driving forces. Furthermore, Beverloo's law fitted the flow rate data for the all selected values of gravity.

The influence of vertical and tilted orifices on the flow rate of the granulate from a silo has been studied in Ref. [52,52,66,113]. At the horizontal and vertical positions of the orifice, the flow rate increased with the orifice size according to Beverloo's equation. Furthermore, the tilt angle plays an important role in features of the discharge. A decrease in the flow rate was found to correspond with the cosine of the tilt angle and at large orifice sizes this decrease was linear.

The shape of the particles can make a dramatic change in the avalanche size distribution and the flow rate. Much numerical work has been performed to study the effect of anisotropic particles on the silo discharge by applying the Discrete Element Method (DEM), where it is easy to play with some parameters such as friction. Cleary and Sawley [8,114] showed that in the presence of friction the elongated particles change the shape of the flow pattern and can reduce the flow rate by around 30% compared to circular particles. On the other hand, in the absence of friction between the particles, Langston *et al*. [115] found the flow rate of the elongated particles with aspect ratio 5 was faster than for circular particles by 40% in 2D simulations, while in 3D simulations he did not notice a significant effect on the aspect ratio of the flow rate of rounded cylindrical particles and spheres. In addition Liu *et al*. [77] showed the decrease in the flow rate of ellipsoidal particles compared to spherical particles with nonzero friction in 3D silo.

Experimental work in Ref. [58] dealt with the effect of the particle shape on the avalanche size by using monodisperse, polydisperse and anisotropic rice grains. A critical orifice size after which the avalanche diverges has been found for all the grain types. Moreover the critical orifice size of the rice grains showed an increase in its value compared to the spherical grains.

Recently, Tang and Behringer [44] studied the discharge rate and the clogging probability of photoelastic elliptical particles in a quasi-2D hopper. They found that the orientation of the particles inside the hopper has a great effect on the flow rate and the blocking arch, where the elliptical particles were aligned toward the orifice in the shear flow zone and formed a stable arch. Another extensive study by Börzsönyi *et al.* [86] has been performed to investigate the flow field of elongated particles inside a 3D silo by using X-ray tomography. The particles in the flowing zone showed a high order of orientation and alignment toward the orifice. As a result of shear depletion, the packing density was smaller in the flowing zone compared to the stagnant zones on the sides of the orifice, and it decreases even more with increasing the aspect ratio.

At the end of this introduction, we may say that silo discharge and its clogging processes are still insufficiently understood particularly for non-spherical grains. So we have many open questions which await solutions as well as detailed flow properties. In this thesis we are going to introduce some of these questions and their answers.

2 Outflow and clogging of elongated particles in a 3D-silo

2.1 Experimental setup and materials

2.1.1 Silo setup

In this chapter we use a 3D uniform cylindrical plastic silo with 5 mm wall thickness, 600 mm height and inner diameter 150 mm, much larger than the grain sizes to avoid wall effects [55]. The silo has an aluminum flat base. At the center of this base, we insert exchangeable plates with circular holes, each hole having a diameter 1 mm larger than the previous one, with precision 0.1 mm.

The grains are poured into the silo through a transparent box ″like a hopper‶. When this box is empty we refill it again to make sure there are sufficient grains inside the silo during discharging, thus keeping a constant outflow (see Fig. 2.1). Grains are discharged from the silo outlet under gravity influence, there are no other external forces governing this process. The grains are collected in another box below the silo and above an electronic scale ($KERN_{KB}1000$) with resolution 0.05 g, which means it can detect one or two beads of the grains listed in Table 2.1.

At a certain moment, some grains assemble and construct a dome above the orifice, block it and arrest the flow. To destroy this stable dome we use an air blower as an external force, because it has less effect on the packing fraction [16] than the alternative methods (*e.g.* vibration or hitting the silo walls) which can affect the volume fraction of the grains inside the silo [54]. The air blower is mounted at (5 ± 0.5 bar) beneath the orifice and connected to the computer through an electronic valve. When the dome is established and the outflow is arrested for 5 seconds, the computer automatically gives an electronic signal to the valve, an air flush destroys the dome and discharging starts again.

By using the scale, the avalanche size S, *i.e.* the number of falling grains between two successive clogging events is calculated and stored in the computer. The avalanche mass is divided by the mass of a single grain. The scale can detect exact avalanche sizes but not the exact time of an avalanche because the measured values are slightly retarded due to an accumulation time. For the avalanche statistics, this is irrelevant. For measurements of flow rates, the exact duration of each avalanche is needed. Because of the retarded response of the scale, a microphone is used to measure the corresponding time for the avalanche [58].

Electronic parts in this setup (balance, valve and microphone) are connected by computer and controlled using a (*LabVIEW*) program. We perform our experiments at constant room temperature 23 ± 2 ℃ and humidity between 30% and 60%.

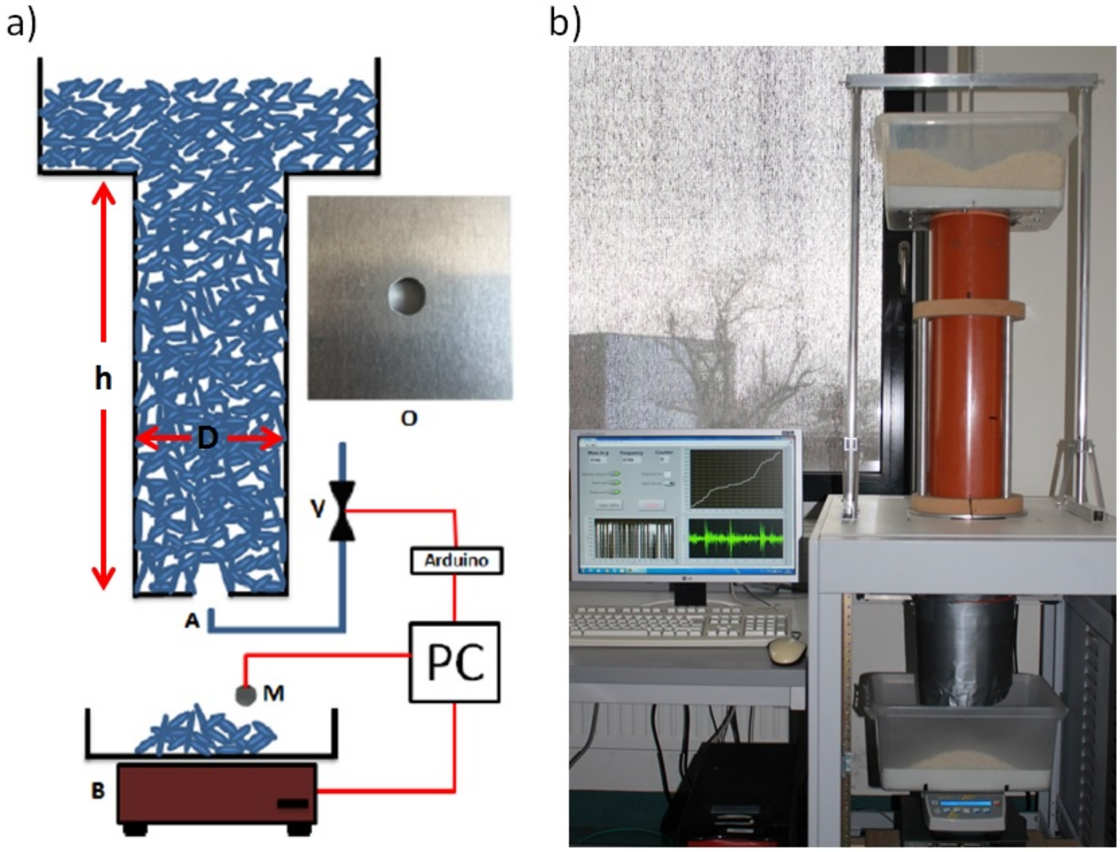

Figure 2.1: (a) Sketch of the experimental 3D flat silo setup, similar to [87]. h, silo height; D, silo diameter; V, electronic valve; A, air jet; M, microphone; B, balance; O, orifice. (b) Photograph of a typical setup.

2.1.2 Material

So far, most studies of silo discharge have dealt with simple sphere-shaped grains. To understand the effect of the grain shape parameter on the avalanche statistics and flow rate, the silo is loaded with materials of different shapes and sizes. We started with perfectly monodisperse spherical airsoft bullets and compared them with elongated particles different in aspect ratio $Q = \ell/d$, where ℓ is the length of the long axis and d is the diameter. Fig. 2.2 shows the grains used in this part.

For elongated particles we define an equivalent radius r_{eq} as the radius of a sphere with the same volume. In case of cylindrical shape

$$r_{eq(cyl.)} = \sqrt[3]{\frac{3}{16}\, d^2 \,.\, \ell}\ , \tag{2.1}$$

and

$$r_{eq(ellip.)} = \sqrt[3]{\frac{1}{8}\, d^2 \,.\, \ell} \tag{2.2}$$

for the ellipsoid rice grains. We will show later that there are other definitions for the equivalent radius which more reliably explain the clogging behavior of the elongated particles.

In this chapter, two types of cylindrical glass rods with different aspect ratios ($Q = 1.2$ *and* $Q = 3.5$), nearly ellipsoid rice grains ($Q \approx 3.6$), three cylindrical plastic rods with aspect ratios ($Q = 6,\ Q = 8$ *and* $Q = 12$) and monodisperse spherical air soft balls ($Q = 1$) are investigated. Table 2.1 shows all the information about these particles.

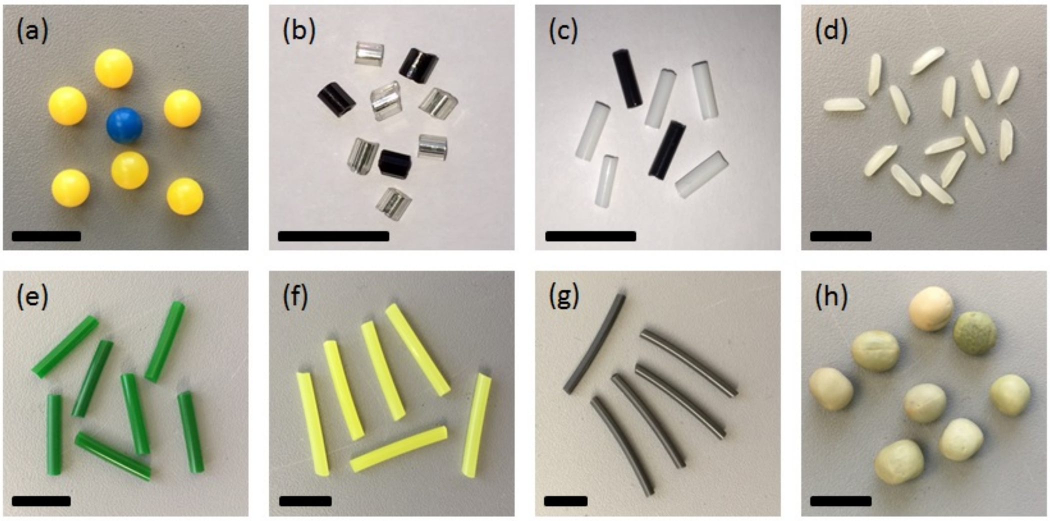

Figure 2.2: Images of particles studied, listed in Table 2.1: (a) spherical airsoft balls with aspect ratio $Q = 1$, cylindrical glass rods (b) $Q = 1.2$, (c) $Q = 3.5$, (d) rice grains $Q \approx 3.6$, plastic cylinders (e) $Q = 6$, (f) $Q = 8$, (g) $Q = 12$, and (h) peas $Q \approx 1$. The horizontal black bars mark 1 cm.

Set	Material	ℓ [mm]	d [mm]	r_{eq} [mm]	$Q = \ell/d$	Mass [mg]
a	Airsoft balls		6±0.036	3	1	120
b	Glass rods	2.2±0.3	1.9±0.2	1.1	1.2	12
c	Glass rods	6.6±0.45	1.9±0.2	1.65	3.5	33
d	Rice	7.2±0.52	2 ±0.18	1.5	3.6	18
e	Plastic rods	14.4±0.32	2.4±0.18	2.49	6	72
f	Plastic rod	19.2±0.38	2.4 ±0.18	2.75	8	99
g	Plastic rod	24±0.42	2±0.16	2.62	12	91
h	Peas		7.6±0.23	3.8	≈ 1	253

Table 2.1: Data of the grains listed in Fig. 2.2. ℓ is the long axis of the elongated grains and d is the short axis or the diameter in case of spherical grains. r_{eq} is the equivalent radius of a sphere with the same volume or radius of spherical grains. $Q = \ell/d$ is the aspect ratio.

2.2 Results and discussion

2.2.1 Avalanche statistics

We define the avalanche size as the number of grains falling down between two clogging events when the orifice size is not much bigger than the particle size. A strong correlation appears clearly between the avalanche size and the outlet dimensions. If the orifice size is increased the avalanche sizes become larger. In order to produce reliable statistics we have to have thousands of avalanches for each orifice. For small orifices we can get 10000 avalanches within a few silo fillings and in a short time but for large ones we struggle to get around 1000 avalanches. The silo setup has to be refilled hundreds of times to get reliable statistics for the mean avalanche size corresponding to each outlet size. In each run, we keep a sufficient amount of grains inside the tube to avoid emptying of the silo.

The avalanche size S comes direct from the $m(t)$ graph, Fig. 2.3.(a), where m is the weight of the grains measured by the scale. This figure shows data of one run for cylindrical glass rods with aspect ratio $Q = 3.5$ at an orifice radius $R = 5.7$ mm. If we zoom in on the thick red box, we can distinguish between the avalanches (see Fig. 2.3.(b)). The horizontal steps indicate clogged states; no change in the scale reading for around 5 seconds. Red angles indicate the triggered pulses to the electronic valve, letting the air pressure come out and destroy the dome (*i.e.* the clogged structure above the orifice).

By knowing the total mass of particles m between two successive horizontal steps and the individual particle mass m_p, we can determine the avalanche size $S = m/m_p$. A sequence of 10000 discrete avalanches for the glass rods ($Q = 3.5$) through an orifice with radius $R = 5.7$ mm is illustrated in Fig. 2.4.(a).

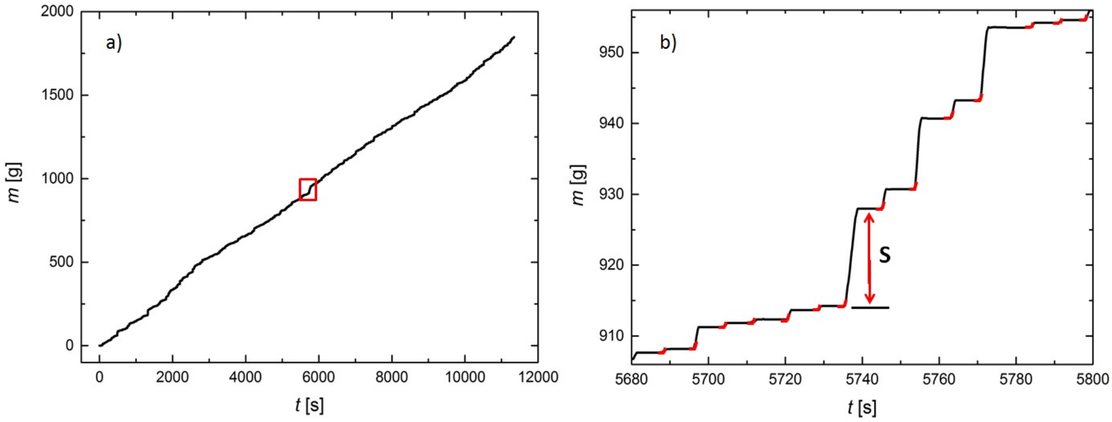

Figure 2.3: (a) The graph represents thousands of avalanches in one run for cylindrical glass rods with aspect ratio $Q = 3.5$ at an orifice radius $R = 5.7$ mm. (b) Detail of the m(t) curve in the red labeled box in (a).

For statistics it is important to know if each avalanche represents an independent event. The correlation between successive avalanches has been checked (See Fig. 2.4.(b)), in this map we can see there is no clear dependence between avalanche size S_n and the subsequent S_{n+1}. Let us assume that particles pass an orifice in a hopper. The probability that a certain particle forms a clog and ends the flow through the orifice is

$$p^{'} = (1 - p), \tag{2.3}$$

where the probability that it passes the orifice is thus p [16]. Let us postulate that the conditions remain constant, meaning there is no ageing in the system. Then the probability that the system clogs after s passing particles, *i.e.* the probability of an avalanche with exactly S particles to occur is

$$p(S) = p^S(1 - p) \tag{2.4}$$

In some places, I will use for convenience the substitution

$$p = exp(-1/S_0) \tag{2.5}$$

with the new variable S_0. The probability of an avalanche having size S is then

$$p(S) = exp(-S/S_0)[1 - exp(-1/S_0)] \tag{2.6}$$

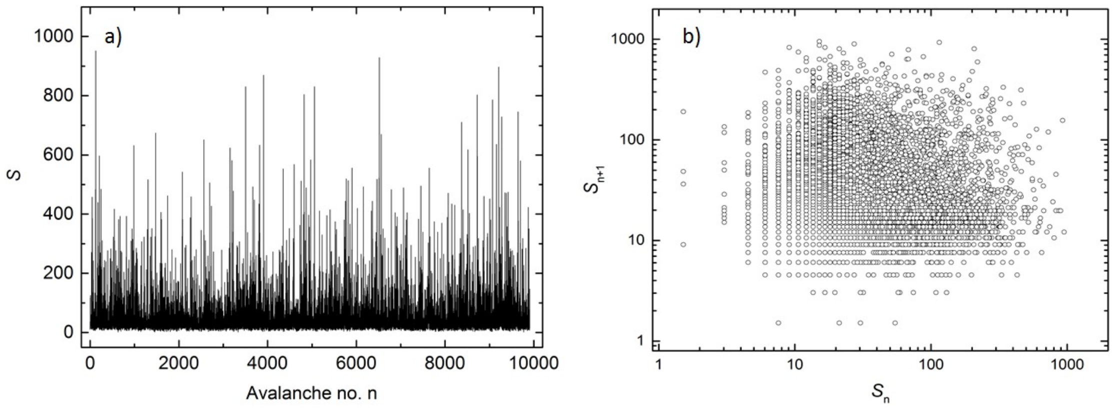

Figure 2.4: (a) Histogram of the sequence of avalanche sizes S_n, cylindrical glass rods with aspect ratio $Q = 3.5$ at an orifice radius $R = 5.7$ mm. (b) Test of the correlation between sizes of subsequent avalanches, similar to [87].

Note that

$$\sum_{S=0}^{\infty} p^S = \frac{1}{1-p} \quad \text{and} \quad \sum_{S=0}^{\infty} n(S) = 1$$

When S_0 is large enough, one can expand the exponential function in the first term and truncate to

$$p(S) = \frac{1}{S_0} \exp(-S/S_0) \tag{2.7}$$

In our experiment we found that two different parts for the avalanche distribution are separated by a vertical dotted line, illustrated in Fig. 2.5. The second part after the vertical dashed line decays exponentially and satisfactorily agrees with Eqn. 2.7. On the left of the dashed line we can see some small avalanches with high probability increasing with S. However we could not see avalanches at fewer than 10 particles. The used air blower as an exciter as in ref. [58] to destroy the dome above the orifice probably lower the packing of particles above the orifice, so that small avalanches of a few grains become extremely rare. It will be more accurate when evaluating the mean avalanche sizes to cancel the small avalanche data and only fit the exponential part, especially with small orifices. The behavior of the second part with high avalanches has been checked for different materials at different orifice sizes R, and all of them take an exponential decay, which means that the probability of clogging is constant for each particle. The inset of Fig. 2.5 shows 1-$x(S)$ in a logarithmic scale as a function of the avalanche size S, where $x(S)$ is the cumulative probability function of avalanches having a size smaller than S. 1-$x(S)$ takes an exponential shape and the deviations appear in the upper part of the curve for small avalanches and in the lower part where we have some large avalanches that occur with lower probability than expected.

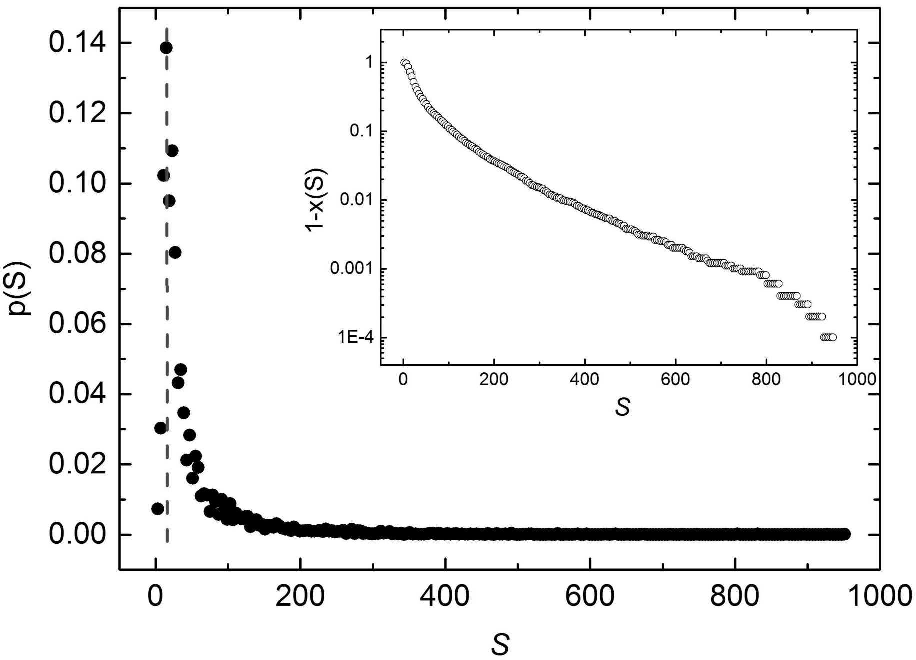

Figure 2.5: Probability of avalanches with size S between two successive clogs for cylindrical glass rods with aspect ratio $Q = 3.5$ and orifice radius $R = 5.7$ mm. The inset shows the cumulative distribution of avalanches having smaller sizes than S. Similar to [87].

2.2.2 Existence of a critical radius and the aspect ratio of grains

The mean avalanche size $\langle S \rangle$, the average number of the grains which falling down between two successive clogging events has a strong relation with the orifice radius R. When the orifice size becomes larger, the probability of clogging decreases and $\langle S \rangle$ increases [58]. We conducted our 3D fixed size silo experiment with different types of anisotropic grains with cylindrical and ellipsoid shape and compared them with monodisperse airsoft balls, the information about the materials is listed in Table 2.1.

Initially, we rescaled the orifice radius by dividing it with the equivalent radius r_{eq} of the sphere with the same volume. Despite the significant contrast in the meaning between Eqn. 1.1 and Eqn. 1.2, within our experimental data we could not discriminate between the power law model behavior Eqn. 1.1, which means there is a critical orifice size R_c after which the mean avalanche size diverges, and the exponential model Eqn. 1.2. This is because we have some limitations which govern the experiment (*e.g.* silo size and the amount of the materials). Fig. 2.6 shows the data for cylindrical glass rods ($Q = 3.5$), both models have been tested for all the investigated particles and they fit our data with high significant precision. In order to distinguish between the two models, many experiments with large orifices and recording enormous avalanche sizes would be required. The fitting parameters for the two models are listed in Table 2.2.

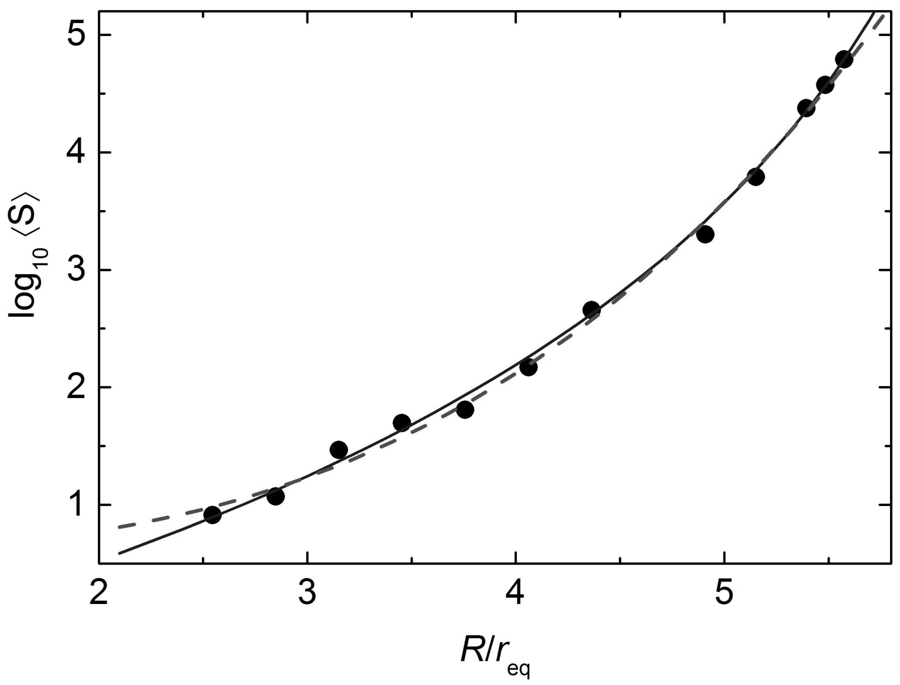

Figure 2.6: Mean avalanche size $\langle S\rangle$ vs R/r_{eq} for cylindrical glass rods with aspect ratio $Q = 3.5$. The solid curve is a fit with Eqn. 1.1 at $\beta = 7$ and the dashed curve with Eqn. 1.2. Within the statistical accuracy of the data, we cannot distinguish between the two models. Similar to [87].

In Fig. 2.7.(a), we can see the data for the mean avalanche sizes with materials of different aspect ratios as a function of (R/r_{eq}), the orifice radius rescaled by the equivalent radius of a sphere with the same volume as a first approximation. A strong relation between $\langle S\rangle$ and the relative orifice radius appears clearly. When the aspect ratio Q increases, the mean avalanche size for the given values of (R/r_{eq}) gets smaller and the corresponding clogging probability increases. That means, when the granulate becomes more elongated, the possibility increases of establishing the dome above the orifice which arrests the outflow more than in the case of short particles. By applying Eqn. 1.1, the critical orifice size corresponding to each type of grains increases with their aspect ratio Q, illustrated in Table 2.2 and the rescaled critical orifice size as a function of the aspect ratio Q for the different types of grains is presented in Fig. 2.8.

The shape parameter also has been checked in this work by using ellipsoid rice grains ($Q = 3.6$) and smooth cylindrical glass rods ($Q = 3.5$), they have almost the same aspect ratio but are quite different in structure. Moreover we did not remark a significant difference between their clogging behavior.

A new reliable definitions for the equivalent radius of anisotropic particles have been introduced in Fig. 2.7 (b) and (c), to scale all our data in one master curve.

Material	Q	R_c	$\ln A$	$\ln c$	a	χ	$Q^{1/6}$	$r_{eq}^{(A)}$ [mm]
Airsoft balls	1	4.95	8.84	0.527	0.135	1	1	
Glass Rods	1.2	5.76	10.55	0.865	0.091	1.1	1.03	1.15
Glass Rods	3.5	6.74	12.1	1.36	0.055	1.25	1.23	1.99
Rice grains	3.6	6.51	10.85	0.40	0.062	1.28	1.24	1.90
Plastic rods	6	12.3	16.3	(0.48)	(0.015)	1.5	(1.34)	3.32
Plastic rods	8	14.7	17.9	(0.58)	(0.011)	1.55	(1.41)	3.83

Table 2.2: The fitting parameters for the mean avalanche size models, Eqn. 1.1 and Eqn. 1.2, and the values of $r_{eq}^{(A)}$.

First in (b) we used the following empirical equation

$$r^*_{eq} = \chi \; r_{eq}, \tag{2.8}$$

where χ is a variable dependent on the aspect ratio. This equation collapses the mean avalanche size data for all investigated particles with aspect ratio ($Q < 6$) to one master curve and for the grains with ($Q = 6$ and 8), it brings only the first data part for small avalanches. In that case also χ increases systematically with Q (see Table 2.2).

The values of χ can be expressed as a function of the aspect ratio Q. The best values of χ have been found by using Eqn. 2.9

$$\chi = Q^{\;0.21 \;\pm\; 0.02} \; . \tag{2.9}$$

The new rescaling equivalent radius r^*_{eq} in Eqn. 2.8 has succeeded in fitting only the avalanches data of the grains with aspect ratio < 6, and the power of Q is very close to 0.1666. That suggested a new interpretation, namely that 1/6 can be used as a reasonable power for Q. Together with Eqn. 2.8 this means that one can choose a new equivalent radius which uses the combination of $r_{eq} \propto \ell^{\frac{1}{3}} \; d^{\frac{2}{3}}$ and $\chi \propto \ell^{\frac{1}{6}} \; d^{-\frac{1}{6}}$ in Eqn. 2.9.

The radius of the sphere with the same cross section area is used as an alternative definition for the equivalent radius of the elongated grains (see Fig. 2.7.(c)). Where in case of cylindrical grains

$$r_{eq}^{(A)} = \sqrt{\ell \; . \; d/\pi} \; , \tag{2.10}$$

and

$$r_{eq}^{(A)} = \sqrt{\ell \; . \; d/4} \tag{2.11}$$

for ellipsoid grains, and (ℓd) represents the cross section area of the long plane which included the rotational axis. However this definition also could not fit well

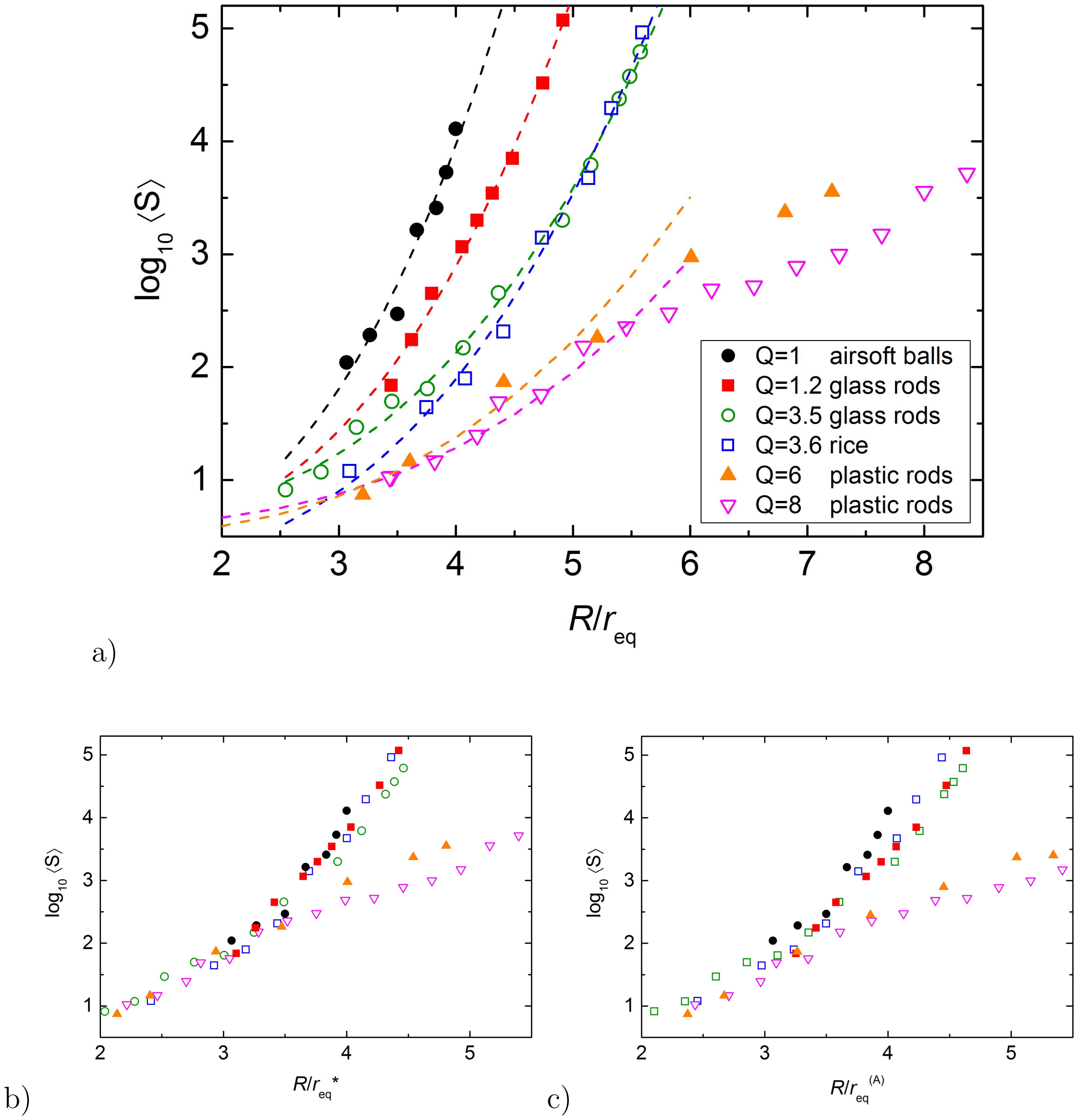

Figure 2.7: (a) Experimental data for $\log_{10}\langle S\rangle$ versus R/r_{eq}, as a first rescale approximation for spherical and elongated grains with different aspect ratios. The dashed curves are fitted with the Eqn. 1.2. For the cylindrical rods with aspect ratio $Q \geq 6$, we fitted only the mean avalanche size data of the small orifice sizes up to $R/r_{eq} < 5$. The mean avalanche size for given R/r_{eq} decreases with increasing the aspect ratio. (b) The same experimental data with the second rescaled approximation r^*_{eq}. This rescaling works only for elongated grains with $Q < 6$. (c) Same data rescaled with the third approximation of the equivalent radius r^A_{eq}. Similar to [87].

the data of the grains with ($Q \geq 6$), but in spite of the latter, it is more realistic when we compare the mean avalanche size of anisotropic grains, to rescale the orifice radius by the equivalent radius of sphere with the same cross section, not the same volume.

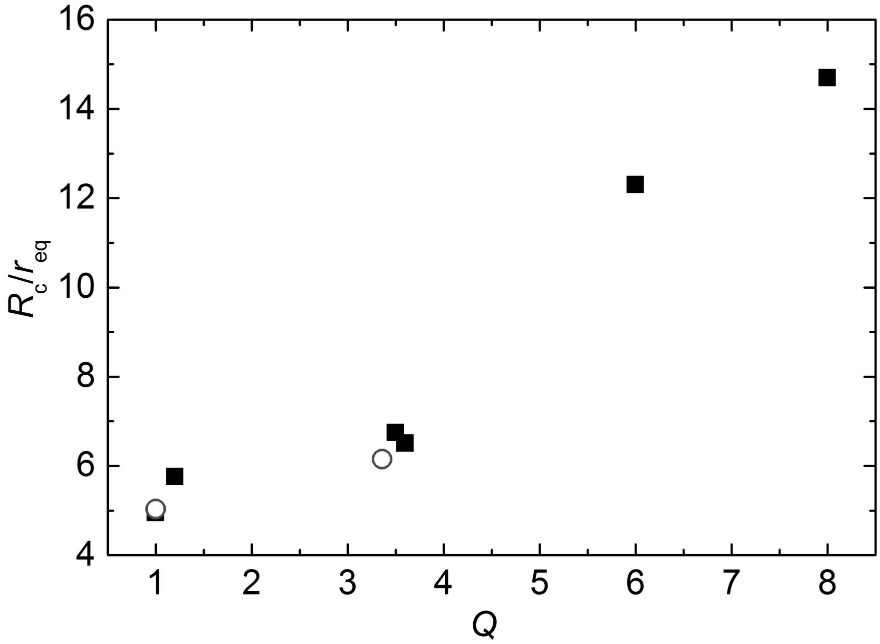

Figure 2.8: Rescaled critical orifice size R_c for different grains vs. aspect ratio. Solid squares: our experimental work, open circles: Ref. [58]. Similar to [87].

2.2.3 Elongated particles and rat-holes

The opportunity for anisotropic grains with high aspect ratio to move in a silo during the avalanches is not as simple as it is with spherical particles. When we start to freshly fill the 3D silo, all grains at the beginning are highly disordered and have a random orientation. When our trigger system starts to destroy the block of particles above the orifice, the first avalanches are very small compared to the next and this as a result of the random packing, so it takes a time to make an empty space above the orifice and let the grains become aligned by shear flow toward the outlet. Experimental data for $Q = 8$ plastic rods are presented in Fig. 2.9, the different colors are for different orifice sizes and all of them with small avalanches compared with the monodisperse airsoft balls (the thick blue curve), which have a homogeneity in the avalanche distributions. So it would be better for a good statistical result to discard the first avalanches of the elongated particles or, at least, treat them separately.

The study of anisotropic grains has still its enigmas and shows new phenomena that have an effect on the avalanche statistics. When we went to study the plastic rods with ($Q = 12$), a new phenomenon appeared clearly and had a major effect

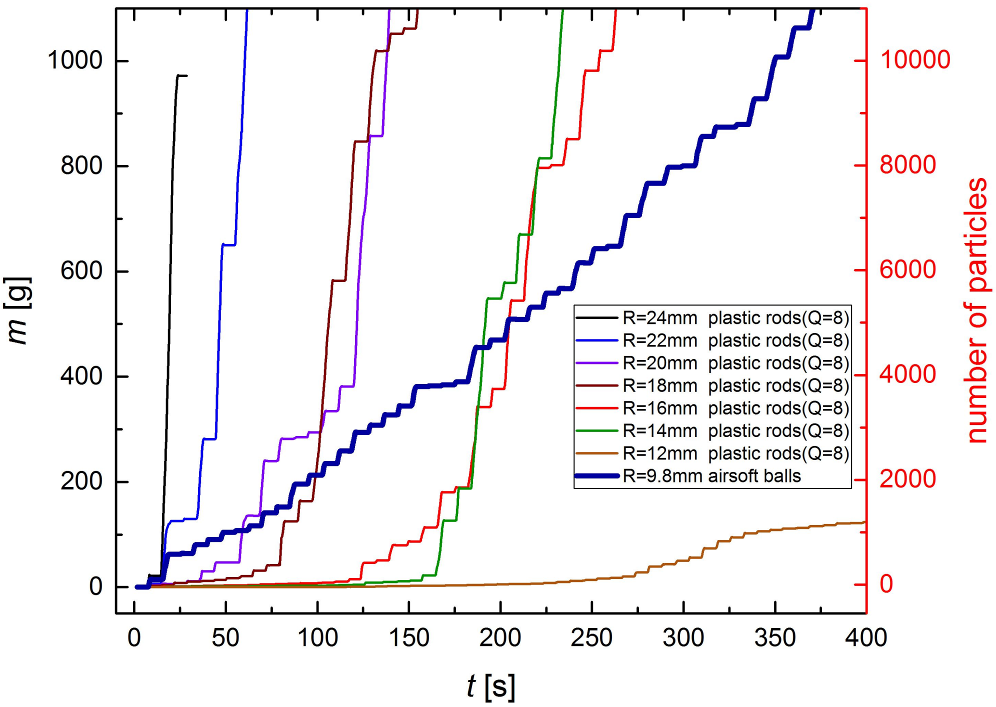

Figure 2.9: Discharged materials from a silo after fresh filling with plastic rods ($Q = 8$). Horizontal steps represent the clogged states between two successive avalanches. The thick blue curve shows a typical discharge of airsoft balls. Note the transients for the elongated grains. Similar to [87].

on the dynamics of our silo. The normal curve $m(t)$ was plotted (see Fig. 2.10), small avalanches occur as under the influence of the air blower and after a certain time span there were no more avalanches and our trigger system was useless. On checking the silo, it was apparent that there was a long vertical tunnel above the orifice penetrating all the granular bed. In Fig. 2.11 we can see this ″rat-hole‟that started at the orifice and grew until it reached the upper surface of the grains, which cover nearly 90% of the silo height and no appearing avalanches any more.

The granular bed around the tunnel is stable and this can be compared with the stability of elongated particle towers with high aspect ratios, which were described before in Ref. [116]. The rat-hole appears also for $Q = 6$ and $Q = 8$ particles with a short tunnel (see Fig. 2.11.(a)). It could be the deviation in their curves from the master curve in Fig 2.7 at the big orifices takes place as a result of the stability of the rat-hole wall. More investigations are needed to understand this phenomenon and discover the effective parameters which govern it (*e.g.* silo diameter).

Another wider silo with diameter ($D = 235$ mm) and height ($h = 600$ mm) was used for checking the existence of the rat-hole with ($Q = 12$) particles. It was surprising to note that we still have this rat-hole but in this case with short granular bed (≈ 200 mm) height. Now we can say that the silo dimensions have a strong effect on the granular bed for the grains with high aspect ratio (see Fig. 2.12).

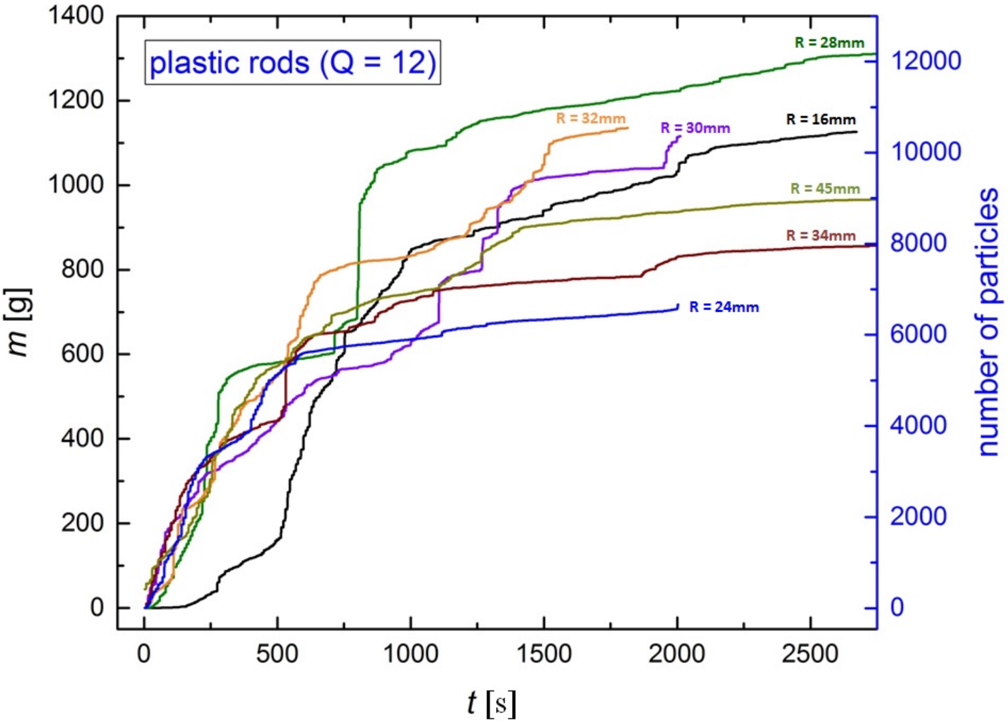

Figure 2.10: Discharge after fresh filling. The vertical tunnel above the orifice grows with each triggered avalanche. When the ″rat-hole‟ reaches the top surface, the outflow stops completely, even with air pulses. Similar to [87].

2.2.4 Outflow velocity and Beverloo's equation

The mass flow rate of the outflow grains from a 3D silo was calculated by knowing the particles mass, given by the scale and its time duration by the microphone. We measured this flow rate in two different areas. One at the small orifices where we have a discrete flow rate because of the clogging events and the second at continuous flow when the orifice radius $> R_c$ (critical orifice size). For both regimes, Beverloo's law (Eqn. 1.3) is appropriate to fit our data with exponent 5/2 at high accuracy [49], even for the elongated particles until $Q \approx 6$. The flow rate data in Fig. 2.13 shows the best fits by using the following equation

$$V = W/m_p = \Gamma' \left(\frac{R}{r_{eq}} - k \right)^{5/2}, \tag{2.12}$$

with particle mass $m_p = (4\pi/3)\, r_{eq}^3 \rho$. In that case the relation between Beverloo's constant Γ in Eqn. 1.3 and Γ' is

$$\Gamma = \frac{\pi\sqrt{2r_{eq}}}{6\phi\sqrt{g}} \Gamma', \tag{2.13}$$

where ϕ is the packing fraction of particles inside the silo. We estimate ($\phi \approx 0.6$) as in the case of spheres [117]. However, the packing fraction of elongated particles can

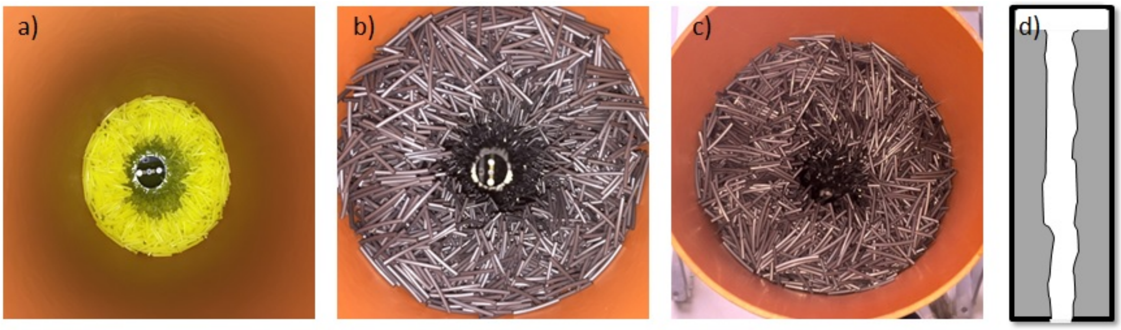

Figure 2.11: Top view of ″rat-hole‶ inside the 3D silo with $R = 32$ mm: (a) Plastic rods of aspect ratio $Q = 8$ the height of the granular bed around 200 mm. (b) and (c) Plastic rods of aspect ratio $Q = 12$, the height of the granular bed in this case around 550 mm and ″rat-hole‶ penetrates nearly all the silo. (d) Sketch of the rat-hole.

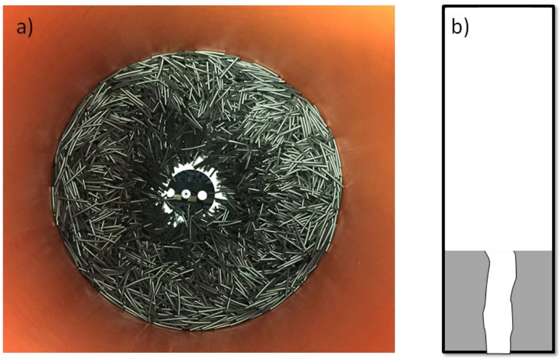

Figure 2.12: (a) Rat-hole image of plastic rods with aspect ratio $Q = 12$ in a wider silo with diameter ($D = 235$ mm) and height ($h = 600$ mm) at an orifice radius ($R = 24$ mm). (b) Sketch of the rat-hole.

be lower than this value due to the random orientations [118, 119], but it recovers again by shear induced alignment during the discharge [86].

The flow rate data as a function of the relative orifice size for different aspect ratio grains is presented in Fig. 2.13. The flow rate for long particles with high aspect ratio shows a decrease in the flow rate than the short ones at given R/r_{eq}, but there was no noticeable difference for the shape effect between the cylindrical glass rods and the ellipsoid rice grains, which have the same aspect ratio. In Table 2.3 we can see a strong relation between the dimensionless constant k and the aspect ratio Q. Its values increase systematically with Q. This means in Beverloo's equation, the long axis of the grains has a more significant influence than the two short axes. If you try to replace d, the sphere diameter, in Eqn. 1.3 with an equivalent parameter of the elongated particles, you need to choose one larger than the average value of the three particle dimensions. Now it is clearer why Beverloo's equation does not fit the $Q = 8$ particles, even if we redefine the equivalent radius.

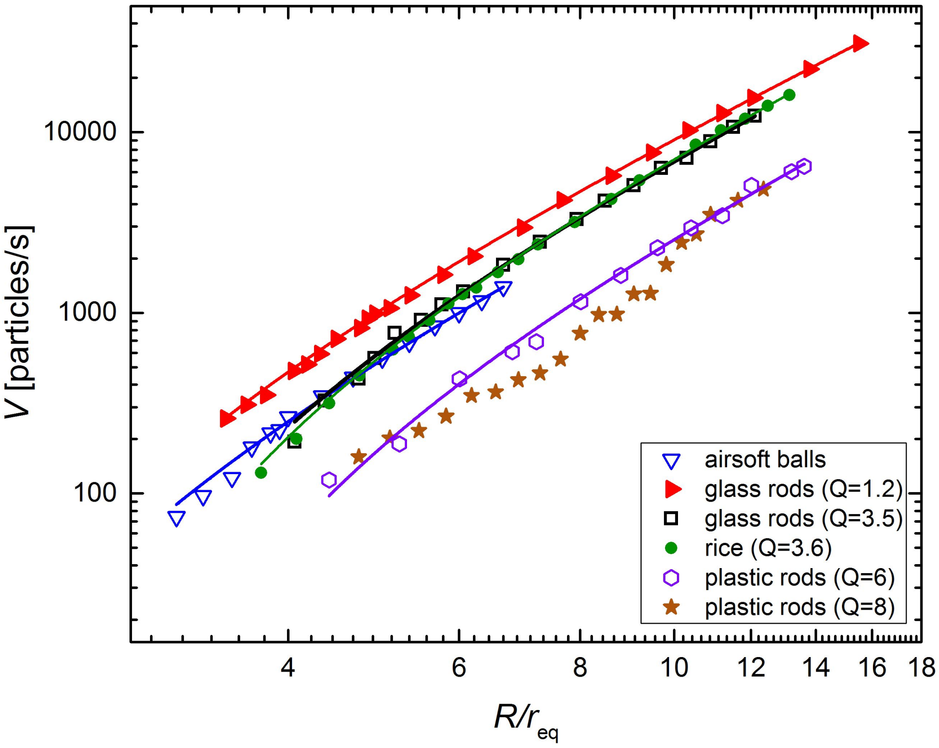

Figure 2.13: Double logarithmic scale of the flow rate vs. R/r_{eq} for different particles. All these data are fitted using Eqn. 2.12 except $Q = 8$ rods.

Material	Q	Γ' [1/s]	r_{eq} [mm]	k	$\Gamma \cdot \phi$
Airsoft balls	1	20.7 ± 0.5	3.0	1.29 ± 0.04	0.268
Glass Rods	1.2	41.2 ± 0.3	1.1	1.35 ± 0.04	0.325
Glass Rods	3.5	36.9 ± 0.8	1.65	1.91 ± 0.07	0.355
Rice grains	3.6	39.9 ± 0.6	1.5	2.0 ± 0.06	0.365
Plastic rods	6	15.5 ± 1.2	2.55	2.3 ± 0.3	0.185

Table 2.3: Fitting parameters for Eqn. 2.12. The values of $\Gamma\phi$ listed in last column by knowing r_{eq} and Γ' in Eqn. 2.13.

3 Effects of lateral walls on 2D silo

In 3D-silos, there are some limitations in the study of all the parameters affecting the avalanche statistics and the velocity field. In order to observe the particle motion inside, we need a special imaging technique such as X-ray tomography to scan all the particles in the silo. For these reasons most experiments in literature were run in 2D or quasi-2D silos so that one can easily observe what is happening inside.

We studied and investigated the influence of changing the lateral walls position on several parameters which govern the avalanche statistics and the arch shape by conducting a 2D-silo experiment. Of particular interest is the limit of small lateral silo extensions, and the influence of lateral boundaries.

3.1 Narrow 2D-silo experimental setup

The experimental 2D flat bottom silo setup consists of two identical 10 mm thick rectangular glass plates with width 350 mm and height 800 mm. Two stainless steel strips with thickness 1.0 mm were inserted vertically between the plates and tightly sandwiched between them. These strips were used not only to control the silo thickness but also as movable lateral walls to change the silo width from 6 mm to 280 mm (see Fig. 3.1).

The glass plates are positioned on a stable metal bench. On this bench there are two metal pieces controlling the orifice size. The two pieces are horizontal and their edges were cut at an angle of 45° downward to prevent any arching between them. We chose and fixed a central outlet with size $D = 4.32 \pm 0.02$ mm by gluing the two pieces in the holding bench and they are slightly raised into the silo.

The silo was loaded by stainless steel monodisperse beads with diameter $d = 1.00 \pm 0.01$ mm, friction coefficient 0.33 ± 0.02 and mass $m = 4.00 \pm 0.01$ mg by using a hoper above the silo [16, 18]. After filling it, several test runs were performed to check that all beads covered the whole silo in a monolayer form and moved freely during the outflow.

The orifice size was chosen carefully to be suitable for registering thousands of avalanche for each silo width and also for recording videos during the outflow without any interruptions. The outlet is around 4 beads in diameter to allow the particles meet and clog the orifice in appropriate time.

An appropriate LED white light was used from behind to illuminate the outlet surrounding area, and make an obvious contrast between the beads and the background to facilitate the detection process.

Beneath the orifice, we put a cardboard box above an electronic scale to collect all the beads which freely flew down under gravity. We used a scale (AND GX-4000) with an accuracy of 1 mg, to be able to detect one single bead (4.00 mg) and it is connected direct to the computer.

An air blower was used to destroy the blocked arch and let the grains flow out again. This technique was used because it has less effect on the packing fraction [16] than the other methods (e.g. vibration or hitting the silo walls) which could alter the volume fraction of the grains inside the silo [54]. Air pressure was adjusted to 4.0 ± 0.5 atm and controlled by a computer through a valve. Its duration was 0.4 ± 0.1 seconds according to ref. [58], where there is no significant effect on the avalanche statistics by changing its magnitude or duration. The experiment was executed in two different ways as described in sections 3.1.1 and 3.1.2.

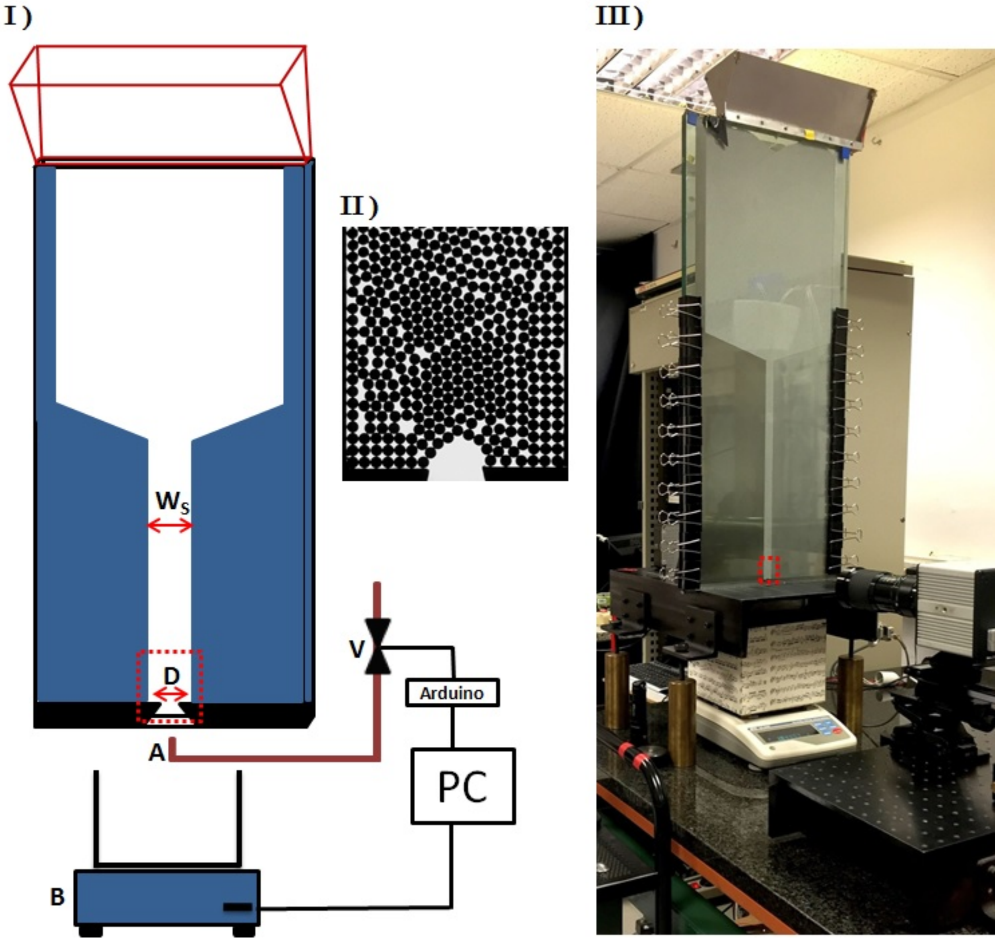

Figure 3.1: (I) Sketch of the exchangeable width 2D flat bottom silo setup. Orifice diameter D, exchangeable silo width W_S, air blower A, electronic valve V and electronic scale B. (II) One of the registered arch images by the camera is indicated approximately by the red dotted area. (III) Photograph of the experimental setup.

3.1.1 Calculating the avalanche size and imaging the blockage arch

The avalanche size S was calculated using the known mass of beads which flew down between two successive clogs, where we divide the avalanche mass by the bead mass. In this experiment we fixed the orifice size at a certain value to allow several avalanches to be recorded in one run.

Once the experiment was set in motion, the grains flew out freely under gravity and their mass was recorded by the balance beneath the orifice. The silo was refilled continuously when the grains level fell below 300 mm.

Once the outflow had been arrested as a result of an established arch which blocked the outlet, a picture was taken for each arch corresponding to the end of one avalanche event and registered on the computer by using a CCD camera ″DMK 31BU03‶ with maximum resolution 1024 x 768 pixels. This camera was placed directly in front of the silo and focused on the area surrounding the outlet. When the outflow was arrested by the arch and there had been no change in the reading from the electronic scale for 5 seconds, a triggered air pressure pulse came out from the blower beneath the silo and destroyed the arch, letting the outflow start again. These processes were controlled by a LabView program which was used to record the avalanche sizes coming from the scale. It also gave the signal to the air blower and registered the arch images.

In this part, thirteen different silo widths are presented. For each silo width we recorded around 2000 avalanches to get good statistics.

3.1.2 Recording high-speed outflow videos

For the second stage of the experimental work in this chapter, we recorded high-speed videos of the outflow using ″Photron Fast Cam-1024 PCI 100K‶ with maximum resolution 1024 x 1024 pixels. The fast camera stayed in front of the setup and focused on the orifice area and its surrounding. All the recorded movies were taken during the outflow without any intermission and after 5 seconds from the beginning to make sure we had a steady flow. Each movie was taken at 4 second time intervals and registered 2000 frames per second. Eight different silo widths were chosen for recording videos and for each one 10 movies were produced.

3.2 Imaging analysis

We used the image processing toolbox in MATLAB for handling and coping with the arch images. Two different methods were checked to find the positions of all beads inside each photo and after that to detect the beads which belong to the arch.

For measuring the mass flow rate, a MATLAB routine was written to track the particles in each frame of the outflow video and count the number of particles which passed the outlet in one second.
Finally, a ″$coarse - graining$‶ technique [45] was used for measuring and showing the continuous velocity field inside the silo.

3.2.1 Particle detection

Our 2D setup was illuminated by using LED white light from behind. This light passed through the empty spaces between the particles and lit them. In the images registered by the camera in front of the silo, the empty gaps appeared as a bright region and the particles as a dark one (see Fig. 3.2.(a)). Therefore it was easy to distinguish between the particles. All the registered images contain around 25 beads above the orifice line and 3 bead diameters below this line, so it is easy to count the number of beads which leave the orifice. The beads centroids were calculated by using two different methods:

1. **Hough transform:**
    - In this method we used the ″$imfindcircles$‶ function which is built in MATLAB, to determine the beads and their centroids. This function takes grayscale images and uses the circular Hough transform to find the circular particles at a given radius. In the written code we adjust ″*EdgeThreshold*‶ to 0.05. The centers of the beads are indicated by red-plus symbols in Fig. 3.2.(b) and the particles are contained within red rings.
2. **Erosion method:**
    - The first step in this method was to transform the grayscale image to a binary image, represented in Fig. 3.2.(c). This image has only two values 0 and 1. The ″$graythresh$‶ function in MATLABA was used for computing a suitable gray-threshold value. When the pixel intensity has a value greater than the threshold, this pixel takes 1 which means bright (gaps), and when its value is less than the threshold it takes 0 which means dark (particles).
    - In Fig. 3.2.(d) we inverted the binary image (*i.e.* the pixels with values 1 became 0 and 0 became 1). In that case the particles appeared white and the gaps between them were dark.
    - After that, the ″*imerode*‶ function was used to make an erosion by using a structure element as a disk with size 80% of particle diameter. This disk was scanned over all the pixels in the images and separated the particles from each other and indicated them by white spots (see Fig. 3.2.(e)). The particle centroids were calculated and represented by x-green symbols.

The two methods were checked, and both of them determined the centroids of the beads with a significant accuracy. Fig. 3.2.(f) shows the calculated bead centroids by the two methods, which are superimposed on each other and presented on the original grayscale image.

3.2.2 Particle tracking

After detecting the centroids of the particles in each image by using Hough transform, a MATLAB code was written to track all the particles in each individual image of each registered high-speed movie. The tracking program was based on calculating the displacement between the positions of the particles in each successive image. The films were recorded at a speed high enough (2000 frames per second) to ensure that the displacement of the grains between two consecutive images is less than their own radius. The velocity of the particles between two frames can be calculated by multiplying their displacement with the camera frequency and then we extended this process for the whole of the video length.

A $''coarse-graining\ technique$ ‟ [84,120,121] was used for calculating a continuous solid density and velocity fields inside the silo. For this method, we chose our 2D $coarse - graining$ Gaussian function as:

$$\Psi[\vec{r} - \vec{r_i}(t)] = [1/2\pi\omega^2] exp(-|\vec{r} - \vec{r_i}|^2/2\omega^2), \tag{3.1}$$

where $\vec{r_i}$ is the position of the particle i, and the Gaussian rms value, ω, set equal to the grain radius. This selection was more reliable and solved the problem of the dependence of velocity profiles on the averaging domain size for large values which need a correction factor to decrease the error percentage [122], or the small values which did not give the intended smoothing. By knowing the $coarse - graining$ function Ψ, the 2-dimensional solid fraction $\phi(\vec{r})$ and the velocity field $\nu(\vec{r})$ were calculated by time averaging over all the temporal sequences for each silo width by using Eqn. 3.2 and Eqn. 3.3 respectively.

$$\phi(\vec{r}, t) = A_g \sum_{i=1}^{N} \Psi[\vec{r} - \vec{r_i}(t)], \tag{3.2}$$

$$\nu(\vec{r}, t) = A_g \sum_{i=1}^{N} \vec{\nu_i}\ \Psi[\vec{r} - \overrightarrow{r_i(t)}]/\phi(\vec{r}, t). \tag{3.3}$$

where A_g represented the xy-plane cross section area of the grains, and $\vec{\nu_i}$ is the instant velocity of each particle.

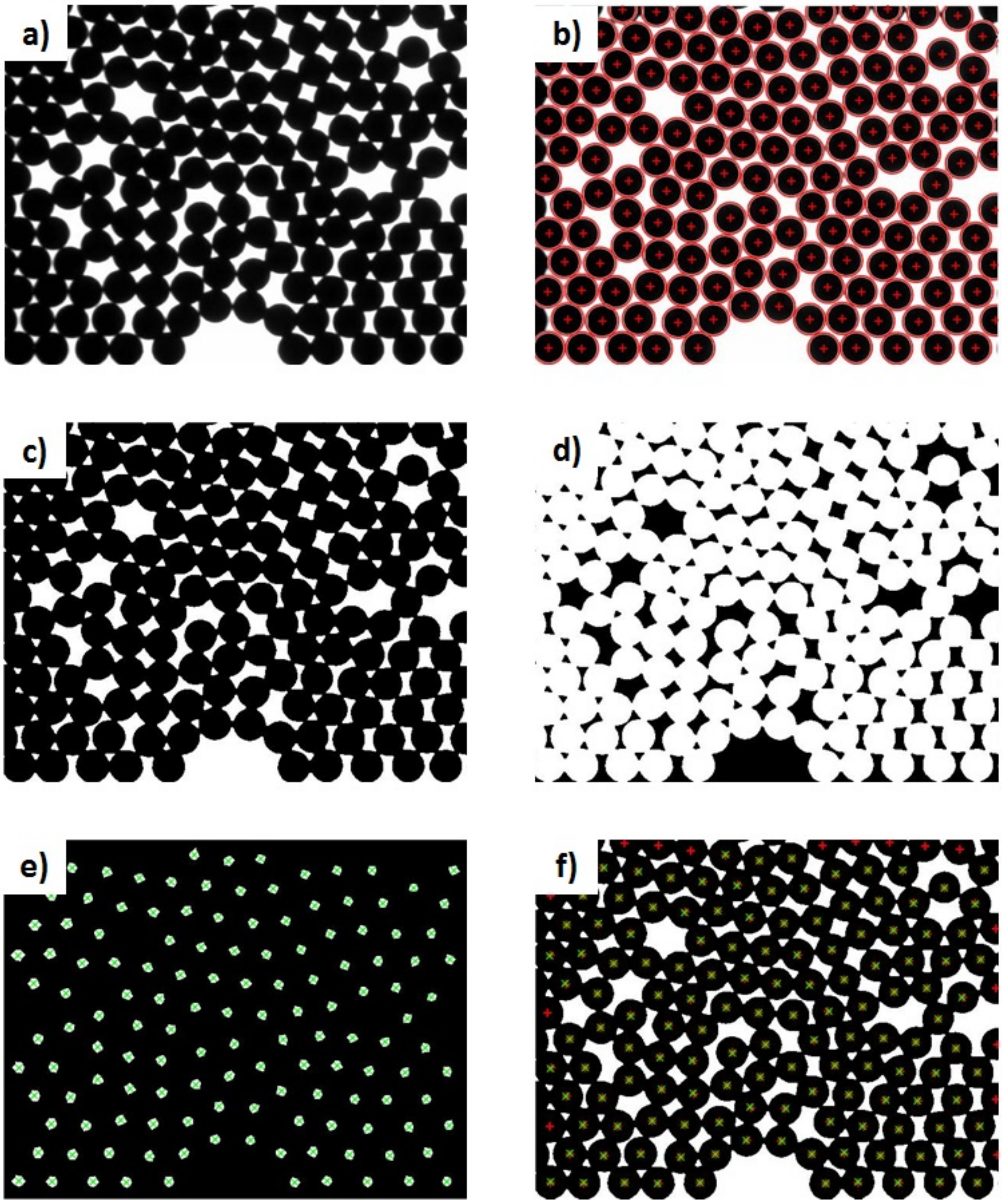

Figure 3.2: Digital processing of camera images. (a) Original arch grayscale image. (b) The particles are marked by red rings and their centers by red-plus symbols, using the Hough transform method. (c) The binary image of the original. (d) The negative binary image. (e) Eroded image, the particles centroids are marked by x-green symbols. (f) Superimposed image of the particle centers obtained with the Hough transform and erosion methods applied to the grayscale image.

3.3 Results and discussion

3.3.1 The position of lateral walls and the mean avalanche size

In the literature some parameters have been checked to see how they positively or negatively affect the clogging probability. All the experiments which ran before in 2D and 3D silos avoided the wall effect by choosing their silo widths greater than 30 grains in diameter [55]. In this section we investigate the influence of the position of the side walls on the avalanche sizes. The silo width W_S has been changed from a very wide one with $W_S = 280$ beads in diameter until it reached a very narrow channel with $W_S \approx 6$ beads in diameter, which means we have around only one bead between the orifice edge and the container wall on both sides (note the orifice width $D = 4.32$ mm). This width is represented in the inset of Fig. 3.3.

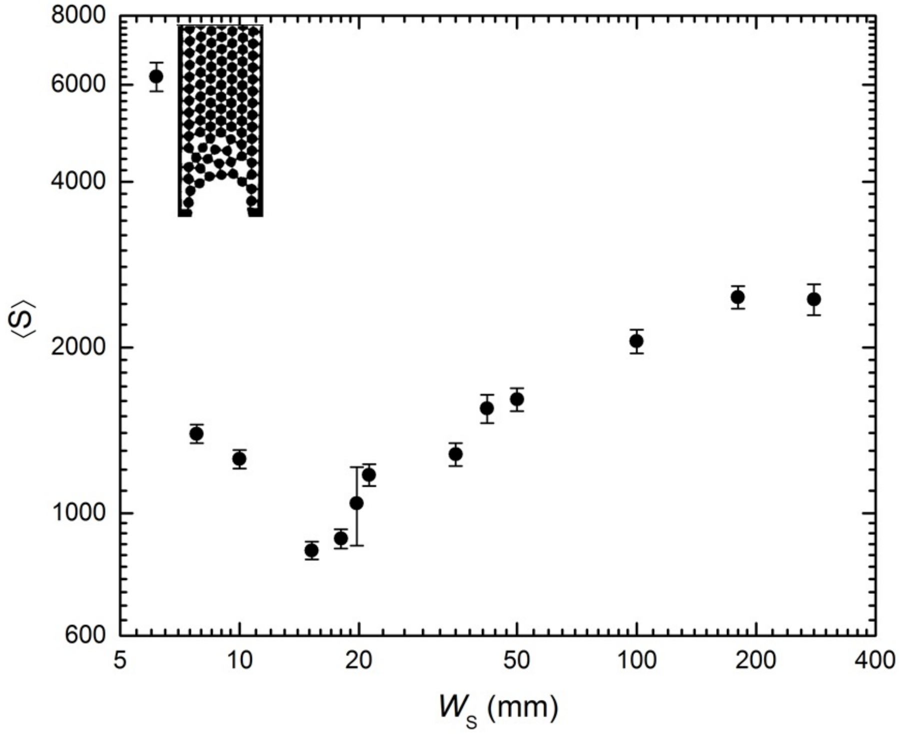

Figure 3.3: Mean avalanche size $\langle S\rangle$ versus the silo width W_S in double logarithmic scale at a given orifice size $D = 4.32$ mm. Similar to [46].

A significant and non-monotonical change in the avalanche size S was noted when the silo width was reduced. At that point, we can say there is a new parameter which can play an important role in changing the clogging probability that controls the avalanche size. In Fig. 3.3, the mean avalanche size is presented as a function of the silo width. For the widest silos in our experiment ($W_S = 280$ mm and 180 mm) the mean avalanche size was more or less the same and it decreased below these widths until it reached the minimum values at ($W_S = 18$ mm and 15.2 mm). After that $\langle S \rangle$ increased again with decreasing silo width and got the maximum value at ($W_S \approx 6$ mm). The error bars have been calculated to indicate 95% confidence intervals using Eqn. 3.4, where μ, is the mean value of the avalanche sizes; σ, is their standard deviation; n, is the number of avalanches. The confidence interval is

$$\mu \pm 1.96\,\frac{\sigma}{\sqrt{n}}. \tag{3.4}$$

3.3.2 Arch shapes and properties

The non-monotonicity for the avalanche size needs more investigation, therefore the arch shape and some characterized properties will be described in this section. First of all, for determining the blockage arch we used the reliable definition introduced by Garcimartín *et al.* [18], where the 2D arch is the first layer above the orifice which blocks the outlet and restricts the outflow for the rest of the beads inside the silo. This arch consists of a set of self-sustained beads, if one of them would be removed, the rest would collapse. Since we have a horizontal silo base, the beads at the bottom which touch the silo base have a great stability. So we consider the first bead touching the left edge and the first one touching the right edge as bases of this arch and not part of it (*e.g.* the two solid circular blue beads in Fig. 3.4.(a). Sometimes the bases included more than one stable bead on each side). The arch was determined by starting from the first bead above the base on the left side of the orifice and moving through the orifice width D, marking all the beads in the first layer until reaching the first bead touching the base on the right side of the orifice. The arch beads are connected by the magenta curve (see Fig. 3.4.(a)).

After determining the arch, different characterizing parameters were defined to understand the arch properties.

- **Arch length (γ):** is the number of connected beads by the magenta-line in Fig. 3.4.(a) which block the outlet after excluding the bases. This parameter was checked for around 2000 arches with different shapes over twelve silo widths, illustrated in Fig. 3.4.(c). For this investigation, no significant dependence appears between the arch length and the silo width. The mean arch length fluctuated between 5 and 6 beads which agrees with ref. [18] at the same orifice size. The minimum value of the arch length appeared at the smallest width, $W_s \approx 6$ beads.

- **Arch aspect ratio (Q):** the second parameter describing the arch properties is the aspect ratio which gave us information about the arch shape. This parameter was calculated by dividing the half arch width (the half distance between the horizontal center positions of the farthest right bead and the farthest left bead in the arch represented by x in Fig. 3.4.(a)) by the arch height (the distance between the vertical center positions of the most vertically distant bead from the outlet to the closest one represented by y in Fig. 3.4.(a)). This means, if the arch aspect ratio Q =1, we have a semicircular arch, and if Q drops below one we will have a pointed arch, and if it rises above one, we will have nearly flat arch [18]. Within our experimental result, the mean aspect ratio of the registered arches is close to 2 for all widths (see Fig. 3.4.(d)). By compiling this result with the last one (the arch length), we can say that the formed arches almost took a convex shape and their widths reached nearly four times their heights for all the silo widths.

- **Angle between the beads (θ):** to understand the position of each bead in the arch in relation to its neighbors, the angle θ (illustrated in Fig. 3.4.(b)) was measured for each bead except the last bead in each arch side. Sometimes we have a flat angle (180^o) at which the three bead centers passed through the same line but this angle is not the maximum one. In some cases we found the central bead below this line and hanging upside down by the other two neighboring beads. In this case the arches were still stable because of the static friction [18]. The mean of the maximum angles has been calculated and plotted as a function of the silo width in Fig. 3.4.(e).

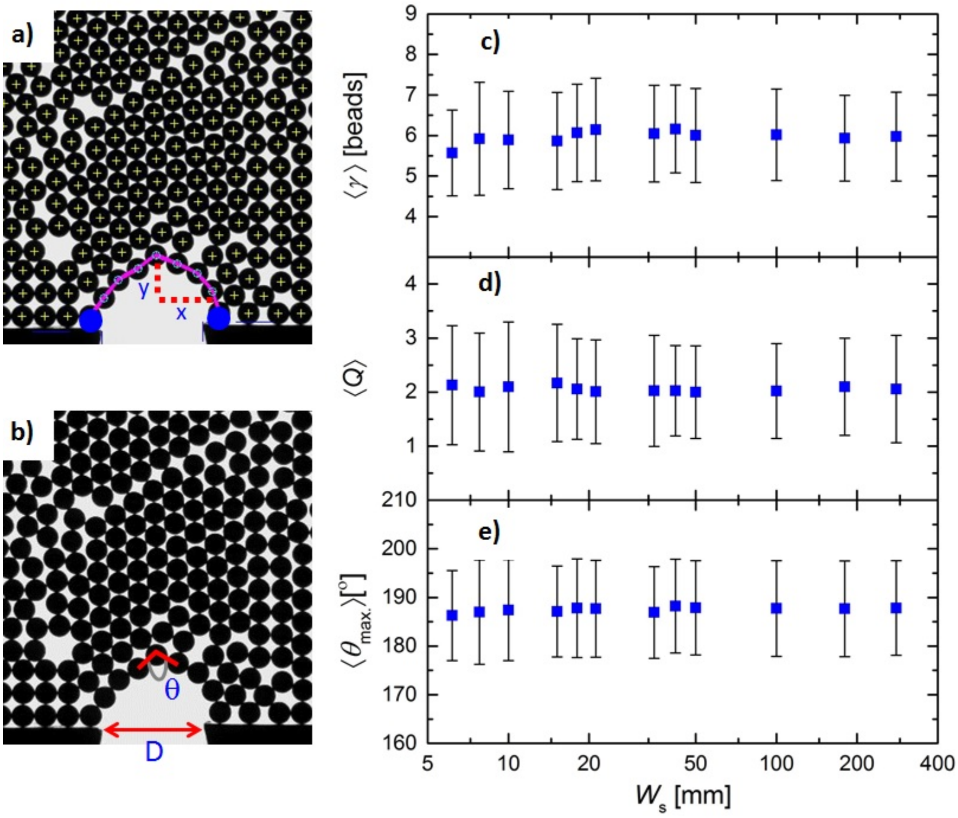

Figure 3.4: (a) The arch is presented by the magenta curve and its base by the two solid-blue circles. (b) The angle between each group of three beads θ in the arch is shown as red angle. (c) Arch length versus silo width. (d) Mean arch aspect ratio Q of the arch versus the silo width. (e) Maximum arch angle versus silo width.

The error bar of the last three parameters has been calculated as the standard deviation of the data.

In order to further investigate this phenomenon, the normalized PDFs were calculated for the arch length γ, the arch aspect ratio Q, and the maximum angle between the beads $\theta_{max.}$ respectively (see Fig. 3.5) for different silo widths. In Fig. 3.5 (a) and (c) the behaviour of the curves is close to the normal Gaussian distribution and the PDFs corresponding to the narrowest silo ($W_s = 6.1$ mm) show a small shift toward the left. In Fig. 3.5.(b), the probability density function for the arch aspect ratio Q possess an exponential tail. In that tail, few arches appeared with high aspect ratio.

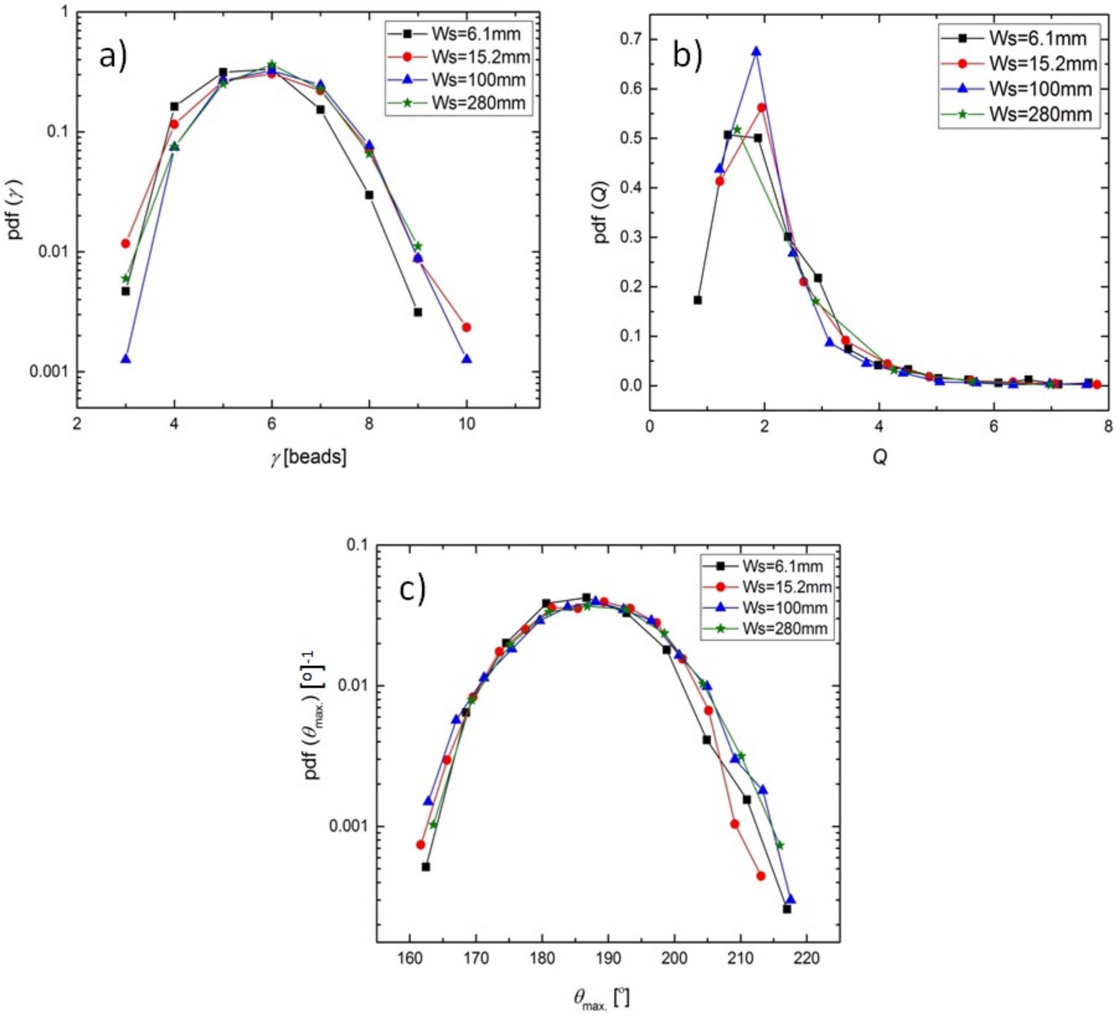

Figure 3.5: Normalized PDFs for: (a) the arch length, (b) The arch aspect ratio and (c) The maximum arch angle, at four different silo widths illustrated in the legend.

3.3.3 Mass flow rate at different silo widths

The mass flow rate was calculated by counting the beads when their centers passed the dashed line in Fig. 3.6.(a) and dividing them by the elapsed time for each video. In this part the camera speed was large enough to measure the elapsed time between two successively passing beads. The flow rate value associated with each silo width is presented by the average value for the 10 registered videos and the error bar is their standard deviation (see Fig. 3.6.(b)). In this figure we can see a saturation in the flow rate for the wide silos and this value increases by around 20% when we go to the narrowest one.

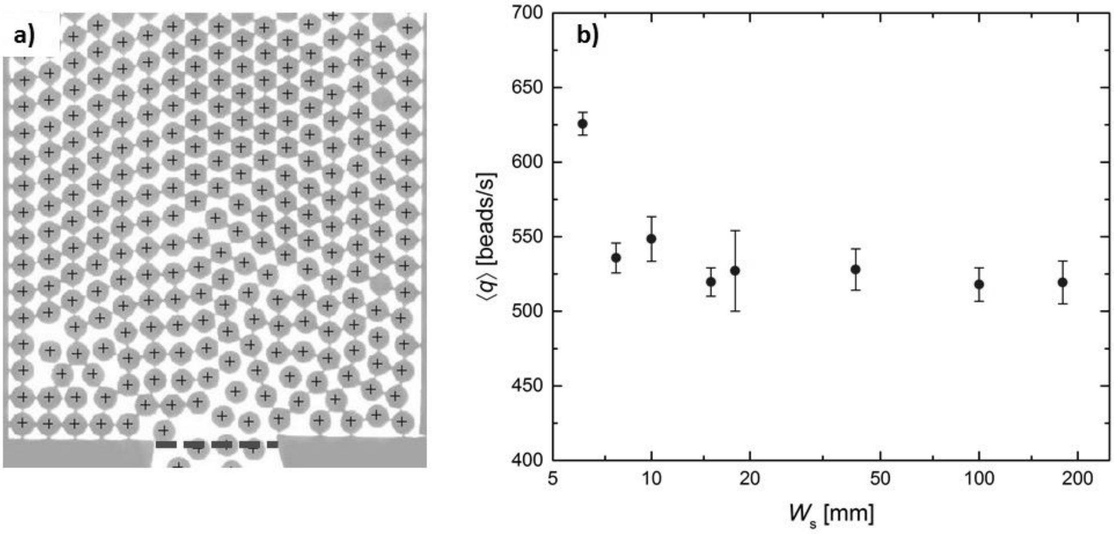

Figure 3.6: (a) One of the recorded video images during the outflow, the dashed line indicates the orifice and all the beads which passed this line were counted to calculate the flow rate. (b) The mean mass flow rate versus the silo width in x-logarithmic scale, similar to [46].

To understand the change in the behavior of the flow rate when the silo became narrow, the instantaneous flow rate q was measured in small temporal windows of 200 ms, which was time enough to allow a sufficient number of beads to discharge (see Fig. 3.7). It is interesting to note here, that when the silo width is between $W_s = 10$ mm and $W_s = 42$ mm (the values corresponding to the minimum avalanche sizes), downward peaks appeared with small values, which indicate intermittency in the flow (temporary stagnations) such peaks did not appear in the case of very narrow and of wide silos.

The normalized histogram of the flow rate at different silo widths is illustrated in Fig. 3.8. At the silo widths in which the minimum avalanche sizes occurred, there was a long tailing off in flow rates at the lower end of the scale. This confirmed the intermittency in Fig. 3.7. It did not appear for the other silo widths, where the distributions were close to Gaussian function. We can verify that there is a strong relation between the clogging and the flow rate intermittencies [63].

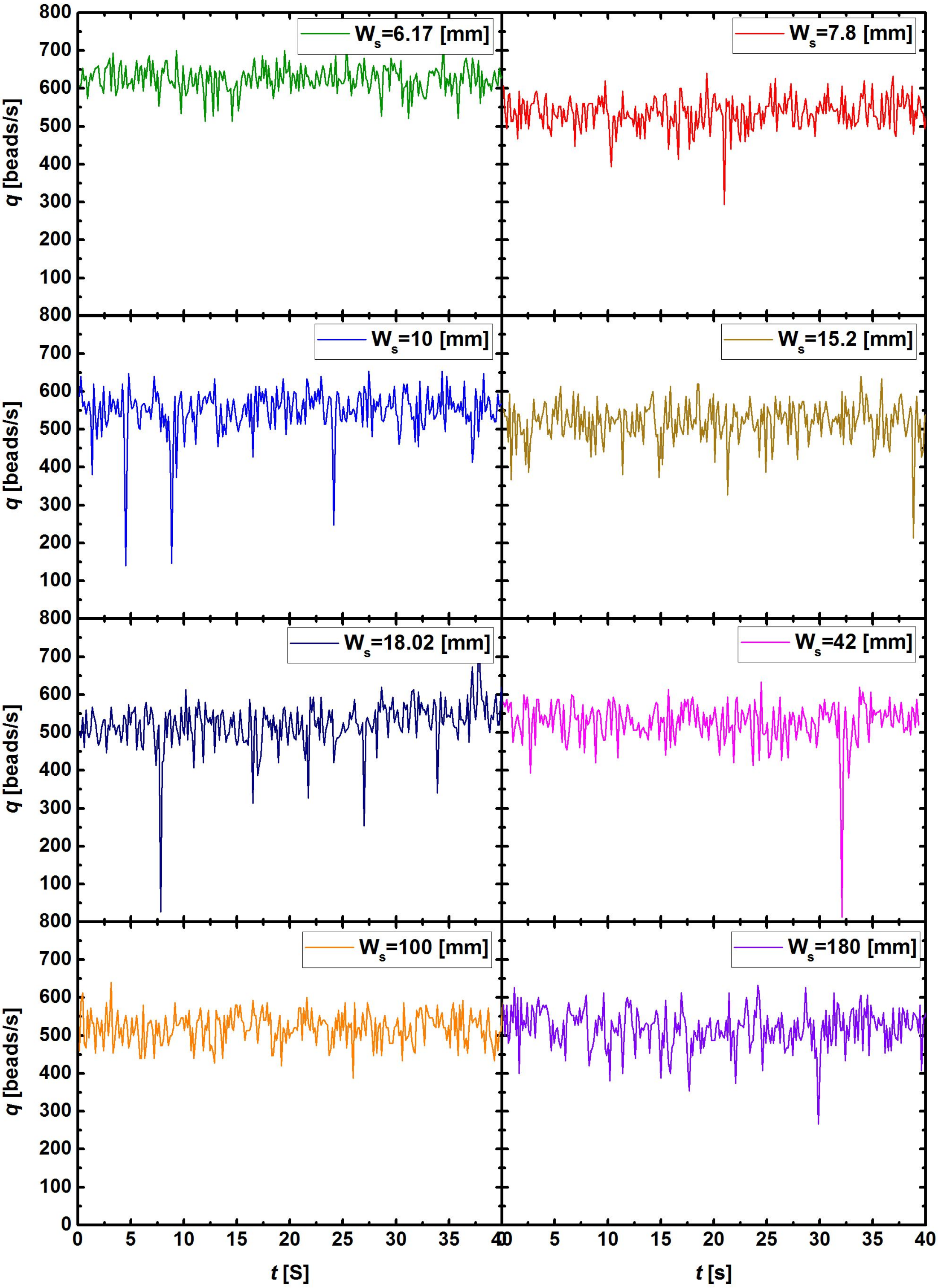

Figure 3.7: The flow rate q in 40 seconds over 10 registered videos at eight different silo widths. The values of q are obtained by counting the number of particles passing through the outlet in time windows of 200 ms.

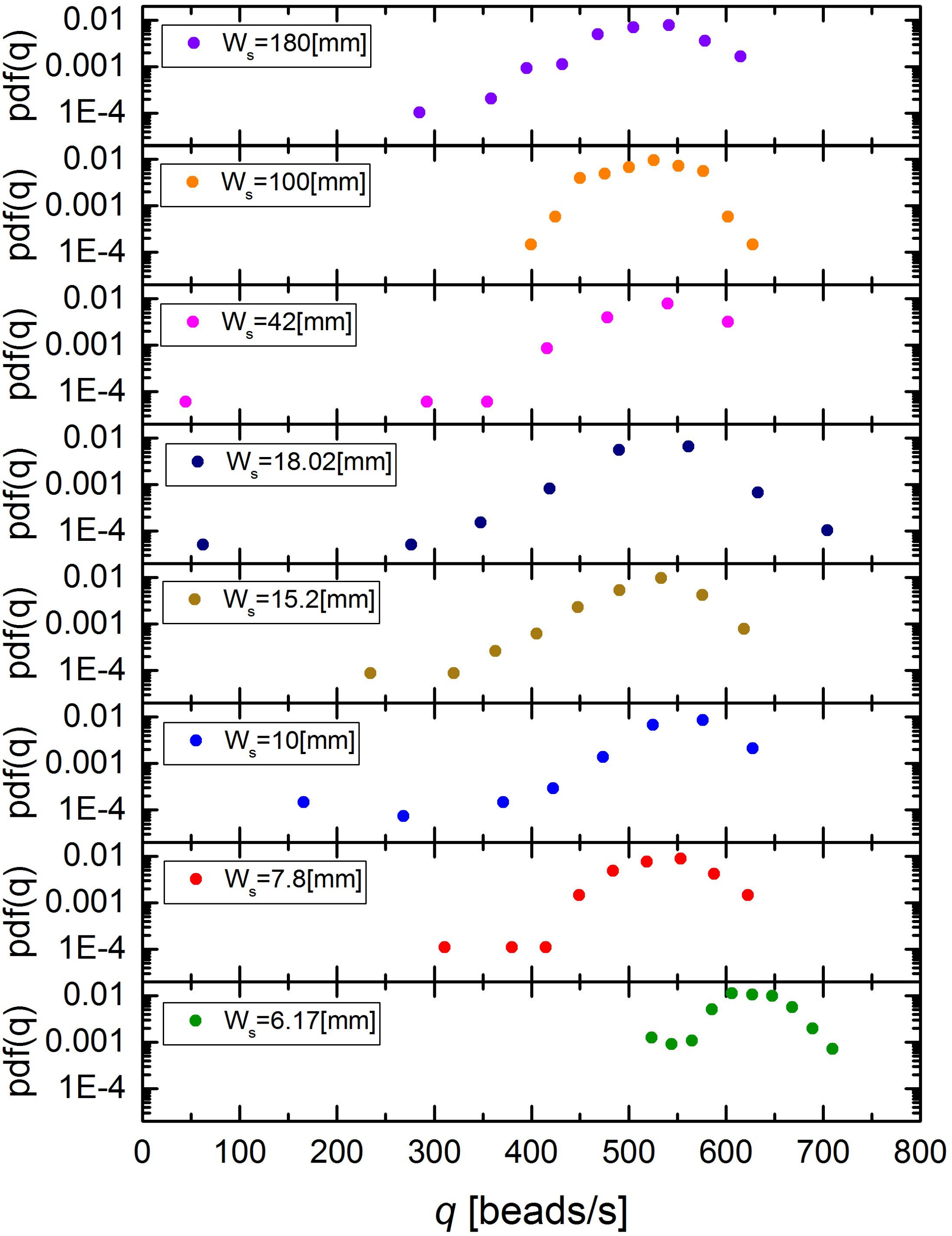

Figure 3.8: Normalized probability distribution function (PDF) of the instantaneous flow rates q for different silo widths as illustrated in the legend. The values of q are obtained by counting the number of particles passing through the outlet in time windows of 200 ms.

3.3.4 Packing fraction and velocity field

In this section, by knowing the particle positions and velocities, the experimental field maps of the packing fraction ϕ and vertical velocity v_y were plotted for six different silo widths (Fig. 3.9), applying an averaging coarse-graining technique [46]. By this we were able to characterize in detail the effect of the lateral walls position on the interior grains. In Fig. 3.9.(a) we can see the appearance of two triangles on the left and right sides of the outlet with high packing fraction (highly crystallized arrangement of the grains) in the wide silos. These regions gradually disappeared when the silo width W_s became narrower. Moreover, the packing fraction ϕ in the lateral sides next to the orifice tended to decrease also. This effect seems to be related to the change in the characteristics of a silo which is wide enough. Another effect developed significantly in Fig. 3.9.(b) related to the change in the silo width: when the lateral walls approached the outlet, an increase in the vertical velocity at the center of the silo appeared clearly above the outlet and the funnel flow shape inside the silo disappeared gradually.

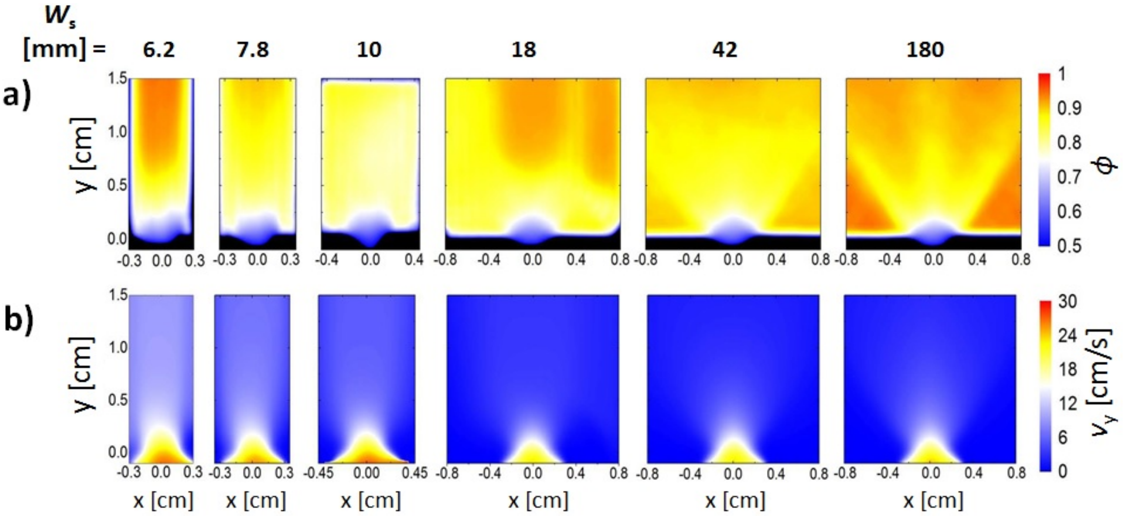

Figure 3.9: Field maps of (a) packing fraction ϕ, and (b) vertical velocity v_y for six different silo widths indicated above the images. Note that the color bar scale is the same in each series for comparison. Similar to [46].

For more detailed quantitative investigation of the lateral walls positions on the values of ϕ and v_y, the central packing fraction ϕ_c and central vertical velocity v_{yc} were plotted versus the relative height (y/d) from the silo bottom, illustrated in Fig. 3.10 (a) and (b) respectively. In these measurements, a thin vertical strip was chosen centered with the outlet at $x = 0$. The surprising point was that we could not extract a clear trend for ϕ_c related to clogging. On the other hand, the central vertical velocity v_{yc} shows a non-monotonic behavior when $(y/d > 3)$ synchronous with what appeared in Fig. 3.3. The vertical velocity was maximum for $W_s = 6$ mm and minimum for $W_s = 18$ mm at a certain height $y = 4$ mm from the silo bottom (see Fig. 3.3.(c)), this correlation might be related to the higher the kinetic energy of the particles when they form an arch [46].

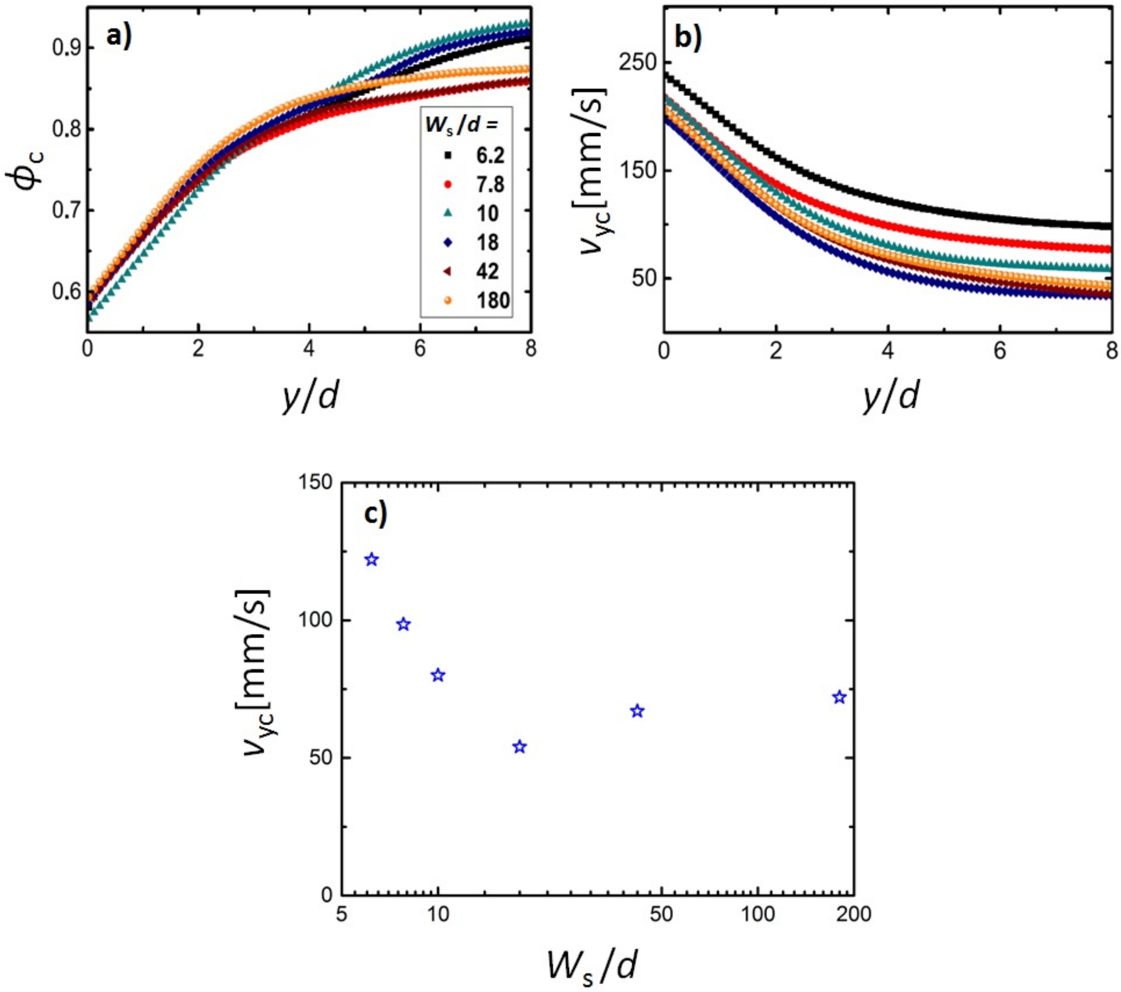

Figure 3.10: (a) Packing fraction ϕ_c, and (b) vertical velocity v_{yc}, for six different silo widths (labels are in the first panel) at the middle of the silo versus the relative height (y/d) from the outlet. (c) The vertical velocity v_{yc} at $y = 4$ mm from the silo bottom versus W_s/d. Similar to [46].

4 Characteristics of soft particles discharge in quasi-2D silo

In the last two chapters, we studied the outflow and clogging of hard particles in 2D and 3D silos. The friction and hardness play an important role in the stability of arches in 2D silos or domes in 3D silos when the orifice size is not much larger than the grain size. Moreover, not even the physical properties of hard granulates are completely understood today, even in the simplest form of monodisperse disks in 2D hoppers. In this chapter, we are going to study the effect of softness and almost total absence of friction on the flow and the clogging phenomena, which will give us new insights into the dynamic and static behavior inside the silo. A few academic studies have presented some features of soft grains. Bertho *et al.* [88] used dense air bubbles flowing in an inverse silo and Hong *et al.* [91] used oil droplets in water also in a reverse manner .

In this chapter, we chose an appropriate soft material that is loaded in the normal downwards silo. This material is called *Hydrogel spheres*, These hydrogels consist of three dimensional polymer networks [123]. When they absorb water they swell, and when they lose it they revert to their original sizes [124]. The time required for the swelling and shrinking processes depends on the environmental conditions.

To run our experiment, we bought monodisperse hydrogel spheres as solid particles with diameter $D \approx 2$ mm from *HappyStore, Nanjing*. After that we put them in distilled water for 24 hours to swell them until they reached the maximum size, with a diameter $D = 9.2 \pm 0.18$ mm and a mass $m_s = 0.42 \pm 0.03$ g (see Fig. 4.1). If we leave these hydrogels in the air for several hours they will dry out and shrink again. So we kept them in distilled water between the experiments to maintain a constant size during the experiments.

There are some properties which characterize this material in contrast to hard grains: first of all, they are incompressible but deformable spheres under the application of pressure. They return back to their original shapes when the applied force is removed; second, they have a very small friction coefficient. A value of $\mu = 0.03$ has been measured for the similar particles [125]; third, their Young's modulus is between 30 kPa and 50 kPa, where the outer part is softer than the inner part. This modulus is one of the most important parameters characterizing the soft particles. In our experiment we calculated it by putting the hydrogel spheres between two thin glass plates and applied a variable force on the upper plate. For each weight, we measured the corresponding Hertzian contact diameter.

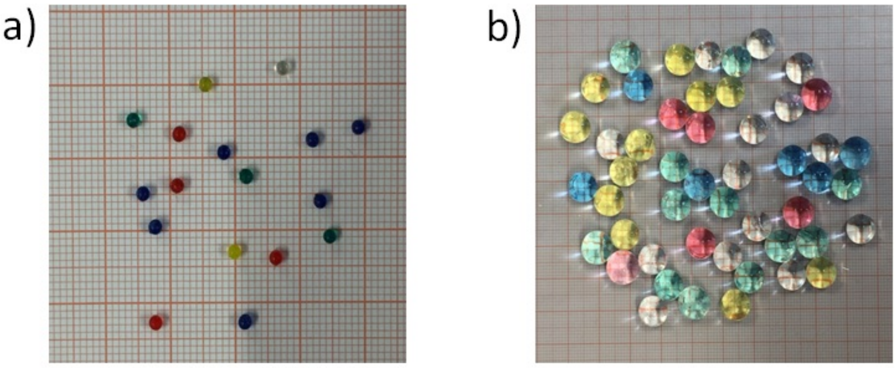

Figure 4.1: (a) Hydrogel spheres as a solid polymer with diameter $D \approx 2$ mm. (b) Photograph of the hydrogels after swelling in distilled water for 24 hours, with final diameter $D \approx 9.2$ mm.

4.1 Quasi 2D-silo experimental setup

The experiment was performed in a quasi-2D silo as illustrated in Fig. 4.2. This silo consisted of two thick glass plates each with 10 mm thickness and surface area 40 cm x 80 cm. These plates were positioned vertically on a stable metal bench. A reasonable gap (10 mm) was maintained between the plates. This gap was slightly larger than the diameter of the spheres, to minimize any friction between the hydrogels and the glass plates and prevent any sticking between them during the outflow. At the bottom of the silo, there were two metal strips which could be moved between the glass plates, to control the outlet size W. The ends of these strips, which enclosed the orifice, were cut at an angle 45^o downward to avoid any arch appearing between them. In addition, their edges were rounded smoothly to minimize the chance of the hydrogel spheres being damaged during the flow and the final inner dimensions of the silo become 77cm x 36.5 cm after extracting the strips. Beneath the orifice, there was a plastic container to collect the hydrogels during the outflow. The container was located above a digital electronic scale ($KERN_{KB}1000$) with resolution 0.05 g which means it can detect the mass of each individual sphere. This scale was connected with a computer. Before we loaded our silo with the hydrogels, we carefully removed any water between the spheres. The hydrogels were poured into the silo through a metal hopper above the silo. During the filling process, the sliding plate below the base of the holding bench was closed and prevented any sphere from running out. A high brightness LED white light sheet was used from behind to illuminate our silo, making apparent the contrast between the blue hydrogels and the background. Many different colors of hydrogel spheres were tested before selecting the blue one to be the most appropriate color to give us a significant contrast between the particles and the background during the outflow. A high-speed camera ″Phantom v611‶ with maximum resolution 1280 x 800 pixels was used for recording videos during the outflow of the hydrogels at different orifice sizes. The camera was located in front of the setup and focused on the surrounding area of the bottom centered orifice.

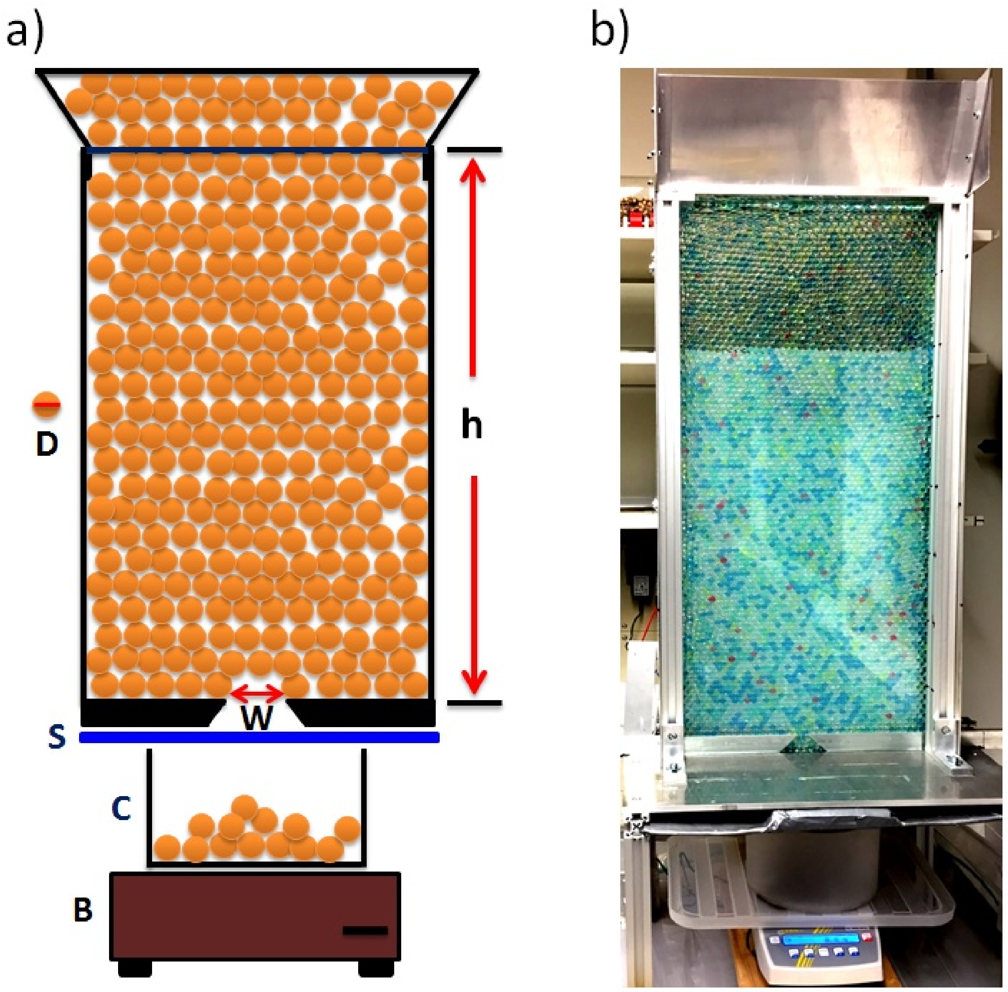

Figure 4.2: (a) Sketch of the quasi-2D experimental silo setup. W, orifice width; S, sliding plate; D, hydrogel diameter; h, filling height; C, collecting box; B, balance. (b) Photograph of a typical setup.

4.2 Experimental work and results

4.2.1 Orifice critical radius and filling height

At the beginning we filled our silo with the hydrogels through the upper hopper after closing the sliding plate. In our observation the hydrogels formed a nearly perfect hexagonal lattice which covered the whole silo when the orifice was closed and this lattice slid down gradually at the middle part of the silo from the top to the bottom during the outflow (see Fig. 4.3). The silo was filled with around 4700 hydrogel spheres, which means the volume packing fraction ϕ of the hydrogels is roughly 0.68. In fact, this value is greater than the normal value of hard spheres in a hexagonal lattice with $\phi = \pi/\sqrt{27}$. This is a result of the deformability in the hydrogels which are slightly squeezed into a rather hexagonal cross section.

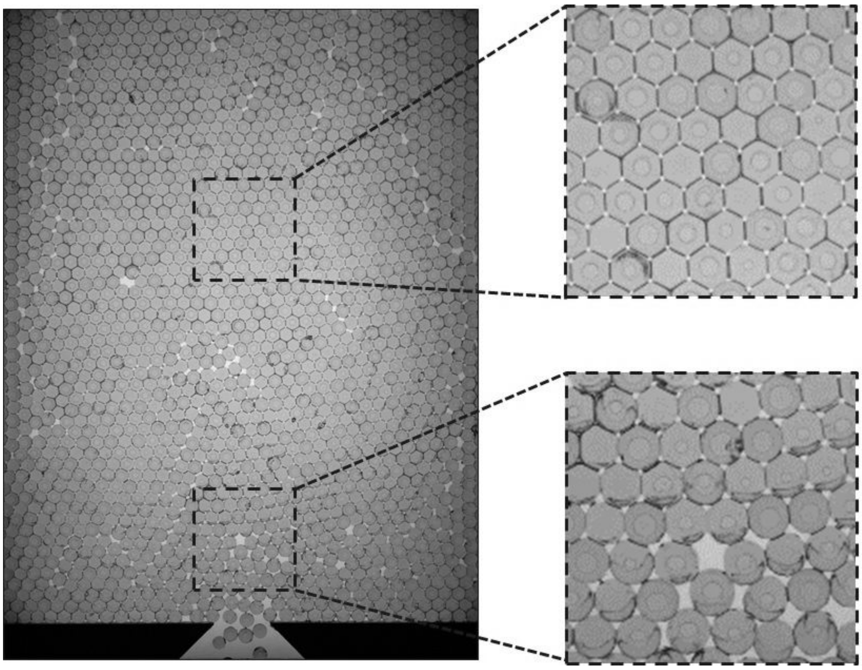

Figure 4.3: A photograph from the outflow video at ($W/D = 4.1$). The two dashed squares represent the hexagonal lattice form of the hydrogels, one directly above the orifice and the other far away from the silo bottom, both at the silo center. These regions are enlarged on the right side.

The features of the hydrogels play a role in the tendency of these spheres to block the outlet and arrest the outflow when the orifice is small. In the present work, some observations were noted for the hydrogels which were completely different from those of hard grains. The first observation was, the silo was completely emptied of spheres when the relative orifice size was $W/D \gtrsim 2.2$, without producing any clogs during the discharge. This behavior is completely different from the literature results found for hard spheres, where one can find clogging even if W/D is as large as 5 [10, 58, 75]. The second observation was, when the relative orifice size W/D became less than 2.1, obvious fluctuations in the velocity field appeared. They clearly are related to small clogging events for few seconds, which are resolved by themselves, and are followed by a permanent clogging state only when the container fill level becomes smaller than a certain height h_f. In Fig. 4.4, the number of outflown particles is plotted as a function of time. Seven different orifice sizes are presented, two of them for the relatively large orifices with $W/D \gtrsim 2.2$, their discharged curves resemble straight lines without any indication of intermittency in the flow. The opposite occurred in the rest of the orifices with (W/D) less than 2.1. Here an intermittency in the flow was observed and it increased with decreasing relative orifice size. The temporary clogging events represented in this graph by the short horizontal lines and their widths indicate the short elapsed clogging times before they were resolved by themselves. At the end of each curve one can see the long horizontal line which indicates the final clogged state at a certain filling height.

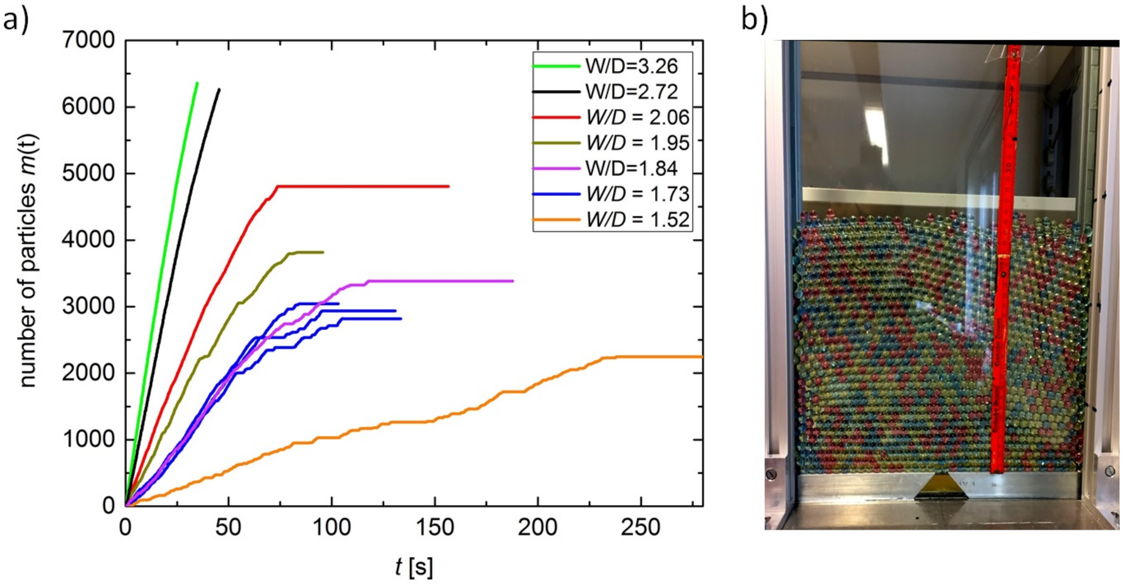

Figure 4.4: (a) Intermittent clogging when the orifice width is $W < 2.1\ D$, followed by a permanent clogging state at a certain height, represented by the long horizontal lines. (b) Photograph of one of the final permanent clogging states at an orifice with relative size $W/D = 1.84$.

The data in the $m(t)$ curves were obtained experimentally by using an electronic scale connected directly with the computer and controlled by a LabVIEW program. This program registered the measured mass of the discharged spheres every 0.1 sec with high enough resolution to discriminate each individual hydrogel sphere. Many experiments were performed corresponding to each orifice size, and the remaining filling height h_f for each experiment was measured, relative to the silo bottom. The different remaining fill levels of the five small orifices with $W/D < 2.1$ in Fig. 4.4 are illustrated in Fig. 4.5 versus W/D. Within this data, the final filling height corresponding to each orifice size varied by around ± 30 % from its average value. This height decreased with increasing orifice size. An acceptable linear fit led to Eqn. 4.1 and Eqn. 4.2 using the left and right scales of Fig. 4.5 respectively, where h_f is the critical remaining filling height of the hydrogels inside the silo after they reached the final clogged state, and p_f is their critical pressure at the silo bottom:

$$h_f = (2.2 - W/D) \text{ x } 95 \text{ cm} \tag{4.1}$$

$$p_f = (2.2 - W/D) \text{ x } 6.6 \text{ kPa} \tag{4.2}$$

In the following section, the determination of this pressure is described. From this fit, we deduced a strong correlation between the remaining filling height of the hydrogels inside the silo and the orifice size, which is one of the mysteries of the behavior of the soft particles inside the silo.

The clogging probability $n(h)$ of 26 independent experiments at the orifice size ($W = 1.84\ D$) as a function of the fill level is presented in the inset of Fig. 4.5 as an example. The probability data was fitted by

$$n(h) = 0.5 + 0.5\ \tanh[(h - 29\text{cm})/5.7\text{cm}], \tag{4.3}$$

where at 29 cm filling height the system was clogged by 50% with a standard deviation 5 cm. For hard grains, the clogging behavior is practically independent of the silo fill height unless rat-holes are formed. This guided us towards studying another important effect.

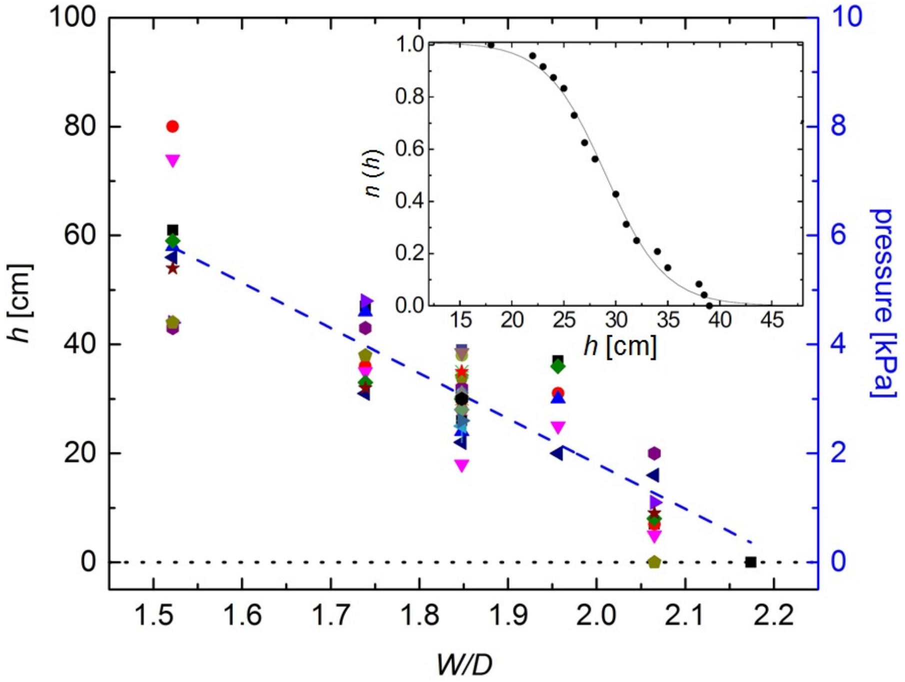

Figure 4.5: The remaining fill height of hydrogels when the silo outflow clogs permanently on the left scale, and its pressure on the right scale for five different orifice sizes with $W/D < 2.1$ as illustrated in Fig. 4.4. The different symbols correspond to different runs of the experiment. The data go well with the linear fitting represented by the dashed line. The inset figure shows the clogging probability $n(h)$ for different remaining fill heights at the orifice size $W/D = 1.84$ follow with a hyperbolic black guide line.

4.2.2 Effect of the filling height on the bottom pressure

Changing the filling heights with the orifice sizes in the last section led us to check the static pressure when we loaded our silo with the hydrogel spheres. For that, the silo was modified by putting a small metal plate with an area 6 cm x 1 cm in the middle bottom of the silo. This plate is connected to a scale by a metal holder and it works as a pressure sensor by measuring the weight of the spheres acting on it (see Fig. 4.6).

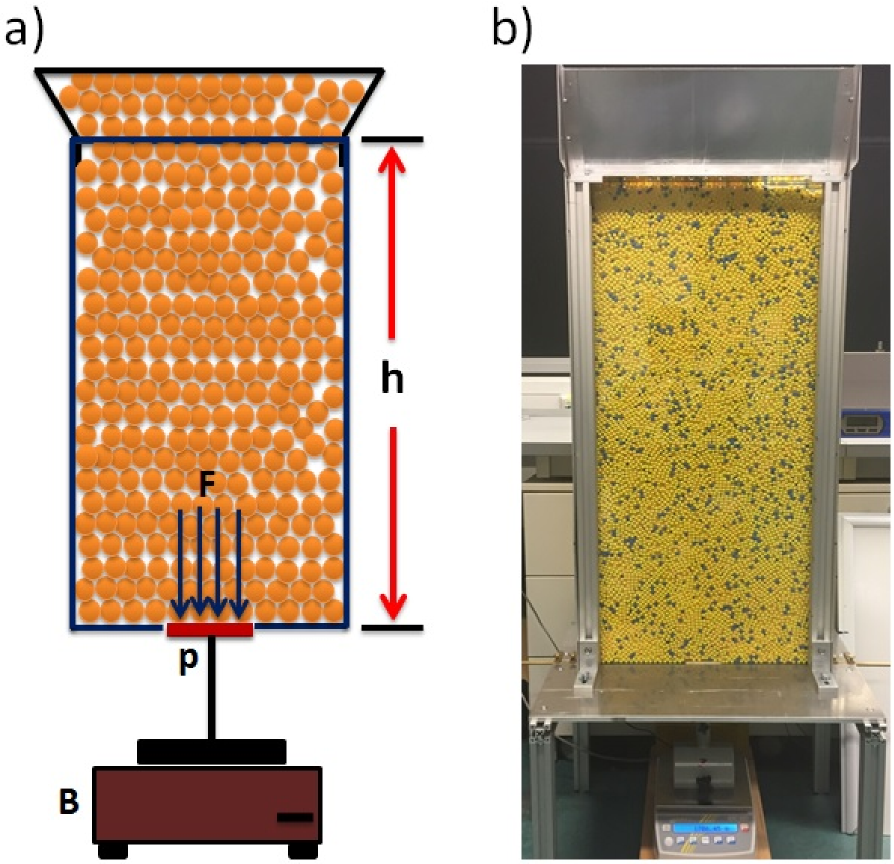

Figure 4.6: (a) Sketch for the modified quasi-2D experimental silo setup for measuring Janssen's effect on the hard and soft materials. B, balance; p, metal plate connected directly with the balance; F, the weight force of the inside spheres; h, the filling height. (b) Photograph of the real setup loaded with airsoft balls.

The position of the pressure sensor can be changed by moving it over the silo bottom. At the beginning, the silo was empty and the scale measurement was calibrated to zero. After that, we poured a certain amount of the hydrogels, measured their filling height, waited for 5 seconds and finally recorded their corresponding force onto the plate. These steps were repeated until the grains covered the whole silo. The experiment was executed several times and for each one around 10 different heights with their corresponding weights were recorded. From our experimental data, it can be seen that the pressure increases linearly with the filling height without any noticeable saturation, and this is in contrast to Janssen's effect for hard frictional particles [106], where after a certain filling height the pressure saturates and the particles weight is transferred to the side walls through force chains [107]. In Fig. 4.7, we illustrate the pressure versus the filling height. The solid circular symbols are the experimental data when the pressure sensor was at the middle of the silo bottom, and the open circular symbols represent the results when this plate was moved nearly to the side wall at the silo bottom. In the last position, the pressure values measured by the sensor were slightly smaller than when it was in the center. The average pressure of the hydrogels at the bottom of the silo was close to 68% of the pressure when the silo was filled with water, where the hydrogels' density ρ_h is around 1.03 g/cm^3 and this value strongly relates to the packing fraction ϕ of the hydrogel spheres.

The pressure of the hydrogels can be estimated at any height within our silo dimensions by using Eqn. 4.4 . One important note is that this pressure drops by about 50% during the discharge. For comparison, two different hard materials were used, smooth airsoft balls with density 1.05 g/cm^3 and peas (higher friction coefficient $\mu = 0.35$ than the others) with density 1.35 g/cm^3. In both experiments for the hard grains, the saturation in the pressure after linearly increasing up to a certain filling height is seen clearly in Fig. 4.7.

$$p(h) = h\rho_h g\phi = 6.9 \text{ kN/m}^3 \tag{4.4}$$

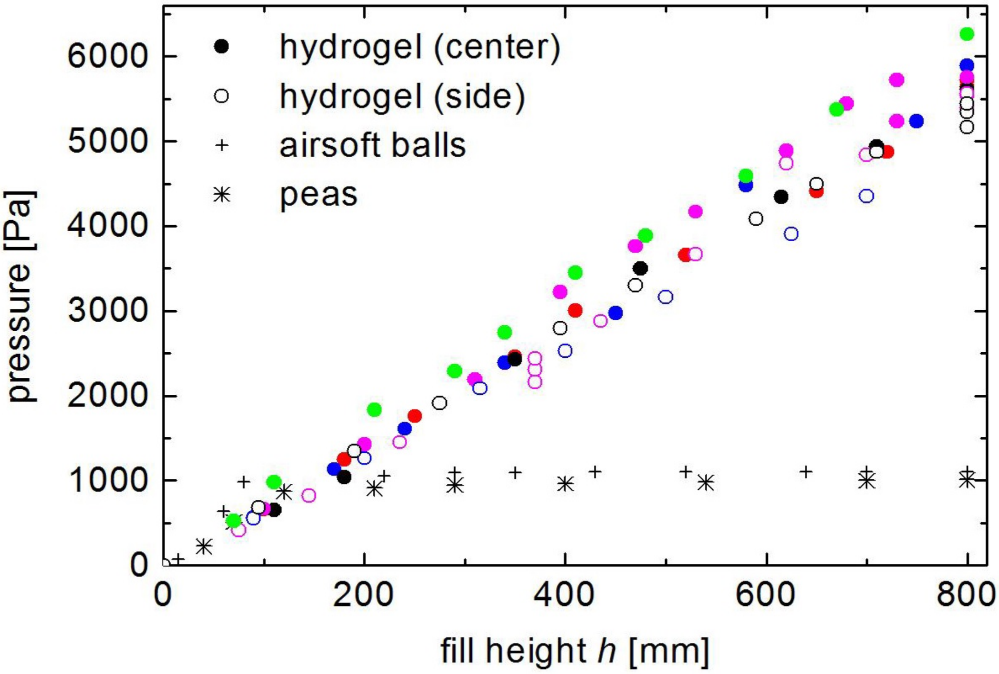

Figure 4.7: Static pressure acting on the plate at the bottom of the silo versus the fill height. Solid symbols, the plate in the center of the bottom; open symbols, the plate near the side of the bottom. Different colors represent different experimental runs (the experimental error is smaller than the symbol sizes). The same experiment was repeated for hard grains, peas with diameter 7.6 mm and airsoft balls with diameter 6 mm for comparison.

4.3 Hydrogels flow fields

In this section, a high speed camera ″Phantom v611‶ was used for recording fast videos with high enough speed (1000 frames per second) for the hydrogels during the discharge. Nine different orifice sizes were adjusted, and for each one many different videos were registered with a total length of 50 seconds each, without any interruption in the flow. The registered videos focused on the surrounding area of the outlet with dimensions 23 cm x 34 cm, where the orifice was centered at the bottom.

The hydrogels were detected and tracked as described before in sections 3.2.1 and 3.2.2, respectively. The velocity maps of three different orifice sizes are illustrated in Fig. 4.8. As seen from these maps, the hydrogel spheres show a new behavior during the discharge which is completely different from the behavior of the hard particles studied before [45]. In Fig. 4.8.(a) we can see the horizontal tendency of the spheres to go toward the orifice from the right and the left even at the silo bottom. This tendency appears clearly at the bottom. It increased with the orifice size. In hard grains discharge, the outflow profile is funnel-shaped, with triangular stagnant zones at the bottom, on both sides of the orifice. This funnel is degraded in the investigated low friction particle discharge. This is in agreement with the low friction coefficient of below 0.03 reported for hydrogel spheres. By looking at the vertical velocity field maps in Fig. 4.8.(b), a small funnel flow appears above the orifice and its height and width increase with the orifice size. After a certain height depending on the orifice size, the small funnel flow shape completely disappeared and the remaining amount of the hydrogels above it move with a constant plug flow velocity as a result of the formed hexagonal lattice. Moreover the zones, on the side of the orifice were moving but with lower velocity.

In order to check the fluctuation of the vertical velocity during the discharge, a thin vertical strip at the middle of the silo was taken from the video frames. In this strip, the average vertical velocity was measured in time windows of 100 ms for the total length of the registered videos (50 sec.). The velocity map of this strip is presented in Fig. 4.8.(c). Within the chosen time windows, we could not see a clear indication for the fluctuation in the vertical velocity during the discharge (the values of the velocity are nearly the same along any horizontal line), which shows the smooth outflow of the hydrogel spheres.

The change in the funnel flow shape until reaching the level at which the spheres move with a plug velocity. This is presented in Fig. 4.9 by plotting the vertical velocity profile at different heights. From the plotted profiles, the vertical velocity decreases gradually with the height and the funnel flow becomes wider until a certain height $y \approx 2.5\ W$, where the motion is plug-flow like. After that, the flow becomes flat through the silo. The idea of the plug flow after a certain height is related to the hexagonal lattice, which was formed by the soft hydrogels inside the silo. In this respect, the outflow is completely different from the behavior of hard spheres.

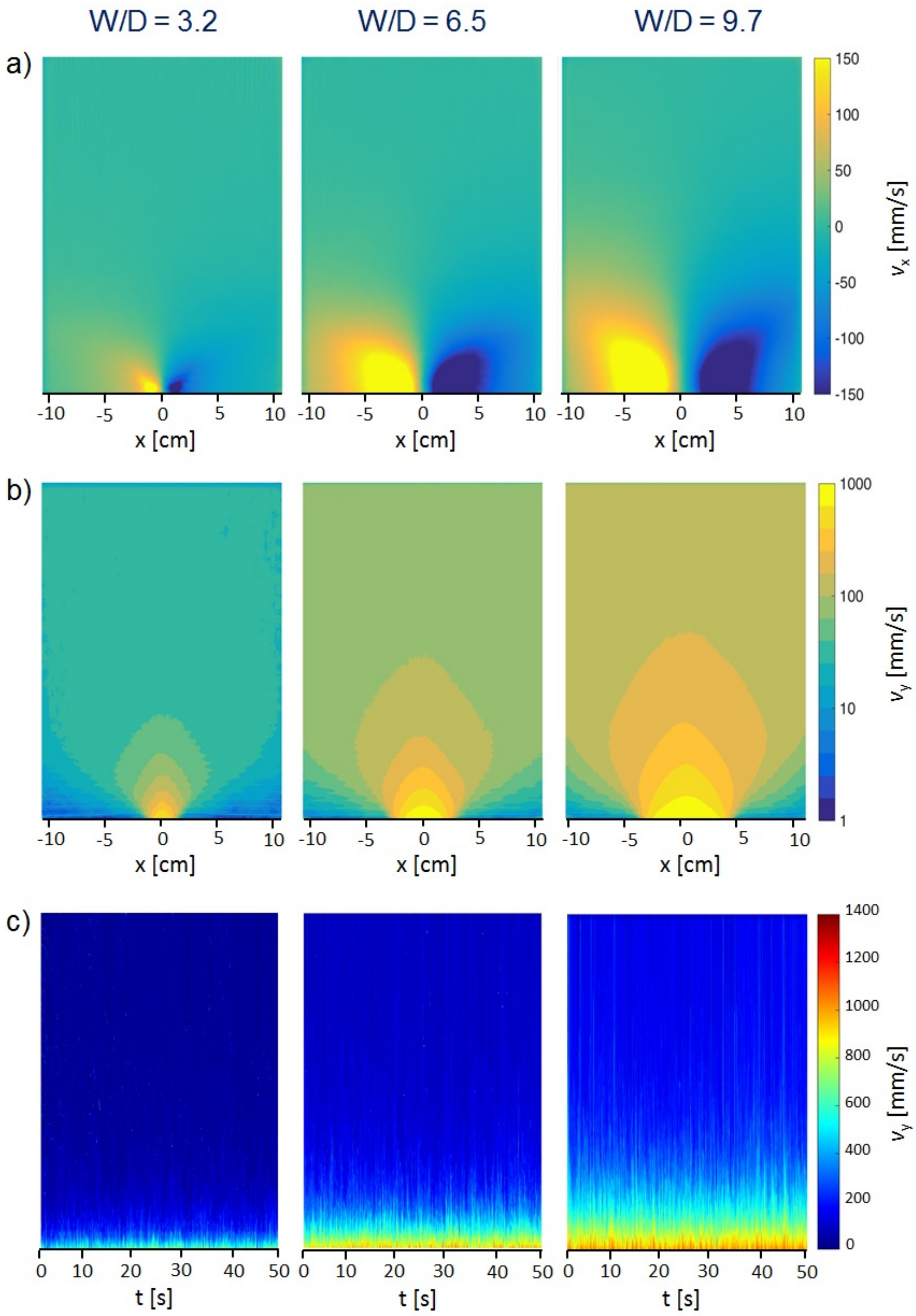

Figure 4.8: (a) Horizontal velocity v_x field maps. The yellow regions indicate flow to the right, the blue regions to the left and the green indicate zero horizontal flow. b) Vertical velocity v_y field maps. (c) The fluctuation of the vertical velocity v_y in a thin strip at the center of the silo in time windows of 100 ms. (a), (b) and (c) represent three different orifice sizes indicated at the top, for each sub-figure the colorbar is the same and can be seen on the right side.

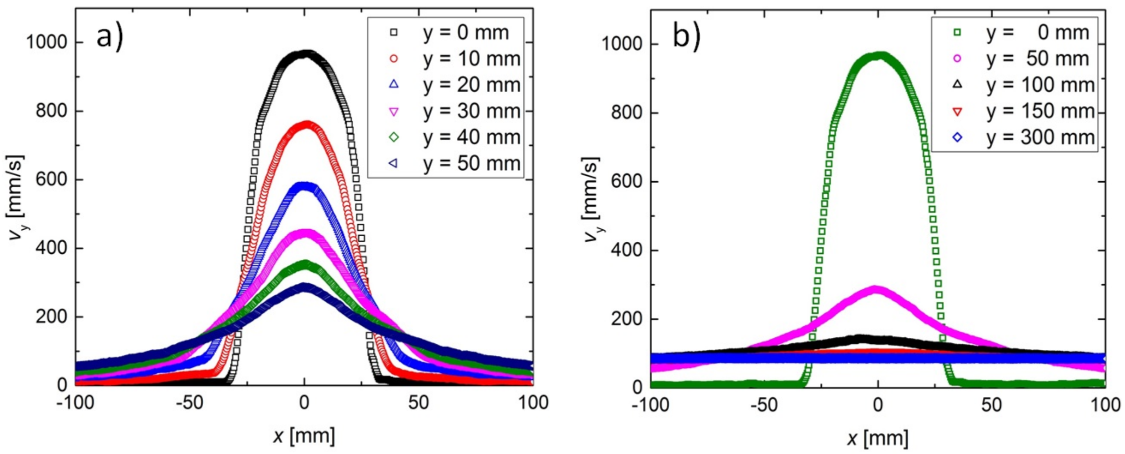

Figure 4.9: Vertical velocity profiles at different heights y as represented in the legends for the orifice size $W/D = 6.5$, (a) from $y = 0$ mm to $y = 50$ mm with small height steps (10 mm); (b) from $y = 0$ mm to $y = 300$ mm with large height steps.

The vertical velocity profiles of nine different orifice sizes are illustrated in Fig. 4.10. Subfigure (b) shows the velocity profiles at the orifice line, where there is a significant increase in the maximum velocity at the center of the orifice (the profile peak) for the small orifice sizes. For the large orifice sizes this difference becomes relatively small compared to the smallest orifice sizes (the peaks seem to be collapsed on each other).

The coincidence in the peaks is related to the competition of the hydrogels from the right and the left sides of the orifice to go through the outlet which leads to a decrease in the maximum velocity at the center of the outlet and makes the peaks wider. If we go 10 cm upwards inside the silo as in Fig. 4.10.(c), a short funnel flow shape is present for the largest orifice size and when the orifice size decreases it becomes increasingly shallow, culminating in a roughly flat shape at ($W/D = 2.1$). By going further inside the silo, at the height of 25 cm from the silo bottom (Fig. 4.10.(d)), the velocity profiles seem to be flat along the investigated silo width (all beads move with almost the same velocity) for the different orifice sizes. An exception is the widest one ($W/D = 10.7$), where its profile takes a small curvature upward.

From the last observations, we can say that the plug-flow of the hydrogels depends on the orifice size (when the orifice size is small the plug-flow appears at short height from the silo bottom).

The last conclusion can be demonstrated by calculating the average vertical velocity along the recorded silo width (part of the real width of the silo) as a function of the height (see Fig. 4.10.(e)). The horizontal tails of the curves which indicated plug-flow appear at a lower height for the smallest orifice and this height gradually increases with the orifice size.

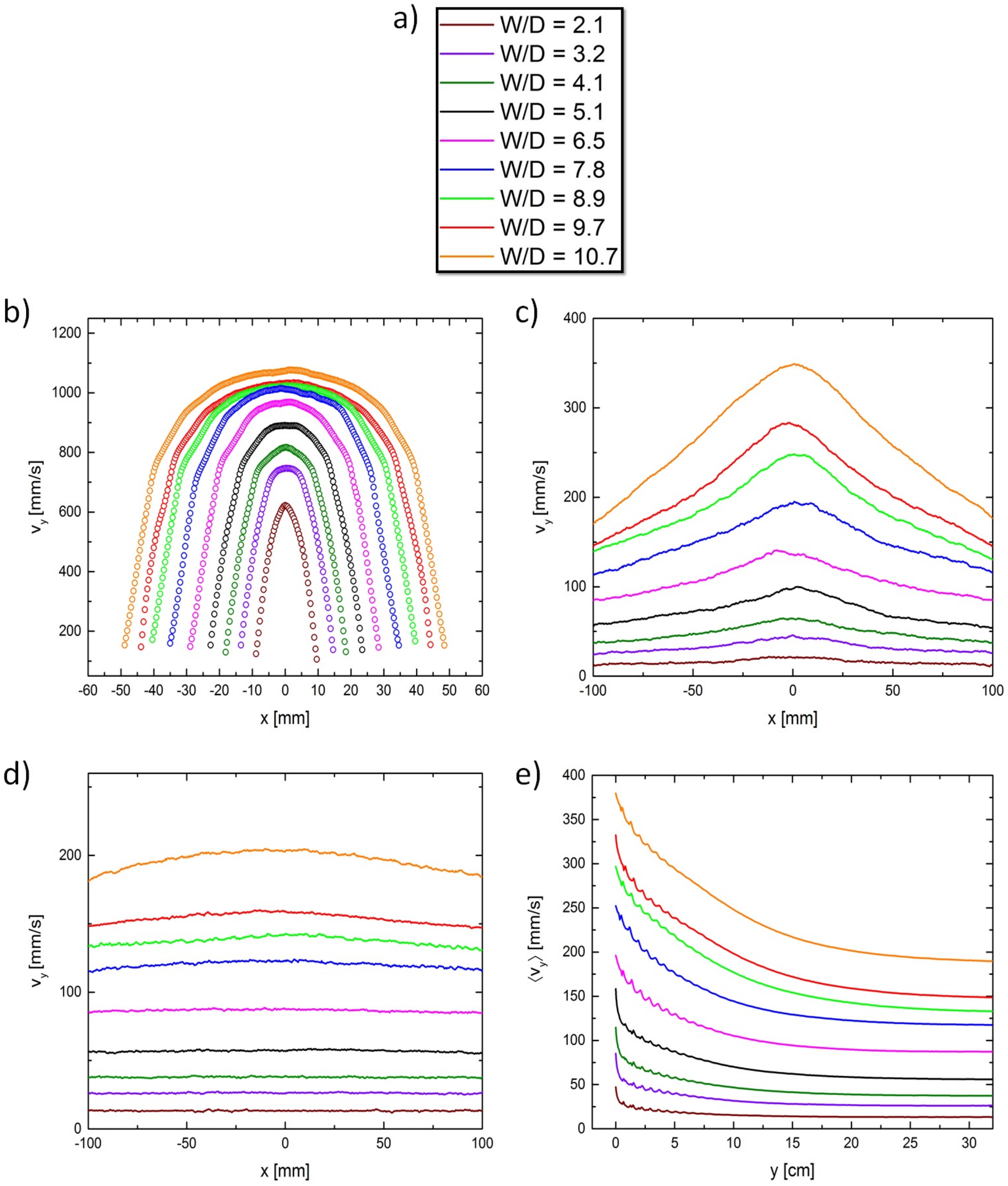

Figure 4.10: (a) Color legend for nine different orifice sizes. (b) Vertical velocity profiles at the orifice line ($y = 0$ cm). (c) Vertical velocity profiles at height ($y = 10$ cm). (d) Vertical velocity profiles at height ($y = 25$ cm). (e) The average vertical velocity along the recorded silo width (around 50% of the real silo width) as a function of the height inside the silo.
]

4.4 Mass flow rate of the hydrogel spheres

The mass flow rate q of the hydrogels was measured by using the balance below the silo which has sufficient accuracy to detect one single sphere. The mass of the discharged spheres and the elapsed time were registered on the computer using a LabVIEW program. The experiment was repeated for different orifice sizes and for each orifice many runs were performed. The discharged mass and the elapsed time were registered after 2 sec. from starting the outflow and ended at the point when the silo still copmletely filled with the hydrogels to ensure we had a constant flow. The mass discharge was measured at the orifice size $W/D > 2$ to avoid the intermittency in the flow as a result of the unstable clogging events, which can last for a few seconds and which dissolve by themselves. So the mass flow rate could not be measured for the very small orifices. The mass flow rate q versus W/D for the hydrogel spheres is illustrated in Fig. 4.11 and for comparison, data of hard airsoft balls are added to the graph. The surprising aspect was, that Beverloo's equation

$$q = q_o \left(W/D - k\right)^{\frac{3}{2}} \tag{4.5}$$

is still valid to fit the flow rate data of the soft spheres as well as the hard grains with $q_o = 37$ spheres/s and $k = 0.3$. The value of k in the case of the soft particles is very small compared to the hard grains with $k = 1.52$ which makes the flow rate through the small orifices more effective. From our results, we can say that softness and friction play an important role in making the flow rate of the hydrogels higher than the hard grains at the same orifice sizes.

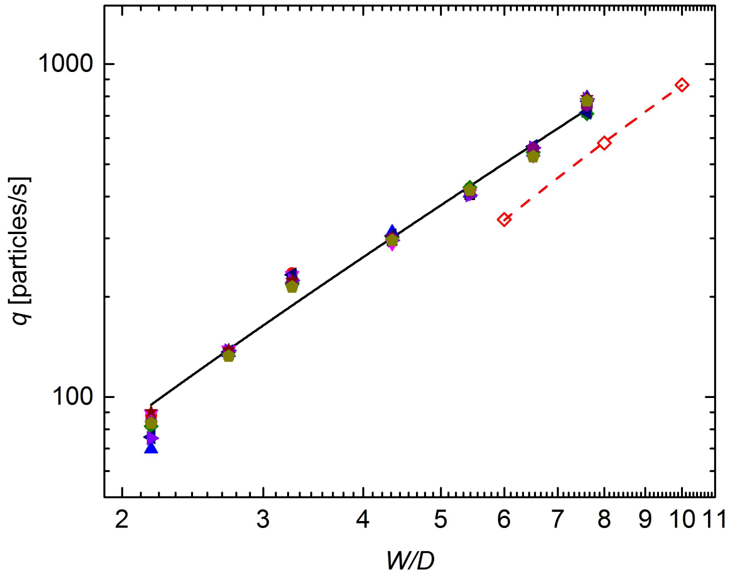

Figure 4.11: The flow rate q versus W/D for soft hydrogel spheres and hard airsoft balls. In this comparison, the behavior of both materials can be fitted using Eqn. 4.5, but the hydrogels show a significantly higher flow rate at the same given relative orifice sizes.

5 Summary

The area of research presented in this dissertation on silo discharge experiments, has attracted a great deal of interest from researchers into granular matter. But it is also important because of its occurrence in everyday life and its potential significance for several fields of industry. I investigated the statistics of discharge phenomena for different types of materials, focusing on shape-anisotropic grains and clogging events when the granulate flows out from silos with small apertures compared to the size of the grains. In my experimental work I used three different classes of granular materials (*e.g.* isotropic hard grains, anisotropic hard grains and soft spheres) to understand how the aspect ratio and the softness influence the discharge dynamics and the clogging probability. In order to execute my work, I built and modified three different silo experiments, each of them based on a specific idea and illustrated in detail in a separate chapter. What follows is a summary of the main results which were obtained during my PhD study as presented in the previous chapters.

In chapter 2, I described the construction of a cylindrical 3D experimental silo with a flat bottom base, in the middle of which I can insert and replace different plates with different circular orifice sizes. The aim of this part of the thesis is to study the dynamics and statics phenomena for anisotropic grains during the discharge from a silo with a small outlet. The silo was loaded with anisotropic materials with a broad range of aspect ratios, shapes and types. In addition, we added measurements of spherical particles for comparison.

The statics and the dynamics of the elongated grains through the silo are qualitatively different from those of spherical grains. One of the new phenomena which appeared during the study of the elongated grains was that when we freshly filled our silo with elongated grains they were highly disordered at the beginning and the first avalanches were very small compared to the following ones. The air blower successively empties the cavity above the orifice from disordered particles and gives the chance to the following grains to align toward the center in the shear flow. This phenomenon is in contrast to the behavior of the spherical particles where there is homogeneity in the distribution of the avalanches from the first to the last one. To achieve statistically significant results for the elongated particles we had to discard the first avalanches.

For all the experimental data which I presented for the 3D silo, the distribution for thousands of avalanches at different orifice sizes was checked, and exponential decay of the size distribution was relieved which means we have a constant clogging probability for each particle passing the outlet. The clogging probability for the elongated as well the spherical particles decreased with increasing orifice size and we could not distinguish between the power law model (Eqn. 1.1) and the exponential model (Eqn. 1.2). The reasons are limitations governing my experimental work (*e.g.* silo dimensions and the amount of available materials (up to 10^6 grains) and their weight). An important aspect was the extension of known empirical characteristics for spheres to anisotropic grains.

At the start, I rescaled the orifice radius by dividing by the equivalent particle radius (the radius of the sphere which has the same volume as the tested grain) and this was the first approximation to compare between the elongated and the spherical particles. It was observed that the clogging probability increased with increasing aspect ratio at a given relative orifice size. The used fit equation worked only for fitting the data of grains with an aspect ratio < 6. For plastic rods with aspect ratios 6 and 8 it was found to fit the small orifice size part until the relative orifice size ≈ 5. After that, I found it more reasonable to compare the anisotropic grains with spheres which have the same cross section area (*i.e.* similar geometric averages of length and diameter) instead of the same volume. In that case all the curves of the studied grains can be combined to one master curve, but there is still a discrepancy in the behavior of the grains with large aspect ratios above 6 for large orifices.

The increase in the clogging probability was greater than expected at the large orifice sizes for elongated grains with aspect ratios 6 and 8, this led us to study an even more elongated particle shape with a higher aspect ratio ($Q = 12$). It was surprising to note that at the beginning there were only a few avalanches and after that, our air blower was useless. On checking the silo, we found that a long empty tunnel had formed above the orifice penetrating the entire granular bed until it reached the end of the silo. Going back to the rods with $Q = 6$ *and* 8, an empty tunnel was found above the orifice as well but was shorter than for the $Q = 12$ grains at the large orifice sizes. This is obviously the reason for a decreasing mean avalanche size at these orifice sizes. The appearance of the rat-hole needs further investigation because the dimensions of the silo could be relevant for the phenomena described in this thesis.

The aspect ratio of the elongated particles not only affected the clogging probability but also mass discharge. The flow rate was decreased by increasing the aspect ratio at given orifice sizes and we could not find a significant difference in the flow rate between the ellipsoid rice grains and the cylindrical glass rods which have the same aspect ratio. The long-established Beverloo's equation fits the anisotropic discharge data until aspect ratio 6, but for the plastic rods with $Q = 8$ it no longer works. A strong correlation appears clear between the dimensionless constant k in Eqn. 2.12 and the aspect ratio Q, where it increases regularly with the aspect ratio. So now we can say that the long axis is more effective than the two short axes in Beverloo's equation when we use elongated particles and this is the reason why it could not fit the grains with the aspect ratio 8.

In chapter 3, I introduced a new parameter which would play an important role in changing the clogging probability and the flow field inside the silo. The 3D silo is a complicated setup if we want to study a new phenomenon and needs a special imaging technique to understand the behavior of the grains inside the silo. For that reason we established a 2D silo with movable side walls to study the effect of the lateral wall positions on the clogging probability. The silo was loaded with monodisperse stainless steel spheres with diameter of 1 mm and the thickness of the silo was adjusted to equal the diameter of the beads. It was tested to ensure there were no grains stuck between the glass plates during the outflow. A fixed orifice width (≈ 4 beads in diameter) was chosen to be suitable for our target and enabled us to register thousands of avalanches at different silo widths and to record the outflow videos without any interruptions.

The variation to the silo width resulted in a significant change in the clogging probability especially for narrow silos. It was noted that the clogging probability increases with the silo width until a certain width, after which it starts to decrease again and reaches saturation at larger widths. The clogging probability for the widest silo is much larger than for the narrowest silo, which has only one bead on the right and left of the orifice. This new phenomenon led us to investigate and study other properties which could be related to the silo width and explain the observed non-monotonic behavior.

First we illuminated our silo by using LED white light from behind, and by using a CCD camera placed in front of the silo and focused on the area surrounding the orifice. An image corresponding to each clogging event was registered. From the recorded images the beads which belong to the arch were determined. Some characteristic parameters for describing the arch (*e.g.* arch length, arch aspect ratio and the angle between the beads) were measured for all the recorded images at different silo widths. For all these parameters, we did not notice any significant change related to the adjustment in the silo width.

After that, we recorded discharge videos without any interruption by using a fast camera with high enough speed. All the beads were detected, and tracking in these videos was achieved by using a MATLAB code. From the evaluation of the videos we were able to calculate the particle flow rate by counting all the beads which passed the orifice line in a certain time. The data show an increase of around 20 % in the value of the flow rate when the silo becomes narrower. By checking the instantaneous flow rate in small time windows of 200 ms, a long tail appeared toward the small values of the flow rate for silo widths at which the small avalanches were recorded. This tail disappeared for the narrowest and wide silos, which indicated the vanishing of intermittency during the discharge.

Finally, in this part of the study we also investigated the effect of the silo width on the packing fraction and the velocity field of the beads inside the silo, by applying the averaging coarse-graining technique. The experimental work was executed for six different silo widths, starting with a silo with a diameter of 6 beads and ultimately reaching 180 beads in diameter. A significant change in the packing fraction associated with the adjustment to the width appears clearly and explains the stability in the case of the wide silo. It was also evident that the packing fraction on both sides of the orifice decreased with decreasing silo width toward the narrowest silo. Also, when the side walls approached the orifice this led to an increase in the values of the vertical velocity at the area above the orifice.

In chapter 4, we studied the effect of softness and friction of the particles on the clogging probability and the flow rate inside a quasi-2D silo. To that end we loaded our quasi-2D silo with soft and frictionless monodisperse hydrogel spheres. These hydrogels were bought as hard spheres and put in distilled water for more than 10 hours to swell and reach their maximum size. The measured Young's modulus for the hydrogels was between 30 kPA and 50 kPa. Their center is slightly harder than the outer layer. These characteristic features of the hydrogel spheres gave new quantitative and qualitative results during the discharge from the silo which had not been described before when using hard grains.

When the orifice width was larger than 2.1 sphere diameter, the silo let almost all the spheres through without any clogging and only a few spheres finally remained at the silo bottom. If the orifice size was below 2.1 sphere diameter, non-permanent clogging events were present for seconds, before being resolved by themselves. At low silo fill heights they were followed by a permanent clogging state. The final arch which blocked the outlet depended mainly on the remaining amount of the hydrogels inside the silo, which indicated a certain critical value for the pressure at the bottom. The remaining filling height corresponding to the final clogging state was found to increase with decreasing orifice size (we recorded clogging until $W/D \approx 1.5$).

By using a pressure sensor placed at the bottom of the silo, a linear increase in the pressure with the filling height was recorded by using the hydrogels. This is in contrast to the result when filling the silo with hard grains, where the pressure saturates at a certain filling height and the remaining weight of the grains above is directed toward the side walls by force chains. The very low friction of the hydrogel spheres may play an important role in that, it may render the redirection of the weight of the material to the lateral silo walls quite ineffective.

The velocity fields of the hydrogels during discharge were obtained by evaluating the recorded videos, which were taken at different orifice sizes by a fast camera placed in front of the silo. From the velocity maps, we could not see any stagnant zones on the sides of the orifice as in the case of the hard grains, and the funnel flow shape above the orifice disappeared at height $\approx 2.5\ W$ from the silo bottom. Above that height, the hydrogels move with a constant velocity. The reason for that could be related to the monodispersity of the hydrogels which shows a hexagonal grid in the upper part during the outflow and dislocated at the area above the orifice. This could reinforce plug flow, instead of a parabolic flow profile. This behavior might change if we used polydisperse hydrogels. The friction or the softness may play an only secondary role.

The discharge of the hydrogels shows a continuous flow when $W/D > 2.1$. Beverloo's equation still fits the outflow data of the soft hydrogel spheres in this region, and for the other region at which $W/D < 2.1$ it was meaningless because of the interruption and variation in the flow during the discharge. Also, the soft frictionless grains show a higher flow rate when compared to the hard airsoft balls of similar geometrical parameters.

In conclusion, in this thesis I have studied new phenomena not previously presented, by means of the construction of three different silos. In these silos I have investigated the effect of the aspect ratio, lateral wall positions and softness & friction on the clogging probability and the discharge flow at small orifice sizes.

Bibliography

[1] H. M. Jaeger, S.R. Nagel, and R. P. Beringer. Granular solids, liquids, and gases. *Rev. Mod. Phys.*, 68:1259, 1996.

[2] C. S. Campbell. Granular material flows - an overview. *J. Powder Techn.*, 162:208, 2006.

[3] M. O. Carpinlioglu. A critical review on modeling and analysis of granular matter flows. *Int. J. Chemistry and Chem. Eng. Syst.*, 1:21, 2016.

[4] Ko van der Weele. Granular gas dynamics: how maxwells demon rules in a non-equilibrium system. *Contemporary Physics*, 49:157–178, 2008.

[5] Iker Zuriguel. Clogging of granular materials in bottlenecks. *Papers in Physics*, 6:060014, 2014.

[6] A. Medina J. A. Córdova, E. Luna, and C. Treviño. Velocity field measurements in granular gravity flow in a near 2d silo. *Physics Letters A*, 250:111–116, 1998.

[7] M. L. Hunt, R. C. Weathers, A. T. Lee, C. E. Brennen, and C. R. Wassgren. Effects of horizontal vibration on hopper flows of granular materials. *Phys. Fluids*, 11:1, 1999.

[8] P. W. Cleary. The effect of particle shape on hopper discharge. *Second International Conference on CFD in the Minerals and Process Industries*, pages 71–76, 1999.

[9] S. S. Manna and H. J. Herrmann. Intermittent granular flow and clogging with internal avalanches. *Eur. Phys. J.E*, 1:341–344, 2000.

[10] Kiwing To, Pik-Yin Lai, , and H. K. Pak. Jamming of granular flow in a two-dimensional hopper. *Phys. Rev. Lett.*, 86:71, 2001.

[11] K. To and Pi. Y. Lai. Jamming pattern in a two-dimensional hopper. *Phy. Rrv. E*, 66:011308, 2002.

[12] A. Samadani, L. Mahadevan, and A. Kudrplli. Shocks in sand flowing in a silo. *J. Fluid Mech.*, 452:293–301, 2002.

[13] C. R. Wassgren, M. L. Hunt, P. J. Freese, J. Palamara, and C. E. Brennen. Effects of vertical vibration on hopper flows of granular material. *Phys. Fluids*, 14:10, 2002.

[14] Kiwing To. Jamming transition in two-dimensional hoppers and silos. *Phys. Rev. E*, 71:060301, 2005.

[15] J. Choi, A. Kudrolli, and M. Z. Bazant. Velocity profile of granular flows inside silos and hoppers. *J. Phys.: Condens. Matter*, 17:S2533–S2548, 2005.

[16] A. Janda, I. Zuriguel, A. Garcimartín, L. A. Pugnaloni, and D. Maza. Jamming and critical outlet size in the discharge of a two-dimensional silo. *EPL*, 84:44002, 2008.

[17] A. Longjas, C. Monterola, and C. Saloma. Force analysis of jamming with disks of different sizes in a two-dimensional hopper. *J. Stat. Mech.*, page P05006, 2009.

[18] Angel Garcimartín, Iker Zuriguel, Luis A. Pugnaloni, and Alvaro Janda1. Shape of jamming arches in two-dimensional deposits of granular materials. *Phys. Rev. E*, 82:031306, 2010.

[19] Iker Zuriguel, Alvaro Janda, Angel Garcimartín, Celia Lozano, Roberto Arévalo, and Diego Maza. Silo clogging reduction by the presence of an obstacle. *Phys. Rev. Lett.*, 107:278001, 2011.

[20] I. Sielamowicz, M. Czech, and T. A. Kowalewski. Empirical description of granular flow inside a model silo with vertical walls. *Biosystems Engineering*, 108:334–344, 2011.

[21] Angel Garcimartín, Iker Zuriguel, Alvaro Janda, , and Diego Maza. Fluctuations of grains inside a discharging two-dimensional silo. *Phys. Rev. E*, 84:031309, 2011.

[22] M. A. Aguirre, J. G. Grande, A. Calvo, L. A. Pugnaloni, and J. C. Geminard. Granular flow through an aperture: Pressure and flow rate are independent. *Phy. Rev. E*, 83:061305, 2011.

[23] J. Tang and R.P. Behringer. How granular materials jam in a hopper. *Chaos*, 21:041107, 2011.

[24] K. Grudzien, M. Niedostatkiewicz, J. Adrien, J. Tejchman, and E. Maire. Quantitative estimation of volume changes of granular materials during silo flow using x-ray tomography. *Chemical Engineering and Processing: Process Intensification*, 50:59 – 67, 2011.

[25] T. Kanzaki, M. Acevedo, I. Zuriguel, I. Pagonabarraga, D. Maza, and R. C. Hidalgo. Stress distribution of faceted particles in a silo after its partial discharge. *Eur. Phys. J. E*, 34:133, 2011.

[26] Francisco Vivanco, Sergio Rica, and Francisco Melo. Dynamical arching in a two dimensional granular flow. *Granular Matter*, 14:563–576, 2012.

[27] C. Lozano, A. Janda, A. Garcimartín, D. Maza, and I. Zuriguel. Flow and clogging in a silo with an obstacle above the orifice. *Phys. Rev. E*, 86:031306, 2012.

[28] Alvaro Janda, Iker Zuriguel, and Diego Maza. Flow rate of particles through apertures obtained from self-similar density and velocity profiles. *Phys. Rev. E*, 108:248001, 2012.

[29] A. Guariguata, M. A. Pascall, M. W. Gilmer, A. K. Sum, E. D. Sloan, C. A. Koh, , and D. T. Wu. Jamming of particles in a two-dimensional fluid-driven flow. *Phys. Rev. E*, 86:061311, 2012.

[30] C. M. Carlevaro and L. A. Pugnaloni. Arches and contact forces in a granular pile. *Eur. Phys. J. E*, 35:44, 2012.

[31] L. Staron, P. Y. Lagree, and S. Popinet. The granular silo as a continuum plastic flow:the hour-glass vs the clepsydra. *Physics of Fluids*, 24:103301, 2012.

[32] R.O. Unac, A.M. Vidales, and L.A. Pugnaloni. The effect of the packing fraction on the jamming of granular flow through small apertures. *Journal of Statistical Mechanics: Theory and Experiment*, 04:P04008, 2012.

[33] G. Mollon and J. Zhao. Characterization of fluctuations in granular hopper flow. *Granular Matter*, 15:827–840, 2013.

[34] R. C. Hidalgo, C. Lozano, I. Zuriguel, and A. Garcimartín. Force analysis of clogging arches in a silo. *Granular Matter*, 15:841–848, 2013.

[35] S.-S. Hsiau, J. Smid, Y.P. Chyou, T.-C. Liu, T.-C. Huang, and C.-J. Hsu. Impact of flow-corrective insert on flow patterns in two-dimensional moving bed. *Chemical Engineering and Processing*, 73:7–15, 2013.

[36] S. Tewari, M. Dichter, and B. Chakraborty. Signatures of incipient jamming in collisional hopper flows. *Soft Matter*, 9:5016, 2013.

[37] Takumi Masuda, Katsuhiro Nishinari, and Andreas Schadschneider. Critical bottleneck size for jamless particle flows in two dimensions. *Phys. Rev. Lett.*, 112:138701, 2014.

[38] S. Albaraki and S. J. Antony. How does internal angle of hoppers affect granular flow? experimental studies using digital particle image velocimetry. *Powder Technology*, 268:253–260, 2014.

[39] L. Kondic. Simulations of two dimensional hopper flow. *Granular Matter*, 16:235–242, 2014.

[40] M. A. Aguirre, R. De Schant, and J. -C. Géminard. Granular flow through an aperture: Influence of the packing fraction. *Phys. Rev. E*, 90:012203, 2014.

[41] I. Sielamowicz, A. Czech, and T. A. Kowalewski. Comparative analysis of empirical descriptions of eccentric flow in silo model by the linear and nonlinear regressions. *Powder Technology*, 270:393–410, 2015.

[42] C. Lozano, I. Zuriguel, and A. Garcimartń. Stability of clogging arches in a silo submitted to vertical vibrations. *Phys. Rev. E*, 91:062203, 2015.

[43] R. Arévalo and I. Zuriguel. Clogging of granular materials in silos: effect of gravity and outlet size. *Soft Matter*, 12:123, 2016.

[44] J. Tang and R. P. Behringer. Orientation, flow, and clogging in a two-dimensional hopper: Ellipses vs. disks. *Europhysics Letters*, 114:34002, 2016.

[45] D. Gella, D. MAza, and I. Zuriguel. Role of particle size in the kinematic properties of silo flow. *Phy. Rev. E*, 95:052904, 2017.

[46] D. Gella, D. Maza, I. Zuriguel, A. Ashour, R. Arévalo, and R. Stannarius. Linking bottleneck clogging with flow kinematics in granular materials: the role of silo width. *Phys. Rev. Fluids*, 2:084304, 2017.

[47] K. Endo, K. A. Reddy, and H. Katsuragi. Obstacle-shape effect in a two-dimensional granular silo flow field. arXiv:1706.04791v1.

[48] F. C. Franklin and L. N. Johanson. Flow of granular material through a circular orifice. *Chem. Eng. Sci.*, 4:119–129, 1955.

[49] W. A. Beverloo, H. A. Leniger, and J. J. Van de Velde. The flow of granular solids through orifices. *Chem. Eng. Sci.*, 15:260, 1961.

[50] R. M. Neddermann, U.Tuzun, S. B. Savage, and G. T. Houlsby. The flow of granular materials discharge rates from hoppers. *Chem. Eng. Sci.*, 37:1597–1609, 1982.

[51] G. W. Baxter, R. P. Behringer, T. Fagert, and G. A. Johnson. Pattern formation in flowing sand. *Phys. Rev. Lett.*, 62:24, 1989.

[52] C. S. Chang, H. H. Converse, and J. L. Steele. Flow rates of grain through various shapes of vertical and horizontal orifices. *American Society of Agricultural Engineers*, 34:1789–1796, 1991.

[53] A. Drescher, A. J. Waters, and C. A. Rhoades. Arching in hoppers: Ii. arching theories and critical outlet size. *Powder Technology*, 84:177–183, 1995.

[54] E. R. Nowak, J. B. Knight, E. Ben-Naim, H. M. Jaeger, and S. R. Nagel. Density fluctuations in vibrated granular materials. *Phys. Rev. E*, 57:1971, 1998.

[55] D. Hirshfeld and D. C. Rapaport. Granular flow from a silo: Discrete-particle simulations in three dimensions. *Eur. Phys. J. E*, 4:193 – 199, 2001.

[56] Z. Zhong, J. Y. Ooi, and J. M. Rotter. the sensitivity of silo flow and wall stresses to filling methd. *Engineering Structures*, 23:756–767, 2001.

[57] I. Zuriguel, L. A. Pugnaloni, A. Garcimartín, and D. Maza. Jamming during the discharge of grains from a silo described as a percolating transition. *Phys. Rev. E*, 68:030301, 2003.

[58] Iker Zuriguel, Angel Garcimartín, Diego Maza, Luis A. Pugnaloni, and J. M. Pastor. Jamming during the discharge of granular matter from a silo. *Phys. Rev. E*, 71:051303, 2005.

[59] H. P. Zhu and A. B. Yu. Steady-state granular flow in a 3d cylindrical hopper with flat bottom: macroscopic analysis. *Granular Matter*, 7:97–107, 2005.

[60] K. Chen, M. B. Stone, R. Barry, M. Lohr, W. McConville, K. Klein, B. L. Sheu, A. J. Morss, T. Scheidemantel, and P. Schiffer. Flux through a hole from a shaken granular medium. *Phys. Rev. E*, 74:011306, 2006.

[61] L. Pournin, M. Ramaioli, P. Folly, and Th. M. Liebling. About the influence of friction and polydispersity on the jamming behavior of bead assemblies. *Eur. Phys. J. E*, 23:229, 2007.

[62] M. Tsukahara, S. Mitrovic, V. Gajdosik, G. Margaritondo, L. Pournin, M. Ramaioli, D. Sage, Y. Hwu, M. Unser, and Th. M. Liebling. Coupled tomography and distinct-element-method approach to exploring the granular media microstructure in a jamming hourglass. *Phy. Rev. E*, 77:061306, 2008.

[63] A. Janda, R. Harich, I. Zuriguel, D. Maza, P. Cixous, and A. Garcimartin. Flow-rate fluctuations in the outpouring of grains from a two-dimensional silo. *Phys. Rev. E*, 79:031302, 2009.

[64] Cristian Mankoc, Angel Garcimartín, Iker Zuriguel, and Diego Maza. Role of vibrations in the jamming and unjamming of grains discharging from a silo. *Phys. Rev. E*, 80:011309, 2009.

[65] A. Janda, D. Maza, A. Garcimartín, E. Kolb, J. Lanuza, and E. Clément. Unjamming a granular hopper by vibration. *Europhys. Lett.*, 87:24002, 2009.

[66] Hannah G. Sheldon and Douglas J. Durian. Granular discharge and clogging for tilted hoppers. *Granular Matter*, 12:579–585, 2010.

[67] Baosheng Jin, He Tao, and Wenqi Zhong. Flow behaviors of non-spherical granules in rectangular hopper. *Chinese Journal of Chemical Engineering*, 18:931 – 939, 2010.

[68] H. Tao, B. Jin, W. Zhong, X. Wang, B. Ren, Y. Zhang, and R. Xiao. Discrete element method modeling of non-spherical granular flow in rectangular hopper. *Chemical Engineering and Processing: Process Intensification*, 49:151 – 158, 2010.

[69] R. Hidalgo, I. Zuriguel, D. Maza, and I. Pagonabarraga. Granular packings of elongated faceted particles deposited under gravity. *J. Stat. Mech*, page P06025, 2010.

[70] M. A. Aguirre, J. G. Grande, A. Calvo, L. A. Pugnaloni, and J.-C. Géminard. Pressure independence of granular flow through an aperture. *Phy. Rev. Lett.*, 104:238002, 2010.

[71] J. E. Hilton and P. W. Cleary. Granular flow during hopper discharge. *Phys. Rev. E*, 84:011307, 2011.

[72] Summer Saraf and Scott V. Franklin. Power-law flow statistics in anisometric (wedge) hoppers. *Phys. Rev. E*, 83:030301, 2011.

[73] C. Perge, M. A. Aguirre, P. A. Gago, L. A. Pugnaloni, D. Le Tourneau, and J. C. Geminard. Evolution of pressure profiles during the discharge of a silo. *Phys. Rev. E*, 85:021303, 2012.

[74] István Oldal, István Keppler, Bela Csizmadia, and Laszlo Fenyvesi. Outflow properties of silos: The effect of arching. *Adv. Powder Tech.*, 23:290–297, 2012.

[75] C. C. Thomas and D. J. Durian. Geometry dependence of the clogging transition in tilted hoppers. *Phys. Rev. E*, 87:052201, 2013.

[76] M. Benyamine and M. Djermane. Discharge flow of a bidisperse granular media from a silo. *Phys. Rev. E*, 90:032201, 2014.

[77] S. D. Liu, Z. Y. Zhou, R. P. Zou, D. Pinson, and A.B. Yu. Flow characteristics and discharge rate of ellipsoidal particles in a flat bottom hopper. *Powder Techn.*, 253:70–79, 2014.

[78] T. J. Wilson, C. R. Pfeifer, N. Meysingier, and D. J. Durian. Granular discharge rate for submerged hoppers. *Papers in Physics*, 6:060009, 2014.

[79] Y. Wang, Y. Lu, and J. Y. Ooi. A numerical study of wall pressure and granular flow in a flat-bottomed silo. *Powder Technology*, 282:43 – 54, 2015.

[80] A. Janda, I. Zuriguel, A. Garcimartín, and D. Maza. Clogging of granular materials in narrow vertical pipes discharged at constant velocity. *Granular Matte*, 17:545–551, 2015.

[81] C. C. Thomas and D. J. Durian. Fraction of clogging configurations sampled by granular hopper flow. *Phys. Rev. Lett.*, 114:178001, 2015.

[82] G. Gutiérrez, C. Colonnello, P. Boltenhagen, J. R. Darias, R. Peralta-Fabi, F. Brau, and E. Clément. Silo collapse under granular discharge. *Phys. Rev. Lett.*, 114:018001, 2015.

[83] P. Mort et al. Dense granular flow -a collaborative study. *Powder Techn.*, 284:571, 2015.

[84] S. M. Rubio-Largo, A. Janda, D. Maza, I. Zuriguel, and R. C. Hidalgo. Disentangling the free-fall arch paradox in silo discharge. *Phys. Rev. Lett.*, 114:238002, Jun 2015.

[85] S. M. Rubio-Largo, D. Maza, and R. C. Hidalgo. Large-scale numerical simulations of polydisperse particle flow in a silo. *Comp. Part. Mech.*

[86] T. Börzsönyi, E. Somfai, B. Szabó, S. Wegner, P. Mier, G. Rose, and R. Stannarius. Packing, alignment and flow of shape-anisotropic grains in a 3d silo experiment. *New J. Phys.*, 18:093017, 2016.

[87] A. Ashour, S. Wegner, T. Trittel, T. Börzsönyi, and R. Stannarius. Outflow and clogging of shape-anisotropic grains in hoppers with small apertures. *Soft Matte*, 13:402, 2017.

[88] Y. Bertho, C. Becco, and N. Vandewalle. Dense bubble flow in a silo: An unusual flow of a dispersed medium. *Phy. Rev. E*, 73:056309, 2006.

[89] K. W. Desmond, P. J. Young, D. Chen, and E. R. Weeks. Experimental study of forces between quasi-twodimensional emulsion droplets near jamming. *Soft Matter*, 9:3424, 2013.

[90] X. Hong, K. W. Desmond, D. Chen, and E. R. Weeks. Avalanches of rearrangements in quasi-2d emulsion hopper flow. arXiv:1503.07569v1.

[91] X. Hong, M. Kohne, and E. R. Weeks. Clogging of soft particles in 2d hoppers. arXiv:1512.02500v2.

[92] J. Duran. *Sands, Powders and Grains: An Introduction to the Physics of Granular Materials.* Springer-Verlag, Berlin, 2000.

[93] V. Trappe, V. Prasad, L. Cipelletti, P. Segre, and D. Weitz. Jamming phase diagram for attractive particles. *Nature*, 411:772–775, 2001.

[94] E. Dressaire and A. Sauret. Clogging of microfluidic systems. *Soft Matte*, 13:37, 2017.

[95] M. D. Haw. Jamming, two-fluid behavior, and self-filtration in concentrated particulate suspensions. *Phys. Rev. Lett.*, 92:185506, 2004.

[96] D. Genovese and J. Sprakel. Crystallization and intermittent dynamics in constricted microfluidic flows of dense suspensions. *Soft Matter*, 7:3889, 2011.

[97] M. Delarue, J. Hartung, C. Schreck, P. Gniewek, L. Hu, S. Herminghaus, and O. Hallatschek. Self-driven jamming in growing microbial populations. *Nature Physics*, 12:762, 2016.

[98] A. Garcimartín, J. M. Pastor, L. M. Ferrer, J. J. Ramos, C. Martín-Gómez, and I. Zuriguel. Flow and clogging of a sheep herd passing through a bottleneck. *Phys. Rev. E*, 91:022808, 2015.

[99] D. Helbing, I. Farkas, and T. Vicsek. Simulating dynamical features of escape panic. *Nature*, 407:487, 2000.

[100] A. Garcimartín, J. M. Pastor, C. Martín-Gómez, D. R. Parisi, and I. Zuriguel. Pedestrian collective motion in competitive room evacuation. *Scientific Reports*, 7:10792, 2017. DOI:10.1038/s41598-017-11197-x.

[101] B. S. Kerner and H. Rehborn. Experimental properties of phase transitions in traffic flows. *Phys. Rev. Lett.*, 79:4030–4033, 1997.

[102] I. Zuriguel, D. R. Parisi, R. C. Hidalgo, C. Lozano, A. Janda, P. A. Gago, J. P. Peralta, L. M. Ferrer, L. A. Pugnaloni, E. Clément, D. Maza, I. Pagonabarraga, and A. Garcimartín. Clogging transition of many-particle systems flowing through bottlenecks. *Scientific Reports*, 4:7324, 2014.

[103] L. A. Pugnaloni and G.C. Barker. Structure and distribution of arches in shaken hard sphere deposits. *Physica A*, 337:428–442, 2004.

[104] A. Garcimartín, C. Lozano, G. Lumay, and I. Zuriguel. Avoiding clogs: the shape of arches and their stability against vibrations. *Powders and grains Conference*, page 686, 2013.

[105] C. Mankoc, A. Janda, R. Arévalo, J. M. Pastor, I. Zuriguel, A. Garcimartín, and D. Maza. The flow rate of granular materials through an orifice. *Granular Matter*, 9:407–414, 2007.

[106] H. A. Janssen. *Z. Ver. Dtsch. Ing.*, 39:1045, 1895.

[107] M: Sperl. Experiments on corn pressure in silo cells translation and comment of janssens paper from 1895. *Granular Matter*, 8:59–65, 2006.

[108] R. Arévalo, D. Maza, and L. A. Pugnaloni. Identification of arches in two-dimensional granular packings. *Phys. Rev. E*, 74:021303, 2006.

[109] L. A. Pugnaloni, M. G. Valluzzi, and L. G. Valluzzii. Arching in tapped deposits of hard disks. *Phys. Rev. E*, 73:051302, 2006.

[110] C. Lozano, G. Lumay, I. Zuriguel, R. C. Hidalgo, and A.Garcimartín. Breaking arches with vibrations: The role of defects. *Phys. Rev. Lett.*, 109:068001, 2012.

[111] S. Dorbolo, L. Maquet, M. Brandenbourger, F. Ludewig, G. Lumay, H. Caps, N. Vandewalle, S. Rondia, M. Mélard, J. van Loon, A. Dowson, and S. Vincent-Bonnieu. Influence of the gravity on the discharge of a silo. *Granular Matter*, 15:263–273, 2013.

[112] R. Arévalo, I. Zuriguel, D. Maza, and A. Garcimartín. Role of driving force on the clogging of inert particles in a bottleneck. *Phys. Rev. E*, 89:042205, 2014.

[113] C. E. Davies and J. Foye. Flow of granular material through vertical slots. *Chem. Eng. Res. and Des .*, 69:369, 1991.

[114] P. W. Cleary and M. L. Sawley. Dem modelling of industrial granular flows: 3d case studies and the effect of particle shape on hopper discharge. *Appl. Math. Modelling*, 26:89–111, 2002.

[115] P. A. Langston, M. A. Al-Awamleh, F. Y. Fraige, and B. N. Asmar. Distinct element modelling of non-spherical frictionless particle flow. *Chem. Eng. Sci.*, 59:425–435, 2004.

[116] M. Trepanier and S. V. Franklin. Column collapse of granular rods. *Phys. Rev. E*, 82:011308, 2010.

[117] G. D. Scott. Packing of spheres: Packing of equal spheres. *Nature*, 188:908, 1960.

[118] A. P. Philipse. The random contact equation and its implications for (colloidal) rods in packings, suspensions, and anisotropic powders. *Langmuir*, 12:1127, 1996.

[119] B. J. Buchalter and R. M. Bradley. Orientational order in amorphous packings of ellipsoids. *Europhys. Lett.*, 26:159–164, 1994.

[120] I. Goldhirsch. Stress, stress asymmetry and couple stress: from discrete particles to continuous fields. *Granular Matter*, 12:239–252, 2010.

[121] T. Weinhart, C. Labra, S. Luding, and J. Y. Ooi. Influence of coarse-graining parameters on the analysis of dem simulations of silo flow. *Powder Technology*, 293:138–148, 2016.

[122] R. Artoni and P. Richard. Average balance equations, scale dependence, and energy cascade for granular materials. *Phys. Rev. E*, 91:032202, 2015.

[123] W. Song, A. C. Lima, and J. F. Mano. Bioinspired methodology to fabricate hydrogel spheres for multi-applications using superhydrophobic substrates. *Soft Matter*, 6:5868–5871, 2010.

[124] T. Bertrand, R. P. Behringer, B. Chakraborty, C. S. OHern, and M. D. Shattuck. Protocol dependence of the jamming transition. *Phy. Rev. E*, 93:012901, 2016.

[125] N. Brodu, J. A. Dijksman, and R. P. Behringer. Spanning the scales of granular materials through microscopic force imaging. *Nat Commun*, 6:6361, 2015.

Scientific Achievements

Publications Related to this Thesis

- **A. Ashour**, S. Wegner, T. Trittel, T. Börzsönyi and R. Stannarius. *Outflow and clogging of shape-anisotropic grains in hoppers with small apertures. Soft Matter.* 13:402-414 (2017).
- D. Gella, D. Maza, I. Zuriguel, **A. Ashour**, R. Arévalo and R. Stannarius. *Linking bottleneck clogging with flow kinematics in granular materials: the role of silo width. Phys. Rev. Fluids.* 2:084304 (2017).
- **A. Ashour**, T. Trittel, T. Börzsönyi and R. Stannarius. *Silo outflow of soft frictionless spheres. Phys. Rev. Fluids.* 2:123302 (2017).

Additional Publications

- F. El-Diasty, M. A. Soliman, Abdel Fatah T. Elgendy and **A. Ashour**. *Birefringence dispersion in uniaxial material irradiated by gamma rays: Cellulose triacetate films. J. Opt. A: Pure Appl. Opt.* 9:247 (2007).
- H. El-Ghandoor, M. Saudy and **A. Ashour**. *Analysis of Surface Roughness Using Laser Optical Imaging Techniques. J. Mater. Sci. Eng. B.* 2:7 (2012).
- T. Börzsönyi, E. Somfai, B. Szabó, S. Wegner, **A. Ashour**, and R. Stannarius. *Elongated grains in a hopper. EPJ Web Conf.* 140:06017 (2017).
- B. Szabó, Z. Kovács, S. Wegner, **A. Ashour**, D. Fischer, R. Stannarius and T. Börzsönyi. *Flow and clogging of anisometric particles in a quasi-2D hopper.**Submitted**, Phys. Rev. E.* (2017).

Other Scientific Achievements

- Holder of Future University Scholarship (2014), awarded for Ph.D. studies.

Acknowledgments

First of all I would like to thank Future University in Egypt which gave me the opportunity to carry out my Ph.D. work in Germany under the excellent supervision of Prof. Dr. Ralf Stannarius, whose invaluable advice and encouragement have enabled me to conduct my research successfully and complete my thesis.

This work could not have been completed without the experience gained during my five weeks in Pamplona with the prestigious group in the Universidad de Navarra - my warm thanks to Iker Zuriguel, Diego Gella, Diego Maza and Angel Garcimartín.

I would like also to thank our partners in the Institute for Solid State Physics and Optics, Budapest, Tamás Börzsönyi and Balázs Szabó for their assistance during the study of the quasi-2D hopper in Budapest.

My thanks also to everyone in the Department of Nonlinear Phenomena in Magdeburg for a very stimulating and productive time. In particular, I would like to mention Tilo Finger, who shared an office with me during my Ph.D. work. Thanks Tilo for your help and advice, I know you suffered a lot with my bad German! I am also most grateful to Torsten Trittel for his help and advice in solving the technical problems.

On a personal note, I owe an enormous debt to my parents, wife and family without whose love, patience, encouragement and support this project would not have come into being.

Finally, I cordially thank Prof. Dr. Ingo Rehberg, the external reviewer for devoting his valuable time to reading this dissertation.

Declaration

I hereby declare that I prepared the submitted thesis

Outflow and clogging of rigid and soft particles in silos with small apertures

without inadmissible assistance and without the use of any aids other than those indicated. Facts or ideas taken from other sources, either directly or indirectly have been marked as such.
This work has so far not been submitted either in Germany or abroad in same or similar form as a dissertation and has also not yet been published as a whole.

Ahmed Ashour Magdeburg, 22nd November 2017